

Simulating intermediate black hole mass measurements for a sample of galaxies with nuclear star clusters using ELT/HARMONI high spatial resolution integral-field stellar kinematics

DIEU D. NGUYEN ,¹ MICHELE CAPPELLARI ,² HAI N. NGO ,³ TINH Q. T. LE ,^{4,5,6} TUAN N. LE ,^{7,5} KHUE N. H. HO ,⁴ AN K. NGUYEN ,⁴ PHONG T. ON ,⁴ HUY G. TONG ,³ NIRANJAN THATTE ,² AND MIGUEL PEREIRA-SANTAELLA ,⁸

¹Department of Astronomy, University of Michigan, 1085 S University, Ann Arbor, MI 48109, USA

²Sub-Department of Astrophysics, Department of Physics, University of Oxford, Denys Wilkinson Building, Keble Road, Oxford, OX1 3RH, UK

³Faculty of Physics – Engineering Physics, University of Science, Vietnam National University in Ho Chi Minh City, Vietnam

⁴Department of Physics, International University, Vietnam National University in Ho Chi Minh City, Vietnam

⁵International Centre for Interdisciplinary Science and Education, 07 Science Avenue, Ghenh Rang, 55121 Quy Nhon, Vietnam

⁶Vietnam National Space Center, Vietnam Academy of Science and Technology, 18 Hoang Quoc Viet, Cau Giay, Hanoi, Vietnam

⁷University of Technology, Vietnam National University in Ho Chi Minh City, Vietnam

⁸Instituto de Física Fundamental, CSIC, Calle Serrano 123, 28006 Madrid, Spain

(Received May 5 2025; Revised June 18 2025; Accepted June 19 2025)

ABSTRACT

Understanding the demographics of intermediate-mass black holes (IMBHs, $M_{\text{BH}} \approx 10^2 - 10^5 M_{\odot}$) in low-mass galaxies is key to constraining black hole seed formation models, but detecting them is challenging due to their small gravitational sphere of influence (SOI). The upcoming ELT/HARMONI instrument, with its high angular resolution, offers a promising solution. We present simulations assessing HARMONI’s ability to measure IMBH masses in nuclear star clusters (NSCs) of nearby dwarf galaxies. We selected a sample of 44 candidates within 10 Mpc. For two representative targets, NGC 300 and NGC 3115 dw01, we generated mock HARMONI integral-field data cubes using realistic inputs derived from *HST* imaging, stellar population models, and Jeans Anisotropic Models (JAM), assuming IMBH masses up to 1% of the NSC mass. We simulated observations across six NIR gratings at 10 mas resolution. Analyzing the mock data with standard kinematic extraction (pPXF) and JAM models in a Bayesian framework, we demonstrate that HARMONI can resolve the IMBH SOI and accurately recover masses down to $\approx 0.5\%$ of the NSC mass within feasible exposure times. These results highlight HARMONI’s potential to revolutionize IMBH studies.

Keywords: Astrophysical black holes (98) — Galaxy kinematics (602) — Galaxy dynamics (591) — Galaxy nuclei (609) — Galaxy spectroscopy (2171) — Astronomy data modeling (1859)

1. INTRODUCTION

Supermassive black holes (SMBHs, $M_{\text{BH}} \gtrsim 10^6 M_{\odot}$) residing in the centers of massive galaxies ($M_{\star} \gtrsim 10^{10} M_{\odot}$) exhibit well-established correlations with host galaxy properties, such as bulge stellar mass (M_{\star}) and velocity dispersion (σ_{\star}) (J. Kormendy & D. Richstone 1995; J. Magorrian et al. 1998; L. Ferrarese & D. Merritt 2000; K. Gebhardt et al. 2000; J. Kormendy & L. C. Ho 2013). These scaling relations suggest a fundamental co-evolution between SMBHs and their hosts (J. Silk & M. J. Rees 1998; T. Di Matteo et al. 2008; A. C. Fabian 2012; D. Krajnović et al. 2018), offering insights

into galaxy assembly and the growth of cosmic structures (K. Gultekin et al. 2009; N. J. McConnell et al. 2011; H. Netzer 2015; J. W. Nightingale et al. 2023).

However, a significant gap exists between the observed populations of stellar-mass black holes (s-BHs, $M_{\text{BH}} \lesssim 10^2 M_{\odot}$), the remnants of massive stars (M. J. Graham et al. 2020), and the dynamically confirmed SMBHs ($M_{\text{BH}} \gtrsim 10^5 M_{\odot}$) (R. Pechetti et al. 2022). The nature of objects within this intermediate-mass range (IMBHs, $M_{\text{BH}} \approx 10^{2-5} M_{\odot}$) remains unconstrained (D. D. Nguyen et al. 2017, 2018, 2019).

Understanding the demographics of IMBHs is crucial for deciphering the origins of SMBHs. Current theories propose that SMBHs grow from “seeds” formed in the early Universe, which could be either light seeds ($M_{\bullet} \approx 10^{2-3} M_{\odot}$) derived from the first stars (S. van Wassenhove et al. 2010;

Corresponding author: Dieu D. Nguyen
 dieun@umich.edu

M. Volonteri 2012; M. Volonteri et al. 2021) or heavy seeds ($M_\bullet \approx 10^{4-5} M_\odot$) formed via direct gas collapse (J. E. Greene 2012; S. Bonoli et al. 2014). The abundance and mass distribution of IMBHs in present-day low-mass galaxies provide a key observational test for these seeding scenarios (M. Mezcua 2017; J. E. Greene et al. 2020; K. Inayoshi et al. 2020).

Detecting and characterizing IMBHs is observationally challenging due to their relatively small gravitational influence compared to SMBHs, requiring high spatial resolution kinematics. This difficulty explains the current uncertainty surrounding their existence and properties, motivating the simulations presented in this work.

1.1. Previous IMBH Determinations and Observational Challenges

Dynamical mass measurements, which infer mass from the motion of tracers (stars or gas) under gravity, exist for roughly 120 black holes (BHs, see review by J. Kormendy & L. C. Ho 2013). However, only about 23 of these fall within the intermediate-mass black hole (IMBH) range ($M_{\text{BH}} \sim 10^{2-5} M_\odot$) (see review by J. E. Greene et al. 2020). These measurements utilize various kinematic tracers and techniques, including stellar dynamics (e.g., E. K. Verolme et al. 2002; K. Gebhardt et al. 2003; D. D. Nguyen 2017; D. D. Nguyen et al. 2025), ionized gas dynamics (e.g., A. J. Barth et al. 2001; J. L. Walsh et al. 2013), molecular gas dynamics (e.g., T. A. Davis et al. 2013; D. D. Nguyen 2019; D. D. Nguyen et al. 2020), atomic gas dynamics (e.g., D. D. Nguyen et al. 2021), and maser disk kinematics (e.g., M. Miyoshi et al. 1995; E. González-Alfonso et al. 2023).

While SMBHs are common in massive galaxies (J. Kormendy & L. C. Ho 2013; N. J. McConnell & C.-P. Ma 2013; R. P. Saglia et al. 2016), the existence and characteristics of IMBHs in lower-mass galaxies are less certain. Some studies report detections (D. D. Nguyen et al. 2019, 2022; R. Pechetti et al. 2022), while others provide only upper limits or suggest their absence (K. Gebhardt et al. 2001; D. Merritt et al. 2001; M. Valluri et al. 2005; D. D. Nguyen et al. 2014). Indirect evidence, such as the off-nuclear X-ray source HLX-1 (O. Straub et al. 2014), also points towards the existence of IMBHs. Promising locations for IMBH searches include nuclear star clusters (NSCs) in dwarf galaxies, globular clusters (GCs), and ultra-compact dwarf galaxies (UCDs) (K. Gebhardt et al. 2005; E. Noyola et al. 2010; A. C. Seth et al. 2014; N. Neumayer et al. 2020).

A major challenge in dynamically detecting IMBHs is resolving their gravitational sphere of influence (SOI), the region where the BH's gravity dominates. The SOI radius is approximately $R_{\text{SOI}} \equiv GM_{\text{BH}}/\sigma_\star^2$, where σ_\star is the stellar velocity dispersion outside the SOI. For a typical IMBH ($M_{\text{BH}} \approx 10^5 M_\odot$) in a dwarf galaxy ($\sigma_\star \approx 10 \text{ km s}^{-1}$) at

a distance of $D \approx 10 \text{ Mpc}$, the SOI radius is very small, $R_{\text{SOI}} \approx 0.09$ (T. de Zeeuw 2001).

This small angular scale is difficult to resolve with current telescopes. Even facilities equipped with adaptive optics (AO), such as VLT/ERIS or Keck/OSIRIS (achieving a point spread function (PSF) $\text{FWHM}_{\text{PSF}} \approx 0.05$), struggle to resolve the SOI of IMBHs beyond the Local Group. The *James Webb Space Telescope* (JWST), despite its excellent sensitivity, lacks the angular resolution needed for unambiguous kinematic detection of IMBHs in distant dwarf galaxies. As a result, the demographics of IMBHs remain poorly constrained.

Understanding the IMBH population is vital for several reasons. It helps distinguish between different BH seeding scenarios (e.g., light seeds from Population III stars versus heavy seeds from direct gas collapse), which predict varying IMBH occupation fractions in low-mass galaxies (E. Gallo et al. 2008; D. D. Nguyen et al. 2018, 2019). It is also crucial for understanding BH–galaxy co-evolution and for predicting gravitational wave event rates for future observatories (C. S. Kochanek 2016; M. Bailes et al. 2021). The limitations of current instruments highlight the need for next-generation facilities like the Extremely Large Telescope (ELT) with instruments such as the High Angular Resolution Monolithic Optical and Near-infrared Integral field spectrograph (HARMONI).

1.2. The role of ELT/HARMONI

Detecting IMBHs ($M_{\text{BH}} \sim 10^{2-5} M_\odot$) is challenging because their gravitational SOI is extremely small (subsection 1.1), requiring observations with very high angular resolution. The HARMONI (N. A. Thatte et al. 2016, 2020; N. A. Thatte et al. 2024) on the ELT is well-suited for this task. Equipped with AO, HARMONI will provide excellent sensitivity along with high spectral ($\lambda/\Delta\lambda \sim 3300 - 17,400$) and angular ($\text{FWHM}_{\text{PSF}} \approx 12 \text{ milli-arcseconds, mas}$) resolution.

With these capabilities, HARMONI can resolve the SOI and measure detailed stellar kinematics within NSCs – the likely hosts of IMBHs – in galaxies out to $\approx 10 \text{ Mpc}$ (this work). HARMONI will greatly expand the volume accessible for IMBH searches compared to current instruments and should provide the first robust constraints on IMBH demographics. This is crucial for distinguishing between BH seeding scenarios in the early Universe (J. E. Greene et al. 2020; K. Inayoshi et al. 2020) and understanding the co-evolution of BHs and galaxies at low masses. This work complements our previous study on HARMONI's capability for measuring SMBHs in more massive galaxies (D. D. Nguyen et al. 2023, hereafter N23).

We outline the selection criteria for our HARMONI IMBH survey in section 2 and present the sample properties in section 3. The dynamical and photometric models are described

in section 4 and section 5, respectively. section 6 details the mock HARMONI IFS simulations using the HARMONI SIMulator (HSIM⁹; S. Zieleniewski et al. 2015) and the kinematic extraction process. We discuss the recovery of IMBH masses and potential limitations in section 7, and summarize our findings in section 8.

Throughout this paper, we adopt a flat Λ CDM cosmology with $H_0 = 70 \text{ km s}^{-1} \text{ Mpc}^{-1}$, $\Omega_{\text{m},0} = 0.3$, and $\Omega_{\Lambda,0} = 0.7$. All magnitudes use the AB system (J. B. Oke 1974) and are corrected for foreground extinction (E. F. Schlafly & D. P. Finkbeiner 2011) using the J. A. Cardelli et al. (1989) law.

2. SAMPLE SELECTION

Our sample selection process aims to identify nearby, low-mass galaxies ($M_{\star} \lesssim 5 \times 10^{10} M_{\odot}$) likely hosting NSCs and potentially IMBHs, suitable for observation with ELT/HARMONI. Unlike the selection for the MMBH survey of ultra-massive galaxies (N23), which relied heavily on homogeneous 2MASS K_s -band photometry (M. F. Skrutskie et al. 2006; T. H. Jarrett et al. 2003) from the 2MASS Redshift Survey (2MRS; J. P. Huchra et al. 2012), we adopted a multi-stage approach due to the limitations of 2MASS for dwarf galaxies. The shallow depth and fixed aperture integration method of 2MASS can lead to unreliable total luminosities, effective radii (R_{e}), and Sérsic indices for compact, low-surface-brightness dwarf galaxies (J. Schombert & A. K. Smith 2012).

We began with the 2MRS catalog, estimating stellar masses from K_s -band luminosities assuming a constant mass-to-light ratio $M/L_K = 1 (M_{\odot}/L_{\odot})$ (D. D. Nguyen et al. 2018) and using distances from the Updated Nearby Galaxy Catalog (I. D. Karachentsev et al. 2013). We then estimated a virial velocity dispersion proxy using the well-calibrated virial relation $\sigma_{\text{vir}}^2 = GM_{\star}/(5R_{\text{e}})$ (M. Cappellari et al. 2006), where R_{e} was taken from 2MRS. We applied the following initial cuts:

- Virial dispersion proxy $\sigma_{\text{vir}} \lesssim 70 \text{ km s}^{-1}$. This threshold aims to select galaxies likely hosting IMBHs, based on extrapolating the $M_{\text{BH}}-\sigma_{\star}$ relation (J. E. Greene et al. 2020). Lower dispersions also imply larger angular sizes for the IMBH R_{SOI} , making them easier to resolve kinematically.
- Distance $D \lesssim 10 \text{ Mpc}$. This ensures the targets are close enough for HARMONI to potentially resolve the NSC structure and IMBH SOI.
- ELT Observability: Declination $|\delta + 24^{\circ}| < 45^{\circ}$ for good adaptive optics (AO) performance from the Amazones site.

⁹ v3.11; available from <https://github.com/HARMONI-ELT/HSIM>

- Galactic Plane Exclusion: Galactic latitude $|b| > 8^{\circ}$ to avoid regions of high dust extinction.

These criteria yielded an initial list of ≈ 500 galaxies.

We then visually inspected images for these ≈ 500 candidates, primarily using the Sloan Digital Sky Survey (SDSS; STScI 2020) or Digitized Sky Survey (DSS; STScI 2020) and higher-resolution *Hubble Space Telescope* (HST) archives when available, to identify galaxies clearly exhibiting a central nucleus (NSC).

Finally, to ensure completeness, we cross-referenced our visually selected nucleated galaxies with extensive literature compilations and studies focused on NSCs. This included photometric (T. Böker et al. 2002; C. J. Walcher et al. 2005, 2006; A. Seth et al. 2008; I. Y. Georgiev & T. Böker 2014; I. Y. Georgiev et al. 2016; R. Pechetti et al. 2020) and spectroscopic (L. C. Ho et al. 2009; N. Kacharov et al. 2018; D. D. Nguyen et al. 2018; K. Fahrion et al. 2022; V. F. Baldassare et al. 2022) surveys, as well as detailed case studies (G. F. Hägle et al. 2007; J. C. Shields et al. 2008; B. de Swardt et al. 2010; K. Fahrion et al. 2020; O. Müller et al. 2021; F. Pinna et al. 2021; D. D. Nguyen et al. 2022). Any galaxy meeting our initial criteria (D , σ_{vir} , observability) that was confirmed to host an NSC in the literature was added to our final sample, even if missed during the visual inspection phase.

This process resulted in a final sample of 44 galaxies, which we refer to as the “HARMONI IMBH survey”. This sample spans stellar masses $2 \times 10^7 \lesssim M_{\star} \lesssim 5 \times 10^{10} M_{\odot}$ (corresponding to K_s absolute magnitudes $-23.5 \lesssim M_K \lesssim -15.4$ mag) and includes a mix of morphological types (6 dE, 7 S0, 27 S, 4 Irr; see Table 2). Figure 1 displays images of the sample galaxies, and their properties are summarized in Table 6. The selection criteria are summarized in Table 1.

A crucial practical requirement for HARMONI observations using Laser Tomography Adaptive Optics (LTAO¹⁰) is the availability of a nearby tip-tilt star. This natural guide star (NGS) is needed for correcting atmospheric turbulence and should ideally have an H -band AB magnitude $m_H < 20.4$ mag, located within an annulus of $12''$ to $60''$ surrounding the science target (N. A. Thatte et al. 2020). We searched Gaia and SDSS archives for suitable NGS candidates for our sample galaxies. Potential NGS are marked in Figure 1 with their estimated H -band AB magnitudes. SDSS magnitudes were converted following Section 2.1 of N23, and Gaia Vegamags were converted using relations from the Gaia DR3 documentation (Section 5.5.1; G. Busso et al. 2022). Suitable NGS were found for the vast majority of targets, confirming the feasibility of LTAO observations.

¹⁰ LTAO mode on the ELT/HARMONI instrument needs at least one NGS to work simultaneously with six artificial off-axis Laser Guide Stars (LGS). This system allows the required NGS to be more than 10,000 times fainter than those needed for classical AO used on Gemini and VLT.

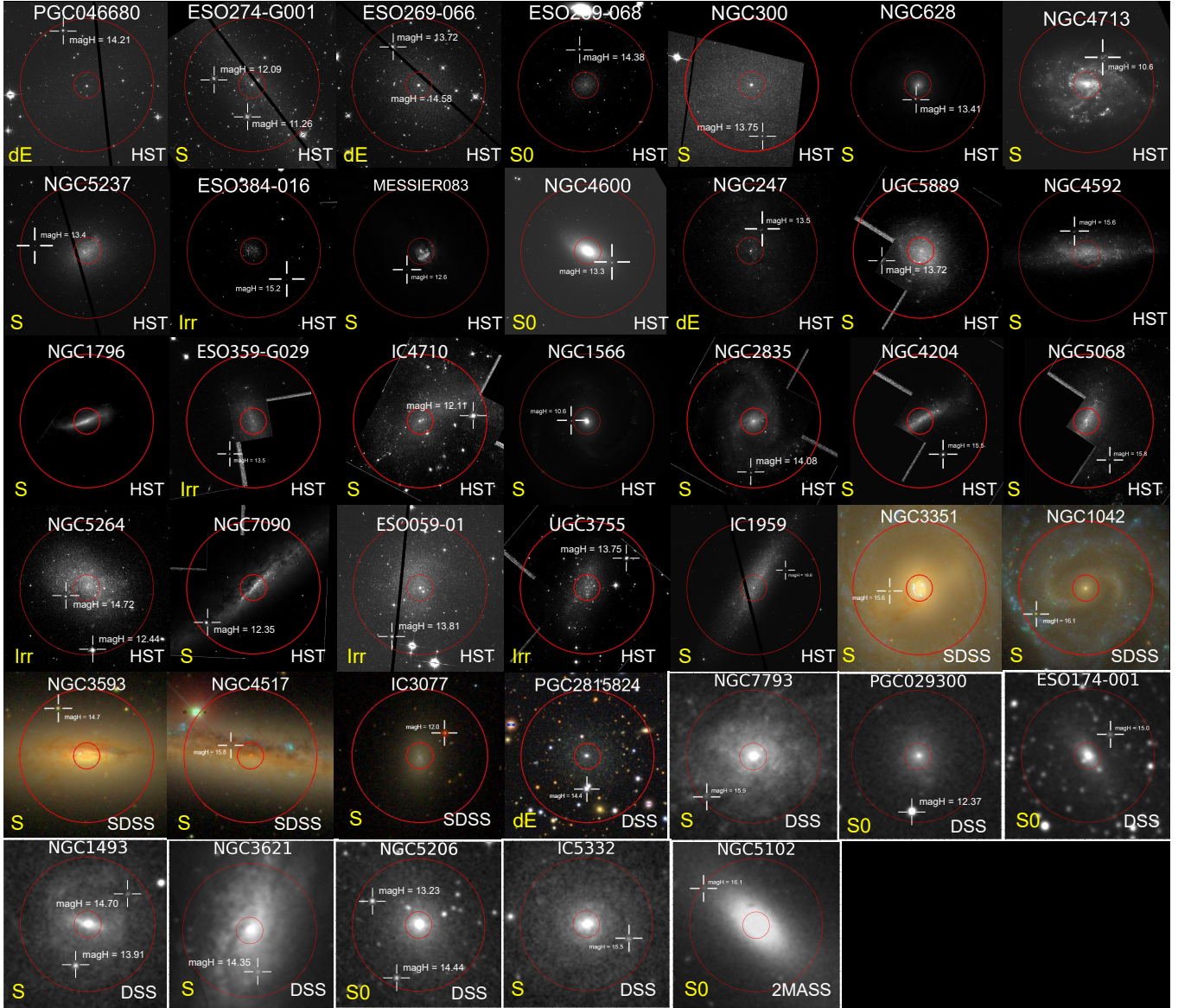


Figure 1. The 40 available observations out of the total number of 44 dwarf galaxies from our HARMONI IMBH sample, as captured in *HST*, *SDSS*, *DSS*, and *2MASS* images. To emphasize their NSCs at the core, the galaxy brightness has been adjusted. Each galaxy's name and galaxy types are also shown. Two red circles define the region around the galaxy's center, spanning from $12''$ to $60''$, where we search for a faint NGS essential for LTAO performance. The white crosses pinpoint the available NGS locations, specifying their apparent AB magnitudes measured in the H band. Here, dE = dwarf Elliptical, S0 = lenticular, S = Sprial, Irr = Irregular.

3. PROPERTIES OF THE HARMONI IMBH SAMPLE

3.1. HARMONI IMBH sample on the mass–size diagram

The left panel of Figure 2 shows the distribution of the HARMONI IMBH survey targets (red dots) in the absolute magnitude (M_K) versus distance plane. This sample occupies the low-mass end of the galaxy population. For comparison, we also plot galaxies from larger surveys like ATLAS^{3D} (M. Cappellari et al. 2011), MASSIVE (C.-P. Ma et al. 2014), and MMBH (N23), highlighting the unique parameter space probed by the HARMONI IMBH sample.

The right panel of Figure 2 presents the mass–size diagram (M_\star, R_e) for the HARMONI IMBH sample, using available stellar masses (M_\star) and effective radii (R_e). We overlay data from the 2MRS galaxy catalog (compiled by N23), excluding sources with potentially unreliable R_e measurements ($R_e < 5''$ or $R_e < 0.3$ kpc, see section 2). Data from the ATLAS^{3D}, MASSIVE, and MMBH surveys are also included. This comparison emphasizes that our sample targets galaxies with expected low stellar velocity dispersions (σ_\star) and, consequently, potentially low black hole masses (M_{BH}). Lines of constant σ_\star are shown for reference.

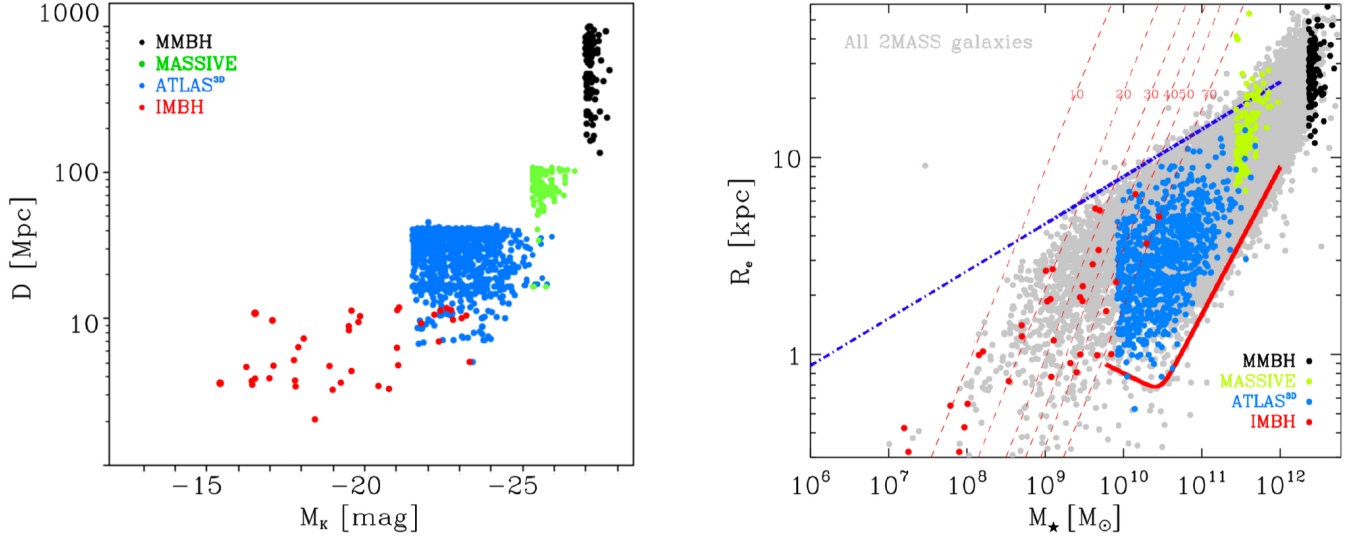


Figure 2. Left: Distance vs. absolute K_s -band magnitude of the HARMONI IMBH (red; this work), MASSIVE (green; C.-P. Ma et al. 2014), ATLAS^{3D} (blue; M. Cappellari et al. 2011), and MMBH (black; N23) surveys. There is an overlapping region between the HARMONI IMBH sample and the ATLAS^{3D} survey (i.e. $\approx 1.8 M_K$ mag or $10^{10} < M_\star < 5 \times 10^{10} M_\odot$). The plotted distance is the angular size distance $D = D_A$. **Right:** The mass-size diagram of the 2MRS sources (grey dots) shows a wide range of stellar mass: $10^7 < M_\star < 6 \times 10^{12} M_\odot$. The inclined-red-dashed lines indicate constant σ_\star of 10, 20, 30, 40, 50, 70 km s $^{-1}$. The ATLAS^{3D}, MASSIVE, MMBH, and HARMONI IMBH samples occupy different regions of the diagram. The thick-solid red curve defines the zone of exclusion described by eq. (4) of M. Cappellari et al. (2013a) in the previously explored stellar-mass range of $5 \times 10^9 \leq M_\star \leq 10^{12} M_\odot$. The thick dash-dotted blue line shows the relation $(R_e/\text{kpc}) = 8 \times [M_\star/(10^{10} M_\odot)]^{0.24}$, which provides a convenient approximation for the lower 99% contour for the distribution of early-type galaxies (M. Cappellari et al. 2013a).

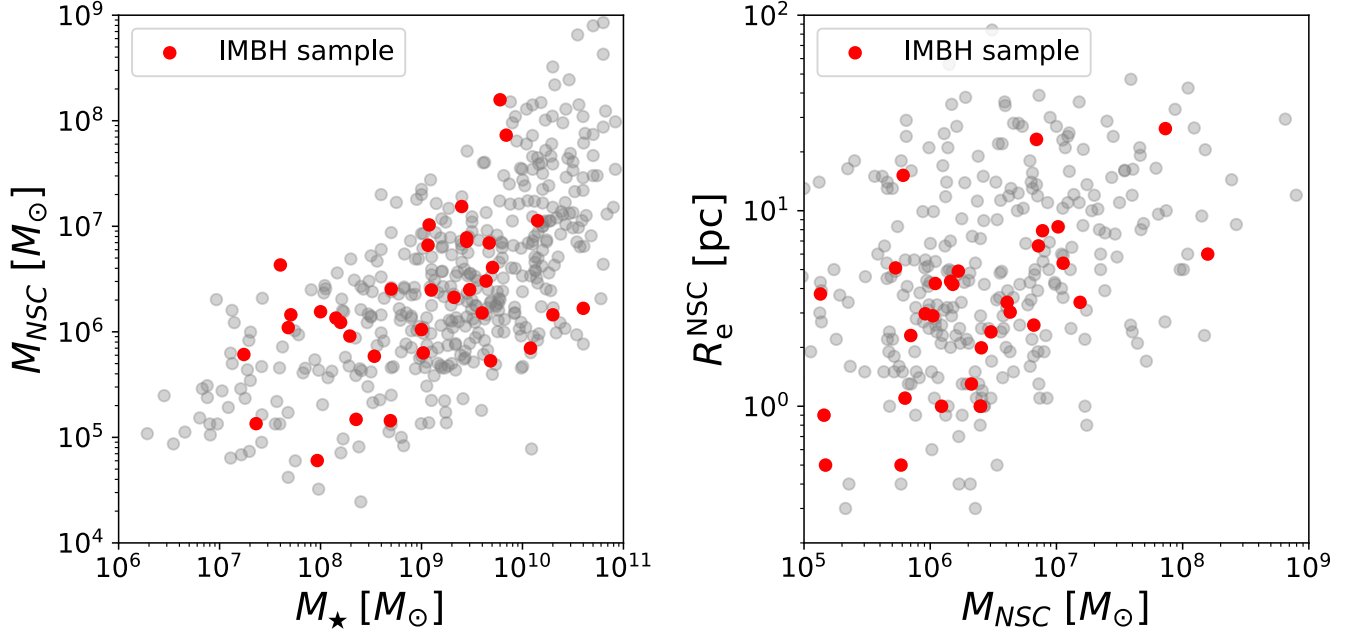


Figure 3. Left: The M_\star – M_{NSC} relation for galaxies in which galaxy and NSC masses are available regardless of their Hubble types. The compilation of dynamical and spectroscopically modeled NSC masses from P. Erwin & D. A. Gadotti (2012), I. Y. Georgiev et al. (2016), C. Spengler et al. (2017), Y. Ordenes-Briceño et al. (2018), and R. Sánchez-Janssen et al. (2019). **Right:** The (M_{NSC}, R_e) distribution for galaxies in which their NSC's mass and effective radius are available. The data are taken from C. J. Walcher et al. (2005), P. Côté et al. (2006), J. Rossa et al. (2006), P. Erwin & D. A. Gadotti (2012), M. A. Norris et al. (2014), I. Y. Georgiev et al. (2016), C. Spengler et al. (2017), V. F. Baldassare et al. (2022), and K. Fahrion et al. (2022).

Table 1. Targets selection criteria for low-mass galaxies hosting NSCs

Distant range:	$D \lesssim 10$ Mpc
Galaxies K s-band absolute magnitude:	$-23.5 \lesssim M_K \lesssim -15.4$ mag
Central stellar-velocity dispersion range:	$\sigma_{\star,c} \lesssim 70$ km s $^{-1}$
(peak of NSC, when available)	
Virial dispersion proxy:	$\sigma_{\text{vir}} \lesssim 70$ km s $^{-1}$
ELT Observability (Armazones site):	$ \delta + 24^\circ < 45^\circ$
Galaxy zone of avoidance:	$ b > 8^\circ$

Table 2. Main characteristics of the HARMONI IMBH sample

Galaxy stellar-mass range:	$2 \times 10^7 \lesssim M_\star \lesssim 5 \times 10^{10} M_\odot$
NSC's mass range:	$10^5 \lesssim M_{\text{NSC}} \lesssim 6 \times 10^7 M_\odot$
NSC's effective radius range:	$3 \lesssim R_e \lesssim 27$ pc
#Galaxies in the sample:	$N_{\text{gal}} = 44$
#dwarf Ellipticals ($T \leq -3.5$):	$N_{\text{dE}} = 6$ ($\approx 13\%$)
#Lenticulars ($-3.5 < T \leq -0.5$):	$N_{\text{S0}} = 7$ ($\approx 16\%$)
#Spirals ($-0.5 < T \leq 8$):	$N_{\text{S}} = 27$ ($\approx 60\%$)
#Irregulars:	$N_{\text{Irr}} = 4$ ($\approx 11\%$)

Notes: The galaxy *Hubble* type (T) is defined from HyperLeda: <https://leda.univ-lyon1.fr/search.html>.

The HARMONI IMBH sample covers over four orders of magnitude in stellar mass. Its location on the mass-size diagram is consistent with the region occupied by dwarf and spiral galaxies, lying just below the approximate upper envelope defined by $(R_e/\text{kpc}) = 8 \times [M_\star/(10^{10} M_\odot)]^{0.24}$ (dashed blue line). The distribution resembles that of dwarf galaxies shown in figure 9 of [M. Cappellari et al. \(2013a\)](#).

For galaxies with $M_\star \gtrsim 10^9 M_\odot$, various properties (stellar populations, gas fraction, dark matter fraction, density slope, IMF) tend to correlate with σ_\star on the (M_\star, R_e) diagram (see review by [M. Cappellari 2025](#)). Black hole masses also follow this trend, suggesting co-evolution ([D. Krajnović et al. 2018](#)). However, below $M_\star \approx 10^9 M_\odot$, the relationships between M_{BH} , σ_\star , M_\star , and R_e are poorly understood due to the scarcity of IMBH measurements and limitations of surveys like 2MASS at low masses and small sizes (especially for $\sigma_\star < 30$ km s $^{-1}$). Despite these limitations, the similarity between our sample's distribution and that of other dwarf galaxy samples with reliable R_e measurements suggests our selection is reasonably representative.

Recent studies ([D. D. Nguyen et al. 2018, 2019; J. E. Greene et al. 2020](#)) indicate that IMBHs in low-mass galaxies may deviate from the scaling relations established for more massive galaxies, hinting at different co-evolutionary pathways.

While [M. Mezcua \(2017\)](#) discussed potential offsets in these relations at the low-mass end, observational challenges hinder definitive conclusions. Our HARMONI IMBH survey aims to overcome these limitations by providing high-resolution kinematic data for nearby IMBH candidates, shedding light on the connection between IMBHs and their host galaxies.

3.2. Nuclear star clusters and central massive black holes

Our HARMONI IMBH sample includes galaxies with NSCs. Among them, 31 NSCs have known masses and effective radii falling within the ranges of $10^5 \lesssim M_{\text{NSC}} \lesssim 10^8 M_\odot$ and $3 \lesssim R_e^{\text{NSC}} \lesssim 27$ pc, respectively. For the remaining NSCs, this information is unavailable. We have compiled data on these NSCs and their host galaxies' properties in [Figure 3](#) alongside with those obtained from literature, including both photometric and spectroscopic surveys.

Out of the 44 selected targets, two IMBHs were estimated through the VLT/SINFONI stellar kinematics: NGC 5102 with $M_{\text{BH}} \approx 9.1 \times 10^5 M_\odot$ and NGC 5206 with $M_{\text{BH}} \approx 6.3 \times 10^5 M_\odot$ ([D. D. Nguyen et al. 2018, 2019](#)). [D. D. Nguyen et al. \(2022\)](#) found a firm signature of an IMBH with $3 \times 10^5 \lesssim M_{\text{BH}} \lesssim 4.3 \times 10^6 M_\odot$ in NGC 3593 based on the ALMA observation of circumnuclear CO(2-1)-molecular gas disc. Additional dynamical models presented in [N. Neumayer & C. J. Walcher \(2012\)](#) suggested that the IMBH in NGC 300, with kinematics measured from VLT/UVES spectra ([C. J. Walcher et al. 2005](#)), likely has a $M_{\text{BH}} < 10^5 M_\odot$. Similarly, the IMBH in NGC 3621, with kinematics measured from the Keck Echellette Spectrograph ([A. J. Barth et al. 2002](#)), suggest a $M_{\text{BH}} < 3 \times 10^6 M_\odot$ ([A. J. Barth et al. 2009](#)).

In the regime of dwarf galaxies with $M_\star < 7 \times 10^9 M_\odot$, the behavior of the M_{BH} –galaxy correlations remain largely unconstrained. It strongly depends on the mass distribution of the currently elusive IMBH population found in the nearby universe (e.g., [M. Mezcua 2017](#)). Recent work by [D. D. Nguyen et al. \(2019\)](#) also provided evidence that the dynamical M_{BH} of five IMBHs in a sample of early-type galaxies within 3.5 Mpc, fall well below the predictions from the [J. Kormendy & L. C. Ho \(2013\)](#), [N. Sahu et al. \(2019\)](#), and [J. E. Greene et al. \(2020\)](#) $M_{\text{BH}}-\sigma_\star$ and $M_{\text{BH}}-M_{\text{bulge}}$ relations.

3.3. Simulated targets

We created mock integral field spectrograph (IFS) observations with HSIM for two dwarf galaxies with NSCs: NGC 300 and NGC 3115, which are located at 2.2 Mpc ([B. F. Williams et al. 2013](#)) and 9.7 Mpc ([H. Jerjen et al. 2000b,a; I. D. Karachentsev et al. 2004](#)), respectively. These galaxies lie at the extreme ranges of our distance selection and are meant to represent our HARMONI IMBH survey's overall characteristics.

NGC 300 is a SA(s)d galaxy, which inclination $i = (42.3 \pm 3.0)^\circ$ ([S. C. Kim et al. 2004](#)), lacks of a bulge ([G. Bono et al.](#)

2010), and has a total stellar mass of $M_\star \approx 2.2 \times 10^9 M_\odot$ (N. Kacharov et al. 2018). The galaxy exhibits a steadily increasing size of its NSC from ultraviolet (UV) to infrared (IR) wavelengths (D. J. Carson et al. 2015), which has a central velocity dispersion of $\sigma_\star = 13.3 \pm 2.0 \text{ km s}^{-1}$ and a dynamical mass of $M_{\text{NSC}} \approx 10^6 M_\odot$, determined from the VLT/UVES spectroscopy (C. J. Walcher et al. 2005), or $\sigma_\star = 13.3 \pm 0.3 \text{ km s}^{-1}$ when measured from the VLT/X-Shooter spectroscopy (N. Kacharov et al. 2018).

The Jeans Anisotropic Model (JAM, M. Cappellari 2008) of the VLT/UVES stellar kinematics measurements (C. J. Walcher et al. 2005) found a $M/L_I \approx 0.6 (M_\odot/L_\odot)$ and suggested an upper limit of $M_{\text{BH}} < 10^5 M_\odot$ (or $\approx 10\%$ of M_{NSC}) for its IMBH, while its best-fit estimate is $M_{\text{BH}} \approx 10^2 M_\odot$ (N. Neumayer & C. J. Walcher 2012).

The star formation history (SFH) of NGC 300's NSC had been independently analyzed by C. J. Walcher et al. (2006) and N. Kacharov et al. (2018), utilizing different spectra, spectral ranges, and simple stellar population (SSP) models. Their findings reveal a relatively consistent stellar population. More than 50% of the stars in the NSC formed over 5 Gyr ago with low metallicity ($[\text{Fe}/\text{H}] \sim -1 \text{ dex}$). Subsequent star formation episodes involving young populations ($\approx 10 \text{ Myr}$) occurred until a few hundred million years ago, resulting in solar metallicity of 1 Gyr ago. **Despite these later episodes, their contributions remain modest, accounting for only 10% of the total luminosity and 1% of the total stellar mass.** There is no evidence of emission lines in the spectra implies that the contribution of a very young population in NGC 300's NSC is likely from an extended horizontal branch (C. Conroy et al. 2018) or blue straggler stars (R. P. Schiavon 2007).

NGC 3115 dw01 (PGC029300) is classified as a dwarf elliptical (dE; H. Jerjen et al. 2000a; B. R. Parodi et al. 2002) with $M_\star \approx 8.9 \times 10^8 M_\odot$ determined from its $B - V$ colour. The galaxy hosts an NSC with $R_e^{\text{NSC}} \approx 6.61 \pm 0.09 \text{ pc}$ and $M_{\text{NSC}} \approx 7.2 \times 10^6 M_\odot$, constrained from the *HST*/WFPC2 F814W images with a photometric $M/L_{\text{F814W}} \approx 1.4 (M_\odot/L_\odot)$ (R. Pechetti et al. 2020). Stellar kinematic measurements with the echelle spectrograph of the 4-meter telescope at Cerro Tololo Inter-American Observatory (CITO) yield a central velocity dispersion of $\sigma_\star = 32 \pm 5 \text{ km s}^{-1}$ in the NSC. However, more global measurements within the galaxy's effective radius ($R_e \approx 1.2 \text{ kpc}$) result in a value of $\sigma_e \approx 45 \text{ km s}^{-1}$ (R. C. Peterson & N. Caldwell 1993).

Due to the absence of stellar populations and SFH in NGC 3115 dw01, we opted for simplicity in our HSIM IFS simulations. We employed Stellar Population Synthesis (SPS) spectra with a fixed age of 5 Gyr, Solar metallicity (z002), and inclination $i = 42^\circ$, which are similar to the nucleus of NGC 300.

4. DYNAMICAL MODEL

4.1. Jeans Anisotropic Modelling

NSCs in dwarf galaxies, such as those targeted by our HARMONI IMBH survey, frequently display significant rotation (e.g., A. Seth et al. 2008; A. C. Seth et al. 2010; D. D. Nguyen et al. 2018; S. Thater et al. 2023). Observed ratios of rotational velocity to stellar velocity dispersion (V/σ_\star) typically range from 0.1 to 0.6 (F. Pinna et al. 2021), indicating substantial ordered motion.

To model the kinematics of these rotating systems, we utilize the JAM (M. Cappellari 2008, 2020). Specifically, we adopt the JAM variant that assumes cylindrical alignment of the velocity ellipsoid (JAM_{cyl}), an approach proven effective for modeling rotating NSCs (e.g., M. Hartmann et al. 2011, figure 4) and rapidly rotating galaxies (e.g., M. Cappellari 2016, figure 10).

We implemented these models using the JAMPy packageⁱⁱ. In the `JAM.AXI.PROJ` procedure, we set `align='cyl'` to enforce cylindrical alignment. We further assumed an oblate velocity ellipsoid, where the vertical dispersion differs from the equal radial and tangential dispersions ($\sigma_z \neq \sigma_R = \sigma_\phi$), by setting `gamma=0` and `kappa=1`.

A crucial aspect of this study is probing radii very close to the central BH. To accurately capture the BH's gravitational influence in this regime, we set the keyword `analytic_los=False`. This treats the BH potential as a point mass, enabling the analytical calculation of the intrinsic second velocity moments ($\langle \sigma_z^2 \rangle$ and $\langle \sigma_\phi^2 \rangle$) in its vicinity, rather than using a Gaussian approximation. These analytically derived intrinsic moments are then numerically integrated along the line-of-sight to predict the observable kinematics.

4.2. Predicted velocity dispersion profiles

Before presenting detailed simulations of the predicted kinematics due to IMBHs of different M_{NSC} , here we try to understand the quantitative behaviour we should expect. This is important because we have to decide how to extrapolate the inner surface brightness profile of NSCs, at radii much smaller than resolvable with *HST*.

In their classic paper, S. Tremaine et al. (1994) studied the qualitative behaviour of the projected velocity dispersion (σ_p) profiles in elliptical galaxies with central SMBHs. They described the predicted velocity-dispersion profile of isotropic galaxy models described by a double power-law density profile, with general inner density $\rho(r) \propto r^{-\gamma}$ and fixed outer density $\rho(r) \propto r^{-4}$ (W. Dehnen 1993), and a smooth transition between these two power-law regimes. Where, γ is the power-law index.

ⁱⁱ v7.2.0; available from <https://pypi.org/project/jampy/>

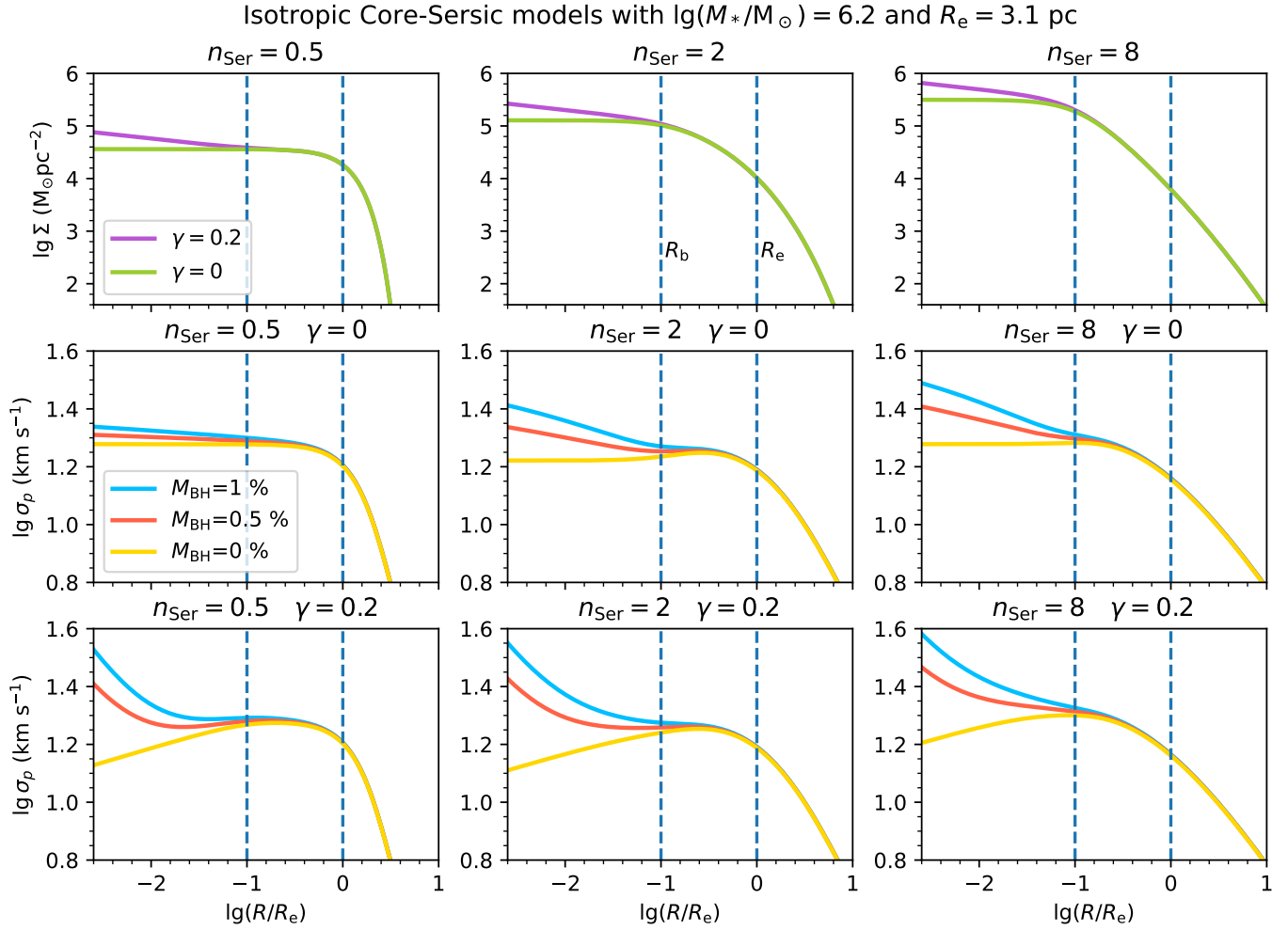


Figure 4. Atlas of the central surface-mass density (Σ , three top-row panels) and projected velocity dispersion (σ_p , the three middle-row and bottom-row panels) profiles resolved deeply into the resolvable region of HARMONI, which are predicted by various values of the Sérsic index (n_{Ser}) and the core inner slope (γ) of the isotropic Core-Sérsic model. These theoretical profiles can be used to describe the qualitative behaviour of the σ_p of stellar systems spanning from galaxies to NSC. For illustration, the values of Σ and σ_p were normalized to approximate the median values of the mass and radii of NSC (see text). We utilized three different Sérsic indices – including the low $n_{\text{Ser}} = 0.5$ (corresponding to the Gaussian profile), intermediate $n_{\text{Ser}} = 2$, and high $n_{\text{Ser}} = 8$ of the Sérsic-index value – and two different values of the core inner slope: $\gamma = 0$ (green line) and $\gamma = 0.2$ (purple line). To illustrate the effects of central IMBHs having at the central region of the projected velocity dispersion profiles, we modeled with three different BH masses: $M_{\text{BH}} = 0\%$ of M_{NSC} (no BH, yellow line), $M_{\text{BH}} = 0.5\%$ of M_{NSC} (or $M_{\text{BH}} = 8 \times 10^3 M_{\odot}$, red line), and $M_{\text{BH}} = 1\%$ of M_{NSC} (or $M_{\text{BH}} = 1.6 \times 10^4 M_{\odot}$, blue line). The two vertically dashed lines represent the break radius (R_b , inner line) and the effective radius (R_e , outer line) of the NSC’s isotropic Core-Sérsic model. The core inner slope γ control the inner behaviour of the central surface-mass density and the projected velocity dispersion profiles, while the Sérsic index describes the outer profile.

Here, we illustrate the behaviour of the velocity dispersion for the more general Core-Sérsic model (A. W. Graham et al. 2003; I. Trujillo et al. 2004), which parametrizes the projected surface brightness (not the intrinsic density) as follows

$$I(R) = I' \left[1 + \left(\frac{R_b}{R} \right)^\alpha \right]^{\gamma/\alpha} \exp \left[-b_{n_{\text{Ser}}} \left(\frac{R^\alpha + R_b^\alpha}{R_e^\alpha} \right)^{1/(\alpha n_{\text{Ser}})} \right] \quad (1)$$

where I' is the normalization and $b_{n_{\text{Ser}}} = Q^{-1}(2n_{\text{Ser}}, 1/2)$ is a factor defined in such a way that the half-light radius R_e encloses half of the total light of the Sérsic profile (without the core), and Q^{-1} is the inverse of the regularized incomplete

gamma function¹² (K. Zhu et al. 2025, eq. 14). Here, n_{Ser} is the Sérsic index, which controls the shape of the outer Sérsic part. R_b is the break radius, which is the point at which the surface brightness changes from the outer Sérsic part to the inner power-law regime of the profile. The intensity I_b at the break radius is given by Equation 1 with $R = R_b$ (we give it in magnitudes μ_b in Table 4). α is the sharpness parameter that controls the sharpness of the transition between the outer Sérsic and inner power-law regimes. Outside the inner break

¹² Implemented in `scipy.special.gammainccinv`

Table 3. *HST/WFPC2* PC (PC1) observations (1 pixel = 0''.045) of the two galaxies hosting NSCs chosen to perform *HISM* simulations

Galaxy name	α (J2000) (h:m:s)	δ (J2000) (deg : ' : '')	UT Date	PID	PI	Filter	Exptime (s)	Zeropoint (mag)	A_λ (mag)
(1)	(2)	(3)	(4)	(5)	(6)	(7)	(8)	(9)	(10)
NGC 300	50:54:53.477	-37:41:03.31	2001 May 06	8599	Boeker	F814W	3×213	23.758	0.025
NGC 3115 dw01	10:05:41.599	-07:58:53.40	1995 Nov. 29	5999	Phillips	F814W	2×160	23.758	0.050
	10:05:41.599	-07:58:53.40	1995 Nov. 29	5999	Phillips	F547M	1×160	23.781	0.025

Notes: Column 1: The galaxy name. Columns 2 and 3: The galaxy's position (R.A. and Decl.) from *HST*/HLA. Column 4: The date when observations were performed. Columns 5 and 6: The project (PID) and principal investigator (PI) identification numbers. Column 7: The broad-band filter used to take the data. Column 8: The exposure times of the observations show the number of exposures multiplied by the time spent on source for each exposure. Columns 9 and 10: The photometric zero-point and extinction value in each filter.

at radius $R > R_b$ this is a [J. L. Sersic \(1968\)](#) profile of projected half-light radius R_e , but gradually transitions to a power law surface brightness $\Sigma(R) \propto R^{-\gamma}$ at smaller radii $R \ll R_b$.

We adopt the Core-Sérsic profile because it can describe the profile of real NSCs. However, we allow for a cusp in the inner slope to parametrize our ignorance of the profile of NSC at radii which are inaccessible with current instruments, but which will become observable with the ELT. In our analysis, we model the NSC in isolation, even though they are embedded in the large-scale gravitational potential of the host galaxy. However, the latter has an insignificant effect on the predicted σ_p profiles at the centre of the NSC. In particular, in our case, R_e represents the size of the NSC, not the size of the host galaxy.

To compute the predictions for the σ_p profiles we first used the `MGE.FIT_1D` procedure in the `MGEFit` package¹³ ([M. Cappellari 2002](#)) to fit the Core-Sérsic profiles in the range $R_b/100 < R < 20R_e$ using 20 Gaussians. Then used the `JAM_SPH_PROJ` procedure in the `JAMPy` package (see footnote 7; [M. Cappellari 2008, 2020](#)) to compute the isotropic velocity dispersion for different values of the Sérsic index n_{Ser} and the core inner slope γ . In all our tests we adopted a fixed $\alpha = 2$ value, which produces a smooth transition between the outer Sérsic and inner power-law profiles. We show the results in [Figure 4](#). The qualitative behaviour of the profiles is independent of the absolute normalization of their total masses M_\star and R_e . It can be applied unchanged to describe the σ_p profile of NSC or giant elliptical galaxies. However, in this Fig., we adopt as mass and size reference the values $\lg(M_{\text{NSC}}/M_\odot) = 6.2$ and $R_e = 3.1$ pc. These are the median values for NSC of late-type galaxies with $M_\star < 10^9 M_\odot$ ([N. Neumayer et al. 2020](#), table 2).

In [Figure 4](#), we adopt either no BH, or BH masses of 0.5% and 1% of the mass of the NSC. These values are the same characteristic fractions observed for normal galaxies ([J. Kormendy & L. C. Ho 2013](#), eq. 11). However, nothing is

currently known about the mass of IMBH in NSC. In fact, NSCs may not have IMBHs at all, or they may be dominated by the IMBH mass. But the qualitative behaviour remains unchanged.

For $\gamma > 0$ and without BHs the σ_p profile decreases towards the nucleus, regardless of n_{Ser} . This is a well-known general feature of realistic galaxy models. It appeared in puzzling contrast with the early observations ([J. Binney 1980](#)) until it became clear that all massive galaxies contain SMBHs. With an IMBH, the σ_p profile starts increasing towards the centre, inside the IMBH's SOI, asymptotically approaching the Keplerian rise $\sigma_p \propto R^{-1/2}$ (for $0 < \gamma < 2$), regardless of the profile slope, as shown by [S. Tremaine et al. \(1994, eq. 52\)](#).

[S. Tremaine et al. \(1994\)](#) also pointed out that¹⁴, when $\gamma = 0$, namely when the inner surface brightness approaches a constant value, the asymptotic behaviour becomes qualitatively different. In that case, without an IMBH, the σ_p profile approaches a constant positive value, instead of dropping towards zero. We confirm the behaviour for the Core-Sérsic profile with a flat inner core regardless of n_{Ser} . With an IMBH, the σ_p profile rises towards the centre, but it does so less steeply than the $\gamma > 0$ case, as predicted for the double power-law models.

What is new in this study is the fact that we explore a range of Sérsic indices, including the extreme case $n_{\text{Ser}} = 1/2$, which corresponds to a Gaussian profile, when $\gamma = 0$. We find that in this extreme situation, the σ_p profile becomes only weakly sensitive to the M_{BH} . This is quite important for the present study, because we are approximating the surface brightness of the NSC using the multi-Gaussian expansion method (MGE, [E. Emsellem et al. 1994](#); [M. Cappellari 2002](#)). And we are fitting photometric data that have a much lower resolution than the one we will be able to obtain with the ELT. This implies that our model may end up being described by a Gaussian in the central parts, well inside the width of the PSF

¹⁴ [S. Tremaine et al. \(1994\)](#) studied densities $\rho(r) \propto r^{-\gamma'}$, which we convert to the corresponding surface brightness $\Sigma(R) \propto R^{-\gamma}$ using $\gamma = \gamma' + 1$.

¹³ v5.0 of the Python package from <https://pypi.org/project/mgefit/>

of our photometry. This is precisely the key region, near the BH, where we want to produce an accurate σ_p prediction.

In practice, we should not worry about NSC having flat surface brightness profiles and isotropic orbital distributions. This is because such models are unphysical and cannot exist in real stellar systems. Instead, if an IMBH is present, isotropic models produce a density cusp that rises as $\rho(r) \propto r^{-1/2}$ near the BH (S. Tremaine et al. 1994), or $\Sigma(R) \propto R^{-3/2}$ in surface brightness (see also R. P. van der Marel 1999). One would require extreme tangential anisotropies for flat profiles $\gamma = 0$ to be allowed, as indicated by the cusp-slope vs central anisotropy theorem (J. H. An & N. W. Evans 2006). We have no reason to think NSC satisfies this requirement. However, what is important is that, lacking real high-resolution photometry at the resolution of HARMONI, we extrapolate the observed surface brightness using a non-zero inner power slope, when constructing the mock kinematics of the NSCs. Failing to do so, we would generate predictions for σ_p profiles that vastly underestimate the central rise that we expect from high-resolution HARMONI observations.

4.3. MARCS synthetic library of stellar spectra

To create mock HSIM IFS simulations, we required stellar population synthesis (SPS) spectra¹⁵ that contain information about the stellar populations (C. Maraston & G. Strömbäck 2011), based on the Model Atmospheres with a Radiative and Convective Scheme (MARCS) synthetic library of theoretical spectra, originally developed by B. Gustafsson et al. (2008). Although MARCS synthetic library spectra are not as reliable as an empirical stellar library, when expecting the stellar kinematics of real galaxies, its minor imperfections are not an issue when generating mock spectra. The library offers broad wavelength coverage spanning from 1,300 Å to 20 μm at high spectral resolution with $\sigma = 6.4 \text{ km s}^{-1}$ (equivalent to $R = \lambda/\Delta\lambda \sim 20,000$). We assumed a Salpeter IMF, an age of 5 Gyr, and Solar metallicity (z002) for both NGC 300's NSC (N. Kacharov et al. 2018) and NGC 3115 dw01 (subsection 3.3). The SPS spectra were truncated within the wavelength range of 1.0–2.5 μm to match the HARMONI/J, H, K, H-high, K-short, and K-long gratings.

5. GALAXY PHOTOMETRY MODELS

5.1. HST images and their PSF models

We summarized the *HST*/Wide Field and Planetary Camera 2 (WFPC2) Planetary Camera (PC) images used in this study in Table 3. We accessed the reduced and drizzled images from the *HST*/Hubble Legacy Archive (HLA), with a pixel scale of 0''.045.

For our analysis, we need the PSFs to deconvolve the *HST* profiles into their intrinsic forms (subsection 5.2). We thus

employed the simulated images of the *HST*/WFPC2 PSFs in each filter using `tiny1` and `tiny2` routines within the Tiny Tim software package¹⁶ (J. Krist 1995; J. E. Krist et al. 2011), which creates a model *HST* PSF based on the instrument, detector chip, detector chip position, and filter used in the observations. To ensure that the model PSFs were processed in the same way as the *HST* images, we produced individual versions of each PSF corresponding to their realistic exposure in each filter and each galaxy on a subsampled grid with sub-pixel offsets, using the same four-point box dither pattern as the *HST*/WFPC2 exposures. Next, in order to account for the effect of electrons leaking into neighbouring pixels on the CCD, each model PSF was convolved with the appropriate charge diffusion kernel. The same filters set of PSFs of each galaxy were then combined and resampled onto a final grid with a pixel size of 0''.045 using `Drizzelpac/AstroDrizzle` (R. J. Avila et al. 2012) to produce final the PSF image.

5.2. Surface brightness profiles and galaxy mass models

We used the *HST* data and their simulated PSFs in subsection 5.1 to measure the galaxies' surface brightness profiles. We fitted the model of Equation 1 and extrapolated these profiles using the best-fit parameters to create our mock surface brightness at higher resolution than *HST*.

Our initial step involved extracting the one-dimensional (1D) surface brightness of NGC 300 and NGC 3115 dw01 by employing the Image Reduction and Analysis Facility (IRAF) `ellipse` task (R. I. Jedrzejewski 1987) to conduct this task. The `ellipse` routine systematically integrated the flux of stars within concentric annuli, allowing for variations in position angles and ellipticities along the semi-major axis of the galaxy, although fixing these two parameters did not yield any significant changes in our results. Before extracting the intrinsically 1D surface brightness profiles in IRAF for each image, we first performed spatial deconvolution using the corresponding PSF image generated in subsection 5.1. Subsequently, we converted the average flux within each annulus, measured in counts/s, into surface brightness expressed in mag arcsec⁻². This conversion was carried out using the photometric information derived from the broad-band filters and camera specifications (Table 3). The large-scale profile of NGC 300 ($r > 2''$) was taken from N. Neumayer et al. (2020), which was extracted from the Wide Field Imager (WFI) observed in *R* band with the MPG/ESO 2.2-metre telescope¹⁷. Here, we calibrated our inner F814W profile ($r \leq 2''$) with the same *HST* profile from D. J. Carson et al. (2015) using the AB magnitude system.

Next, we applied analytical functions to fit these 1D surface brightness of NGC 300 and NGC 3115 dw01. These functions

¹⁵ Available from <https://marcs.astro.uu.se/>

¹⁶ <https://github.com/spacetelescope/tinytim>

¹⁷ Available at <https://www.eso.org/public/images/eso1037a/>

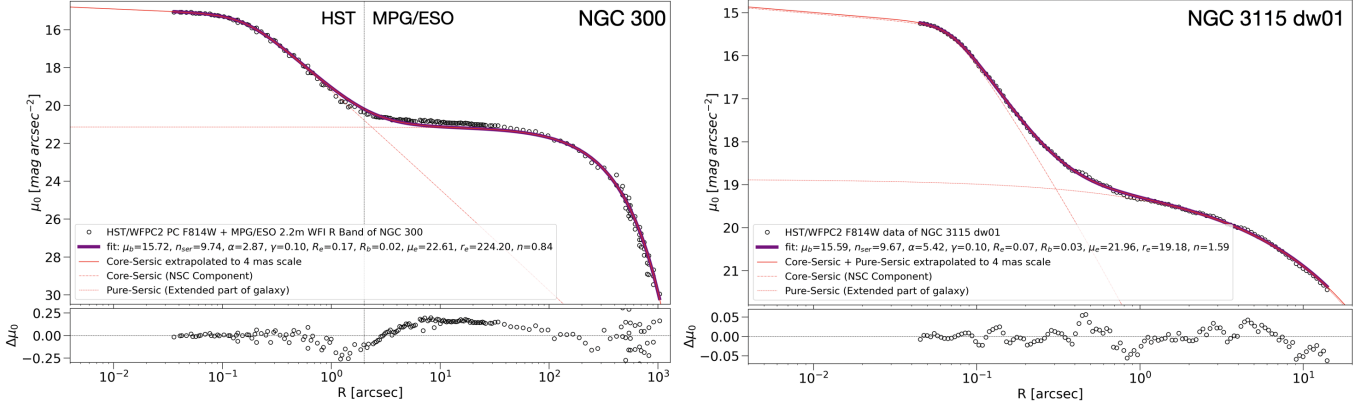


Figure 5. Upper panels: The *HST*/WFPC2 F814W surface brightness of NGC 300 (left) and NGC 3115 dw01 (right) constructed from *IRAF* ellipse are plotted in open black dots, while their best-fit Core-Sérsic + pure-Sérsic surface brightness are plotted in purple solid-thick lines. Their best-fitting parameters are shown in the legends. Here, the Core-Sérsic profile is plotted in a red dashed line, while the pure-Sérsic profile is depicted in a red dotted line. For $r < 0''.045$, these surface brightness are extrapolated to the 4 mas scale required for this IMBH survey’s imaging with MICADO (red solid-thin lines). **For NGC 300, the vertical black line indicates the radius at which we combined the narrow-field *HST*/WFPC2 F814W data with the wide-field MPG/ESO 2.2-m WFI R-band data.** **Lower panels:** The differences, data – model, between the *IRAF* ellipse surface brightness and their corresponding best-fit Core-Sérsic + pure-Sérsic models illustrate the fit’s goodness.

Table 4. Best-fit Core-Sérsic ($\gamma = 0.1$) + pure-Sérsic parameters of the *HST*/WFPC2 surface brightness profiles.

Galaxy name	Filter	μ_b (mag/arcsec $^{-2}$)	n_{Ser}	α	R_e (arcsec)	R_b (arcsec)	μ_e (mag/arcsec $^{-2}$)	R_e (arcsec)	n
(1)	(2)	(3)	(4)	(5)	(6)	(7)	(8)	(9)	(10)
NGC 300	F814W	15.72 ± 0.22	9.74 ± 0.05	2.87 ± 0.05	0.17 ± 0.03	0.02 ± 0.01	22.61 ± 0.45	224.20 ± 1.52	0.84 ± 0.11
NGC 3115 dw01	F814W	15.59 ± 0.21	9.67 ± 0.05	5.42 ± 0.12	0.07 ± 0.02	0.03 ± 0.01	21.96 ± 0.20	19.18 ± 0.25	1.59 ± 0.07
	F547M	16.44 ± 0.25	9.51 ± 0.06	5.27 ± 0.15	0.06 ± 0.02	0.03 ± 0.01	23.01 ± 0.24	18.73 ± 0.27	1.71 ± 0.05

Notes: Column 1: The galaxy name. Column 2: The board-band filter used to take the data. Columns (3–7): The best-fit parameters of the Core-Sérsic profile for the NSC components, orderly the surface brightness density at the break radius, the Sérsic index of the outer Sérsic part, the sharpness parameter which indicates how fast/slow the profile changes from the outer Sérsic to inner power-law regime, the break radius where the profile changes from the outer Sérsic part to the inner power-law part, and the effective radius of the outer Sérsic part. Columns (8–10): The best-fit parameters of the pure-Sérsic profile for the galaxies’ extended parts, orderly the surface brightness density at the effective radius, the effective radius, and the Sérsic index.

involved combinations of a Core-Sérsic model (A. W. Graham et al. 2003; I. Trujillo et al. 2004) and a pure-Sérsic model (J. L. Sersic 1968). Here, while the Core-Sérsic model is used to fit the NSC component, the pure-Sérsic model was applied to fit the extended component of the galaxy. This model fit also gives the Sérsic index (n_{Ser}) of the NSC, which is useful to predict the kinematics trend (see subsection 4.2). Furthermore, the pixel size of the *HST*/WFPC2 is 45 mas. This means that a single pixel contains over 60 spaxels of the proposed 10 mas mode adopted for this HARMONI IMBH survey. In fact, it is more than 11 times larger than the pixel size for ELT/MICADO images (i.e., 4 mas). We thus do not know the stellar profile at this scale, and this region is indeed embedded deeply in the core of an NSC, which is controlled by the power-law behaviour of the Core-Sérsic model. In this work, we adopted the power-law index $\gamma = 0.1$ as in N23 for both galaxies, although our tests with varying γ provide $\gamma = 0.08$ for NGC 300 and $\gamma = 0.13$ for NGC 3115 dw01 with their current *HST* 1D surface brightness, implying our

global choice of $\gamma = 0.1$ for mock HARMONI IFS simulation in the subsequent Section is reasonable.

Additionally, the pure J. L. Sersic (1968) model has a form:

$$I(R) = I_e \exp \left\{ -b_n \left[\left(\frac{R}{r_e} \right)^{1/n} - 1 \right] \right\} \quad (2)$$

In which, we denoted n is the Sérsic index of the pure-Sérsic profile to distinguish with that n_{Ser} of the Core-Sérsic profile in equation (1), which controls the degree of curvature of the profile. I_e is the intensity at R_e , which is converted into surface brightness density μ_e shown in the legends of Figure 5 and Table 4.

We applied a non-linear least-squares algorithm using the MPFIT¹⁸ function (C. B. Markwardt 2009) to iteratively fit the combined function of a Core-Sérsic and a pure-Sérsic above for both NGC 300 and NGC 3115 dw01 to their corresponding

¹⁸ Available from <http://purl.com/net/mpfit>

spatially deconvolved profiles, thereby obtaining the best-fit parameters homogeneously. After the fits, we extrapolated the best-fit surface brightness towards the galaxies' centers to a scale of 4 mas required for this IMBH survey's imaging with MICADO (Figure 5). The best-fit parameters and their associated errors derived from these surface brightness fits are saved in Table 4.

Next, we employed these derived parameters to describe the two-dimensional (2D) luminosity density models extrapolated towards the central 4 mas for each galaxy. We assumed a small flattening based on the fact that not all NSCs are perfectly spherical and non-rotating, characterized by the ratio between the semiminor and semimajor axes $q' = b/a \approx 0.9$. This assumption also works for the extended bulge or disk of NGC 3115 dw01 as the galaxy morphology looks round through its *HST* images. However, the extended scale of NGC 300 revealed through the MPG/ESO 2.2-m WFI *R* band image suggests the galaxy's outer part ($r > 2''$) can be approximately assumed as $q' = b/a \approx 0.75$. Subsequently, we approximated these 2D luminosity density models using the MGE method (E. Emsellem et al. 1994; M. Cappellari 2002). This involved using the MGE.FIT_SECTORS routine from the MGEFit package (M. Cappellari 2002) and included 15 Gaussians spanning radii from 4 mas to $\approx 1000''$ for NGC 300 and $\approx 15''$ for NGC 3115 dw01, as listed in Table 7.

Finally, we converted the luminosity surface density into mass surface density by assuming a constant mass-to-light ratio, $M/L_{\text{F814W,dyn}} \approx M/L_I \approx 0.6 (M_\odot/L_\odot)$ for NGC 300 (N. Neumayer & C. J. Walcher 2012) and $M/L_{\text{F814W,phot}} \approx M/L_I \approx 1.4 (M_\odot/L_\odot)$ for NGC 3115 dw01 derived in AB mag (R. Pechetti et al. 2020). To simplify our HARMONI IFS simulations, we disregarded (1) potential variations in M/L_I due to differences in stellar populations (e.g., M. Mitzkus et al. 2017) and (2) the distribution of dark matter halos (J. F. Navarro et al. 1996), given that the stellar density is expected to be orders of magnitude larger in the NSC. We focus on the stellar kinematics within the central part of $0''.4 \times 0''.4$ of HARMONI field-of-view (FOV), where the central BH's and NSC's potential is the dominant factor.

5.3. Effect of individual stars

A critical consideration for our HARMONI IMBH survey, with its proposed 10 mas spaxel resolution, is ensuring a sufficient number of stars within each spaxel. This is necessary to treat the stellar distribution as continuous rather than needing to model individual stars, a challenge that increases with closer targets. To evaluate this, we estimated the average number of stars per 10 mas spaxel using the surface brightness profiles provided in Figure 5. Our method involved converting the surface brightness density from mag arcsec $^{-2}$ to surface luminosity density in L_\odot arcsec $^{-2}$, and then calculating the average number of stars within the 10 mas spaxel area based on this luminosity density.

Our findings are illustrated in Figure 6, which shows the estimated number of stars per 10 mas spaxel versus radius for NGC 300 and NGC 3115 dw01. In NGC 300, the stellar density per spaxel falls dramatically from over 100 in the nucleus to approximately one star at radii exceeding 200 spaxels (equivalent to the $\approx 2''.15$ extent of our HARMONI FOV). NGC 3115 dw01, being significantly denser, shows a decrease from about 5000 central stars per spaxel to around 700 within the FOV. Notably, even in the difficult case of NGC 300 – a close and well-resolved target – the central $0''.4 \times 0''.4$ region maintains a density of roughly 100 stars per 10 mas spaxel, supporting the validity of a continuous distribution assumption in such dense central areas. It is important to understand that this issue of discrete stars per single spaxel is primarily a concern only for the few innermost spaxels. For radii further out, we will employ Voronoi binning (see footnote 13, subsection 6.3). This technique combines adjacent spaxels into larger spatial bins, thereby guaranteeing a sufficient number of stars within each bin for accurate integrated light measurements.

6. HARMONI IFS SIMULATIONS

First, we describe the HARMONI instrument on ELT and HARMONI Simulator (HSIM) in subsection 6.1. Next, we combine the mass models of NGC 300 and NGC 3115 dw01 constructed in section 5 with HSIM to simulate their *J* (1.046–1.324 μm), *H* (1.435–1.815 μm), *K* (1.951–2.469 μm), *H*-high (1.538–1.678 μm), *K*-short (2.017–2.201 μm), and *K*-long (2.199–2.400 μm) mock datacubes in subsection 6.2. Finally, we present the extracted kinematics from these mock HSIM cubes in subsection 6.3.

6.1. HARMONI instrument on the ELT and HSIM simulator

HARMONI is the first optical and NIR IFS ranging from 0.458 to 2.469 μm and offering IFS at four distinct spatial scales (i.e., 4×4 , 10×10 , 20×20 , and 30×60 mas 2) and three spectral resolving powers (i.e., $\lambda/\Delta\lambda \approx 3, 300, \approx 7,100$ and $\approx 17,400$) through 13 gratings. As integrated from 798 hexagonal segments with 1.4-meter diameter, HARMONI will gather spectral data from a field of 152×214 spaxels ($\approx 32,530$ spectra) over a 39-meter primary mirror equipped with laser guide star AO. We note that HARMONI is currently undergoing a Rescoping Science Evaluation, and its detailed specifications may change. In this work, we use the last available stable specifications, as the instrument characteristics are not yet sufficiently settled to incorporate the latest potential changes into our simulations.

N23 demonstrated that HARMONI could robustly measure SMBH masses for massive galaxies up to $z \lesssim 0.3$. Its scientific explorations can also extend from diffraction-limited

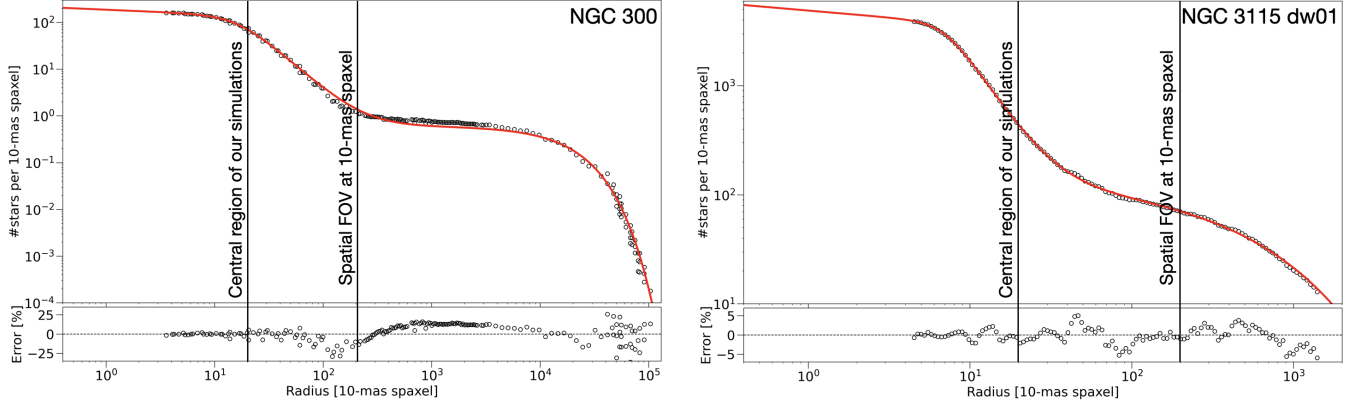


Figure 6. The upper panels present the estimated number of stars per 10 mas spaxel for the nuclei of NGC 300 (left) and NGC 3115 dw01 (right). The data points derived directly from the SB in Figure 5 are shown in black circles at their best-fit models are shown in red lines. The lower panels of the figure display the residuals, calculated as $(\text{data} - \text{mode})$, which provide a relative error in our estimation, helping to assess the accuracy of our calculations. The inner vertical solid line represents our spatially central regions of HARMONI simulations in subsection 6.2 ($0.^{\circ}4 \times 0.^{\circ}4$), while that same outer line illustrates the full spatial FOV of HARMONI at our chosen 10-mas spaxel survey ($2.^{\circ}15 \times 1.^{\circ}54$; see S. Zieleniewski et al. 2015).

imaging to ultrasensitive observations, including the study of morphology, spatially resolved populations and kinematics, abundances, and line ratios in distant sources, even in regions of faint SB (N. A. Thatte et al. 2016, 2020).

S. Zieleniewski et al. (2015) introduced a sophisticated HSIM pipeline designed for simulating observations with the HARMONI instrument on the ELT. This software takes as input high spectral and spatial resolution IFS cubes without random noise (generated in subsection 6.2) and incorporates the physical properties of celestial targets to generate simulated data cubes. In the simulation process, HSIM factors in the complex atmospheric conditions at the ELT’s observation site and realistic detector statistics/readout, thereby producing data that mimics actual observations. This paper is primarily focused on utilizing HARMONI’s LTAO IFS simulations to probe the nucleus stellar kinematics of nearby dwarf galaxies. We aim to search for the kinematic signatures of IMBHs and estimate their masses. These simulations also delineate the boundaries within which HARMONI can deliver feasible observables. Furthermore, they provide invaluable scientific insights, offering guidance for future research efforts that will use actual data obtained with HARMONI.

6.2. Simulations of Mock IFS Datacubes

We generated mock HARMONI IFS datacubes using the HSIM pipeline. These simulations were conducted for three medium-resolution gratings (J, H, K , with $\lambda/\Delta\lambda \approx 7100$ and $\sigma_{\text{instr}} \approx 18 \text{ km s}^{-1}$) and three high-resolution gratings ($H\text{-high}, K\text{-short}, K\text{-long}$, with $\lambda/\Delta\lambda \approx 17400$ and $\sigma_{\text{instr}} \approx 6 \text{ km s}^{-1}$). The primary goal of these simulations was to assess the impact of kinematic errors and evaluate the feasibility of using different stellar spectral features for determining the black hole mass (M_{BH}).

Table 5. Mock HSIM IFS datacubes (DIT = 15 min.)

Galaxy name	HSIM band	Exptime (minutes)	Sensitivity (minutes)
(1)	(2)	(3)	(4)
NGC 300	J	180=DIT×12	90=DIT×6
	$H, H\text{-high}$	210=DIT×14	120=DIT×8
	$K, K\text{-short}, K\text{-long}$	240=DIT×16	150=DIT×10
NGC 3115 dw01	J	180=DIT×12	90=DIT×6
	$H, H\text{-high}$	210=DIT×14	120=DIT×8
	$K, K\text{-short}, K\text{-long}$	240=DIT×16	150=DIT×10

Notes: Column 1: the galaxy name. Column 2: HSIM band chosen to perform IFS simulations. Column 3: real exposure time we put in HSIM for our simulated kinematics maps presented in Figure 7 and Figure 8, where the total integration time is determined as DIT×NDIT. Column 4: Sensitivity in terms of exposure time at which we test the lowest limit of S/N from the simulated IFS so that our pPXF still extract accurate kinematics (will be discussed later in subsection 7.3). We should note that the estimated time show in Columns 3 and 4 are the science time on targets without accounting for the target acquisition, overhead, and AO setup time.

As discussed in N23 and A. Crespo Gómez et al. (2021), the K -band spectrum (covering both K -short and K -long) contains several molecular absorption lines crucial for measuring stellar kinematics. Prominent among these are the CO absorption bandheads in the range of 2.29–2.47 μm , such as $^{12}\text{CO}(2-0)$ at 2.293 μm and $^{12}\text{CO}(3-1)$ at 2.312 μm . Additionally, atomic lines like Na I $\lambda 2.207 \mu\text{m}$, Ca I $\lambda 2.263 \mu\text{m}$, and Mg I $\lambda 2.282 \mu\text{m}$ in the K -band are also important for this purpose.

In the H -band (including $H\text{-high}$), a rich set of atomic absorption lines is available (e.g., Mg I $\lambda 1.487, 1.503, 1.575, 1.711 \mu\text{m}$; Fe I $\lambda 1.583 \mu\text{m}$; Si I $\lambda 1.589 \mu\text{m}$). Strong CO absorption features are also present, including $^{12}\text{CO}(3-0) \lambda 1.540 \mu\text{m}$, $^{12}\text{CO}(4-1) \lambda 1.561 \mu\text{m}$, $^{12}\text{CO}(5-2) \lambda 1.577 \mu\text{m}$,

$^{12}\text{CO}(6-3) \lambda 1.602 \mu\text{m}$, $^{12}\text{CO}(7-4) \lambda 1.622 \mu\text{m}$, and $^{12}\text{CO}(8-5) \lambda 1.641 \mu\text{m}$.

Furthermore, promising atomic and molecular absorption lines have been identified in the J -band IFS for potential use in future studies. These lines are primarily sensitive to metallicity and include species like Fe I, Mg I, Si I, and Ti I. Examples include Ti I $\lambda 1.1896, 1.1953 \mu\text{m}$; Si I $\lambda 1.1988, 1.1995, 1.2035, 1.2107 \mu\text{m}$; Mg I $\lambda 1.1831, 1.2087 \mu\text{m}$; and Fe I $\lambda 1.1597, 1.1611, 1.1641, 1.1693, 1.1783, 1.1801, 1.1887, 1.1976 \mu\text{m}$ (J. T. Rayner et al. 2009; M. Lyubenova et al. 2012).

A representative subset of these potential atomic and molecular absorption lines is marked on the six HSIM mock IFS spectra displayed in Figure 13. These lines were selected to guide the determination of the optimal wavelength range for extracting stellar kinematics, specifically aiming to avoid contamination from sky emission (such as OH lines in the J band). For a more exhaustive list and visual representation of these stellar absorption tracers, interested readers are directed to L. Wallace & K. Hinkle (1996, 1997); J. T. Rayner et al. (2009); C. J. Evans et al. (2011); M. Lyubenova et al. (2012); A. Crespo Gómez et al. (2021).

It is important to note that the atomic absorption species and molecular absorption lines observed in the J, H, H -high, K -short, and the blue portion of the K -band IFS generally exhibit relatively narrow profiles and low intensity. This characteristic can lead to saturation at very high velocity dispersions, typical of the vicinity of massive galaxies hosting SMBHs (N23). However, this limitation is less critical for NSCs, which generally have significantly lower stellar velocity dispersions (σ_\star). While these lines may be saturated near SMBHs ($\sigma_\star \gtrsim 70 \text{ km s}^{-1}$) due to line broadening and blending with noise, they are expected to serve as effective indicators for measuring stellar kinematics around IMBHs, where velocity dispersions are lower. In the context of this simulated work focusing on IMBHs, we will specifically evaluate the feasibility of employing these lines in the J, K -short, and the blue part of the K -band IFS for measuring stellar kinematics, as detailed in subsection 6.3.

6.2.1. Creation of the input noiseless HSIM datacubes

To generate the input noiseless datacubes for HSIM, we adopted the MARCS synthetic stellar spectra (subsection 4.3) and assumed a Gaussian line-of-sight velocity distribution (LOSVD).

First, we used the `JAM_AXI_PROJ` routine from the `JAMPy` package (M. Cappellari 2008, 2020) to compute the projected intrinsic first (V) and second (V_{rms}) velocity moments. We assumed an oblate velocity ellipsoid (JAM keywords `gamma=0`, `kappa=1`) for predicting V . The velocity dispersion was then calculated as $\sigma_\star = \sqrt{V_{\text{rms}}^2 - V^2}$.

For each galaxy, we generated three kinematic models corresponding to different IMBH masses (M_{BH}), expressed as fractions of the NSC mass (M_{NSC}): 0%, 0.5%, and 1%. These fractions correspond to $M_{\text{BH}} = (0, 5 \times 10^3, 10^4) M_\odot$ for NGC 300 and $M_{\text{BH}} = (0, 3.5 \times 10^4, 7 \times 10^4) M_\odot$ for NGC 3115 dw01. The NSC masses, $M_{\text{NSC}} = 10^6 M_\odot$ for NGC 300 and $M_{\text{NSC}} = 7 \times 10^6 M_\odot$ for NGC 3115 dw01, were calculated using the MGE models representing the Core-Sérsic profile (Table 7) and the respective mass-to-light ratios: $M/L_I \approx 0.6 (M_\odot/L_\odot)$ for NGC 300 (N. Neumayer & C. J. Walcher 2012) and $M/L_{\text{F814W}} \approx 1.4 (M_\odot/L_\odot)$ for NGC 3115 dw01 (R. Pechetti et al. 2020). These values are consistent with the JAM model masses within 3%. The JAM_{cyl} kinematic maps were computed on a $5 \times 5 \text{ mas}^2$ grid, assuming isotropy ($\beta_z = 0$) and an inclination $i = 42^\circ$ (subsection 3.3).

Given the proximity of the HARMONI IMBH sample ($D \lesssim 10 \text{ Mpc}$), redshift effects are negligible. The input noiseless IFS datacube for HSIM was then created for each spaxel (x, y) using the following procedure:

1. The chosen synthetic stellar spectrum (subsection 4.3) was logarithmically rebinned to a velocity scale of $\text{velscale} = 0.5 \text{ km s}^{-1}$ per pixel.
2. For each spatial position (x, y) , a kinematic Gaussian kernel was constructed using the mean velocity $V(x, y)$ and velocity dispersion $\sigma_\star(x, y)$ predicted by the JAM_{cyl} model. The kernel was sampled with a velocity step $\Delta V = 0.5 \text{ km s}^{-1}$.
3. The logarithmically rebinned spectrum from step (i) was convolved with the Gaussian kernel from step (ii) in log-wavelength space. The resulting spectrum represents the broadened stellar light at position (x, y) .
4. The convolved spectrum was then resampled onto a linear wavelength grid. The wavelength step $\Delta\lambda$ was chosen to be at least two times smaller than the FWHM spectral resolution element of the highest-resolution HARMONI grating ($\Delta\lambda \approx 0.5 \text{ \AA}$ for the high-resolution gratings), ensuring proper sampling and conservation of spectral information during subsequent processing by HSIM.
5. Finally, the spectrum at (x, y) was scaled to match the surface brightness predicted by the MGE photometric model (Table 7) at that location. The scaling factor was determined by comparing the integrated flux of the unscaled spectrum within the relevant photometric band (e.g., F814W) to the MGE surface brightness, using the `ppxf.ppxf_util.mag_spectrum` function from pPXF (M. Cappellari 2023).

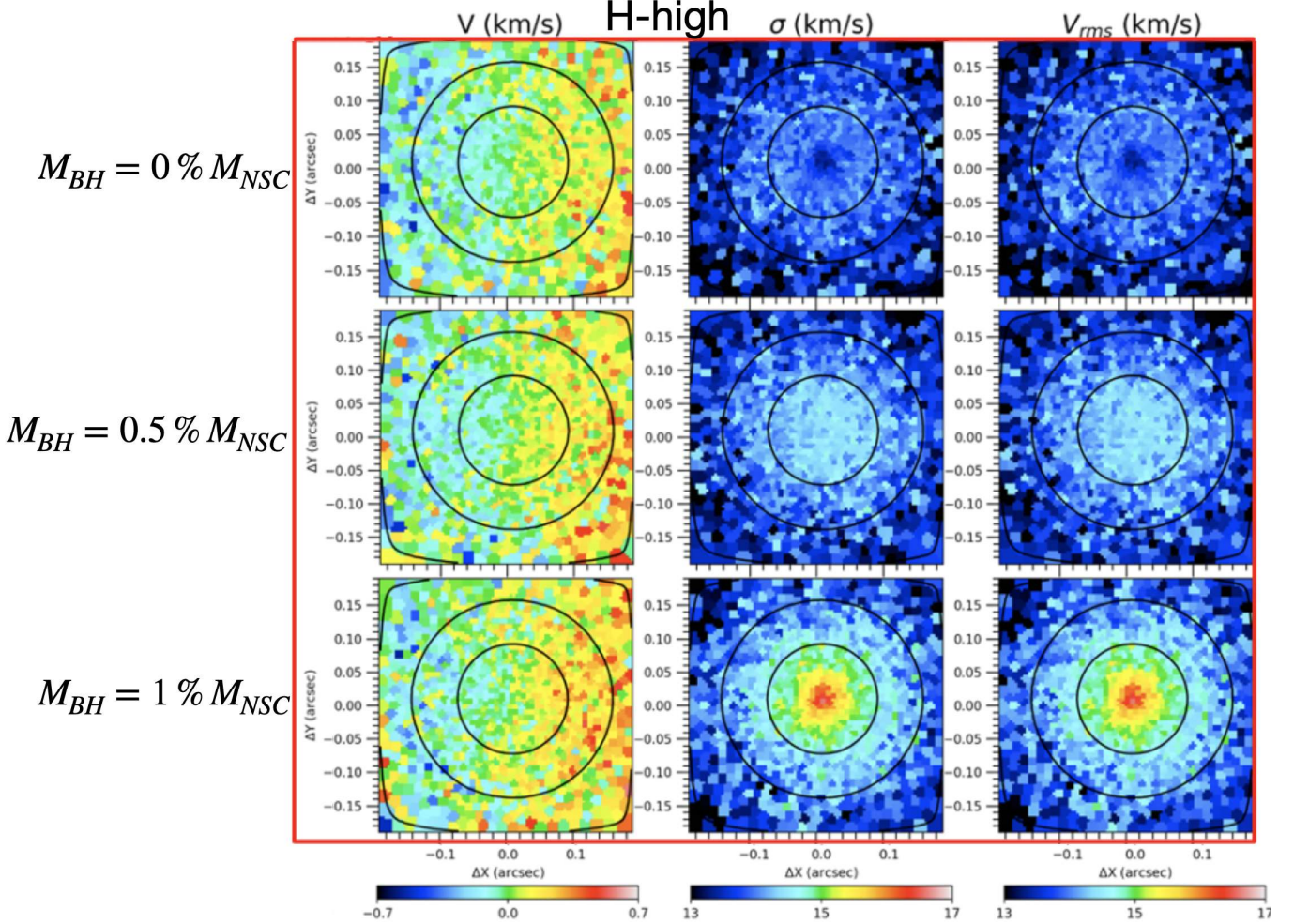


Figure 7. Stellar kinematic maps (V , σ_\star , and V_{rms}) for the nucleus of NGC 300, derived from mock HARMONI H -high IFS observations. The simulations were performed using HSIM (S. Zieleniewski et al. 2015), based on input kinematics generated with JAM_{cyl} models (M. Cappellari 2008) assuming three different central BH masses: $M_{\text{BH}} = 0 M_\odot$ (top row), $5 \times 10^3 M_\odot$ (middle row), and $10^4 M_\odot$ (bottom row). Kinematics were extracted from the simulated noisy data cubes using pPXF (M. Cappellari 2023), fitting the H -band spectral range $\lambda 1.45\text{--}1.74 \mu\text{m}$. Contours represent isophotes from the collapsed data cube, spaced by 1 mag arcsec $^{-2}$. The color bars are fixed across the rows to facilitate comparison and illustrate the kinematic impact of the central IMBH. The results demonstrate HARMONI’s capability to detect IMBH kinematic signatures in NSCs.

6.2.2. HSIM output datacubes (mock IFS HARMONI)

We used the input-noiseless cubes created in subsubsection 6.2.1 as an input for HSIM to produce the mock HARMONI IFS observations. For computational efficiency, we limited our IFS simulations within a central subset of the full HARMONI FoV measuring $0''.4 \times 0''.4$ region with a pixel size of 10×10 mas 2 . This choice ensured that the stellar kinematics, primarily influenced by the central BHs in our HARMONI IMBH sample, could be robustly detected. The exposure time for each simulation was carefully adjusted based on the gratings to ensure a median S/N of the final HARMONI spectral sampling produced in output by HSIM at least 5 per spectral pixel in each spaxel at the measured stellar features. Subsequently, pixel binning was employed to increase the S/N further. To replicate the actual ELT observa-

tions, we incorporated multi-exposure frames and dithering by setting a Detector Integration Time (DIT) of 900 s (15 minutes) for each exposure. The total exposure time was determined by the number of exposures (NDIT), which is an integer specified in the HSIM pipeline.

All essential properties of NGC 300 and NGC 3115 dw01 needed for the modelings are presented in subsection 3.3, while the chosen grating IFS and HSIM simulations are shown in Table 5. Regarding the AO performance during HSIM simulations, we applied the LTAO mode with an NGS of 17.5 mag in H -band within the radial distance of 30'', the optical (500 nm) zenith seeing of FWHM = 0''.64, and airmass of 1.3. These parameters are defaulted in HSIM to perform median observational conditions for the Armazones site.

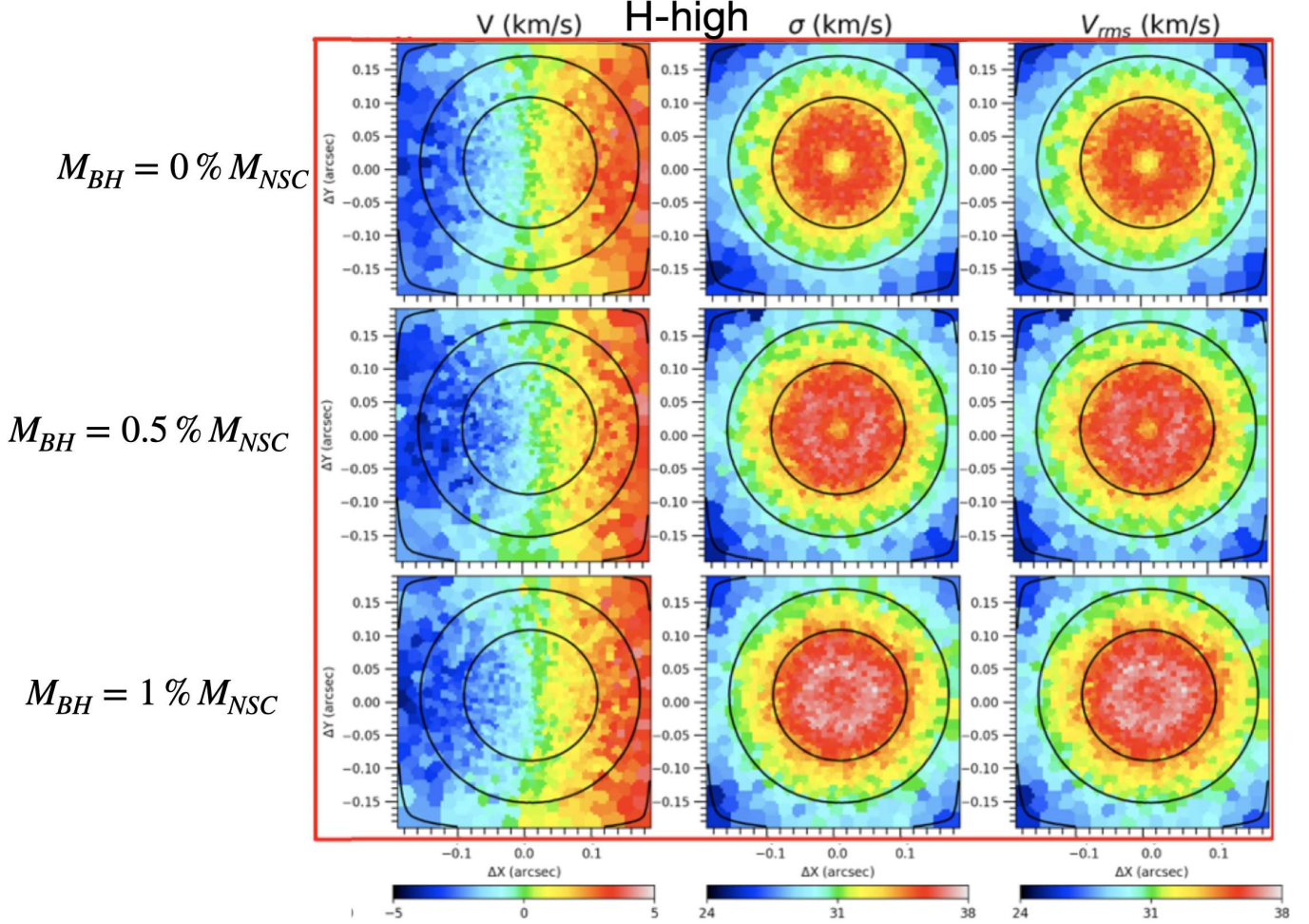


Figure 8. Same as Figure 7 but for NGC 3115 dw01 with three M_{BH} : = $0 M_{\odot}$ (first row), = $3.5 \times 10^4 M_{\odot}$ (second row), and = $7 \times 10^4 M_{\odot}$ (third row).

6.3. Stellar kinematics extraction from HSIM mock datacubes

To measure the stellar kinematics from the mock HARMONI data cubes generated in subsection 6.2, we utilized the spectral ranges defined by the HARMONI gratings themselves, as simulated by HSIM. Within these ranges, we focused on specific wavelength intervals known to contain prominent stellar absorption features suitable for kinematic analysis, as discussed in subsection 6.2 and illustrated in Figure 13. The key intervals used within each grating’s range were:

- Within the K (1.951–2.469 μm) and K -long (2.199–2.400 μm) bands: $\lambda 2.28$ – $2.40 \mu\text{m}$ (targeting CO band-heads).
- Within the H (1.435–1.815 μm) and H -high (1.538–1.678 μm) bands: $\lambda 1.45$ – $1.74 \mu\text{m}$ (targeting various atomic lines and CO features).
- Within the J -band (1.046–1.324 μm): $\lambda 1.16$ – $1.218 \mu\text{m}$ (targeting atomic lines, avoiding strong OH sky emission).

- Within the K -short band (2.017–2.201 μm): $\lambda 2.05$ – $2.20 \mu\text{m}$ (targeting atomic lines).

We verified the suitability of fitting only these restricted wavelength intervals by comparing the results with those obtained from fitting the full spectral range provided by each grating (excluding regions heavily contaminated by sky lines, particularly in the J -band). The differences in the extracted kinematics were minimal (<5%), confirming that these selected features robustly capture the kinematic information.

Before extracting kinematics, we applied the adaptive Voronoi Binning method (vorbin¹⁹; M. Cappellari & Y. Copin 2003) to the spatial dimensions of the data cubes. This process groups adjacent spaxels into larger bins to achieve a targeted-S/N greater than 20 per bin per \AA within the selected spectral fitting ranges, thereby reducing uncertainties in the subsequent kinematic measurements.

¹⁹ v3.1.5 available from <https://pypi.org/project/vorbin/>

Next, we extracted the stellar kinematics from the binned spectra using the penalized pixel-fitting method (pPXF²⁰; M. Cappellari 2023). For each bin:

1. The spectrum was logarithmically rebinned in wavelength.
2. A set of stellar templates, specifically the MARCS (B. Gustafsson et al. 2008) version of the C. Maraston & G. Strömbäck (2011) SPS models (using 13 templates with ages 3–15 Gyr and Solar metallicity, z002), was fitted to the spectrum.
3. The template continuum shape was corrected using Legendre polynomials (mdegree=0, degree=4).
4. The LOSVD was parameterized by its first two moments (mean velocity V and velocity dispersion σ_*) by setting moments=2.
5. The instrumental broadening of HARMONI (using the constant dispersion adopted by HSIM) was accounted for by convolving the templates during the fit.

Figure 13 shows examples of the best-fit SPS template overlaid on the simulated spectrum from the central bin for each of the six gratings, along with the fitting residuals (data-model).

The resulting kinematic maps (V , σ_* , and the root-mean-square velocity $V_{\text{rms}} = \sqrt{V^2 + \sigma_*^2}$) for the nuclei of NGC 300 and NGC 3115 dw01 are presented in Figure 7 and Figure 8 for the H -high grating, and in Figure 14 and Figure 15 for the other gratings. Since the rotation V is small in these models ($V \approx 0.7 \text{ km s}^{-1}$ for NGC 300 and $V \approx 5.0 \text{ km s}^{-1}$ for NGC 3115 dw01), the V_{rms} maps are very similar to the σ_* maps. The kinematic results are consistent across all six gratings for simulations with the same input M_{BH} , with differences in V_{rms} typically less than 3%, validating the extraction procedure.

As theoretically predicted (subsection 4.2 and S. Tremaine et al. 1994), the kinematic maps clearly show the signature of the central IMBH. Models without a BH ($M_{\text{BH}} = 0$) exhibit a characteristic drop in σ_* and V_{rms} towards the center. In contrast, models with sufficiently massive IMBHs show a distinct central peak in σ_* and V_{rms} within the BH’s SOI, with the peak becoming more pronounced as M_{BH} increases. This Keplerian-like rise in velocity dispersion is the key kinematic evidence for a central massive object.

In contrast, models that include a BH (i.e., $M_{\text{BH}} = 3.5 \times 10^4$ and $7 \times 10^4 M_{\odot}$) for NGC 3115 dw01 show a characteristic central drop in σ_* and V_{rms} , although not as pronounced as in the $M_{\text{BH}} = 0$ case. This may be due

to the combined effects of the galaxy’s distance, a massive NSC, and the small assumed M_{BH} . However, the clear difference between the kinematic maps with and without an IMBH, even for this most distant target NGC 3115 dw01 (at 9.7 Mpc), demonstrates HARMONI’s capability to resolve the kinematic signatures of IMBHs in nearby NSCs. HARMONI can effectively distinguish between a scenario with no IMBH and one containing an IMBH with a mass of just 0.5–1% of the NSC mass.

We note the presence of edge effects in the kinematic maps, particularly higher σ_* and V_{rms} values in the outermost bins. This is an artifact of the PSF convolution performed by HSIM near the boundary of the simulated field of view ($0.^{\prime\prime}4 \times 0.^{\prime\prime}4$), resulting in the squared appearance of the outermost surface brightness contour. To avoid biasing the dynamical modeling, these affected edge bins were excluded during the M_{BH} recovery process (subsection 7.1).

7. DISCUSSION

7.1. Recovering Black Hole Masses

Using the mock IFS data cubes from the six HARMONI gratings and their derived kinematic maps (subsection 6.3), we fitted these maps (V_{rms}) with JAM_{cyl} models. The goal was to determine the IMBH mass (M_{BH}) and constrain other dynamical parameters: stellar anisotropy (β_z), the stellar mass-to-light ratio relative to the *HST*/F814W photometry (M/L_{F814W}), and the galaxy inclination (i). We sampled M_{BH} logarithmically (assuming a flat prior in $\lg M_{\text{BH}}$), while the other three parameters were sampled linearly. The JAM_{cyl} models predict kinematics which are then compared to the mock V_{rms} maps, accounting for the HARMONI LTAO PSF ($\text{FWHM}_{\text{PSF}} \approx 12 \text{ mas}$, N23). We set the following search ranges for the parameters:

- $\log_{10}(M_{\text{BH}}/M_{\odot})$: 0 to 6
- M/L_{F814W} : 0.1 to 3 (M_{\odot}/L_{\odot})
- β_z : -1.0 to 0.99
- i : 5° to 90°

We started the fitting process with initial guesses for the parameters. For NGC 300, we used $(M/L_{\text{F814W}}, \beta_z, i) = (0.6, 0, 42)$, and for NGC 3115 dw01, $(M/L_{\text{F814W}}, \beta_z, i) = (1.4, 0, 42)$. The initial guesses for M_{BH} were set to the values used in the simulations (subsection 6.2): $M_{\text{BH}} = 0, 5 \times 10^3, 10^4 M_{\odot}$ for NGC 300 and $M_{\text{BH}} = 0, 3.5 \times 10^4, 7 \times 10^4 M_{\odot}$ for NGC 3115 dw01, depending on the specific simulation being fitted.

To find the best-fit JAM_{cyl} model and explore the parameter space thoroughly, we employed a Markov Chain Monte Carlo (MCMC) simulation using the adaptive Metropolis algorithm

²⁰ v8.2.1 available from <https://pypi.org/project/ppxf/>

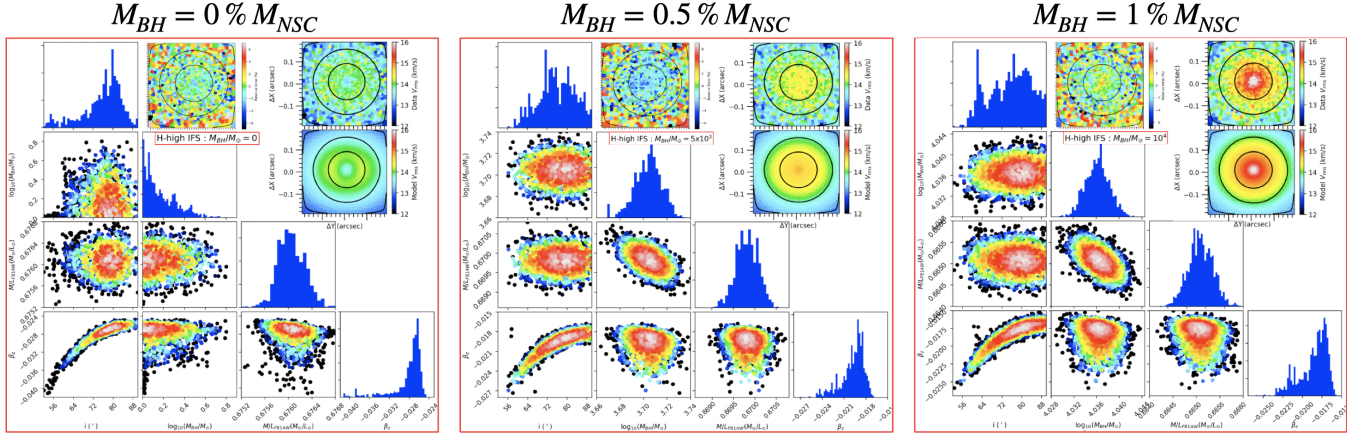


Figure 9. The posterior distributions obtained after the burn-in phase of the adamet MCMC optimization process for the JAM_{cyl} models applied to the *H*-high HSIM kinematics of NGC 300. These simulations were generated using the JAM_{cyl} models and feature three M_{BH} : 0 M_{\odot} (left), $5 \times 10^3 M_{\odot}$ (middle), and $10^4 M_{\odot}$ (right). Each red-square panel presents a set of four parameters (i , M_{BH} , M/L_{F814W} , and β_z), depicted as scatter plots illustrating their projected 2D distributions and histograms displaying their projected 1D distributions. In the top right corner, there are inset maps that depict the V_{rms} values. The top maps represent the simulated kinematic maps extracted from the simulated datacubes, while the bottom maps represent the kinematic maps recovered from the best-fit JAM_{cyl} model. These maps visually illustrate the level of agreement or disagreement at each spaxel between the simulated data and our best-fit model. The determination of the best-fit JAM_{cyl} model is based on the PDF with the highest likelihood.

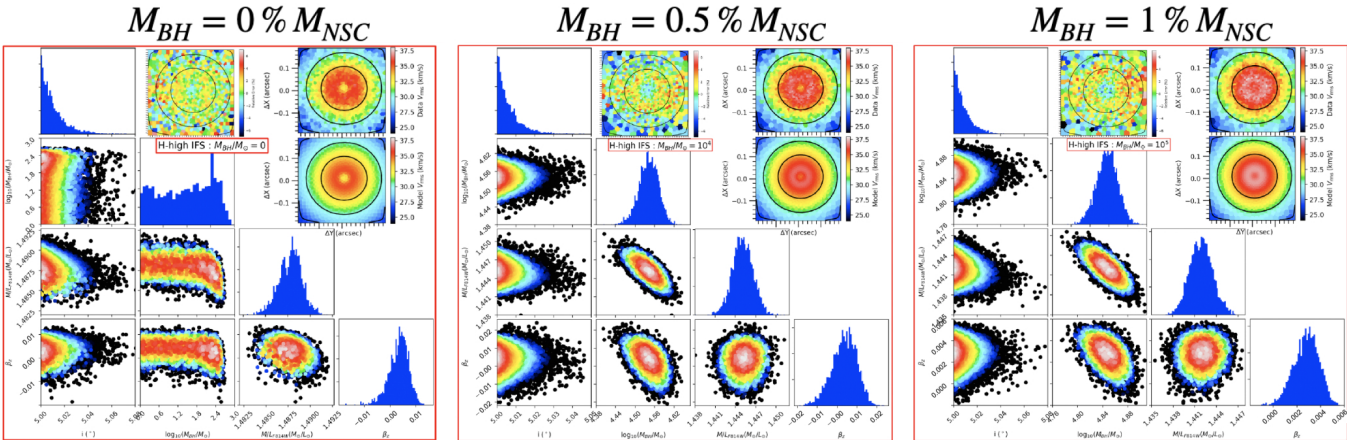


Figure 10. Same as Figure 9 but for the *H*-high HSIM kinematics of NGC 3115 dw01 with three M_{BH} : 0 M_{\odot} (left), $3.5 \times 10^4 M_{\odot}$ (middle), $7 \times 10^4 M_{\odot}$ (right).

(H. Haario et al. 2001) within the Bayesian framework provided by the adamet²¹ package (M. Cappellari et al. 2013b). Each MCMC chain ran for 3×10^4 iterations. We discarded the first 20% as the burn-in phase and constructed the full probability distribution function (PDF) from the remaining 80%. The best-fit parameters correspond to the point of highest likelihood in the PDF. We determined the 1σ (16–84 percentile range) and 3σ (0.14–99.86 percentile range) confidence levels from the posterior PDF.

The best-fit parameters and their uncertainties for NGC 300 are shown in Figure 9, Figure 16, and Figure 17, and for

NGC 3115 dw01 in Figure 10, Figure 18, and Figure 19. These figures display the 2D posterior distributions for pairs of parameters, where color indicates likelihood (white is highest, black is below 3σ). Histograms show the 1D marginalized distributions. The best-fit values and uncertainties derived from these distributions are listed in Table 8 (NGC 300) and Table 9 (NGC 3115 dw01).

Inset plots in the top-right corner of each panel in these figures compare the input mock V_{rms} map (top) with the best-fit JAM_{cyl} model prediction (bottom). Relative error maps, $(\text{data}-\text{model})/\text{data}$, are also shown (middle) to visualize the goodness of fit bin-by-bin. Overall, the models agree well with the mock kinematics within the central $0''.4 \times 0''.4$ region for all gratings.

²¹ v2.0.9 available from <https://pypi.org/project/adamet/>

The recovered M_{BH} and M/L_{F814W} values are consistent with the input values used in the simulations, typically within 5%. This success is due to the high quality of the simulated kinematics and the fact that the IMBH SOI is well-resolved by HARMONI's 10 mas spaxels, even for the smallest simulated BH masses ($M_{\text{BH}} = 5 \times 10^3 M_{\odot}$ for NGC 300 and $M_{\text{BH}} = 3.5 \times 10^4 M_{\odot}$ for NGC 3115 dw01). The corresponding SOI radii are $R_{\text{SOI}} = 13$ mas for NGC 300 ($D = 2.2$ Mpc, $\sigma_{\star} = 13.3 \text{ km s}^{-1}$) and $R_{\text{SOI}} = 35$ mas for NGC 3115 dw01 ($D = 9.7$ Mpc, $\sigma_{\star} = 32 \text{ km s}^{-1}$).

The 2D posterior distributions show consistent features across different M_{BH} values and gratings. As expected, when $M_{\text{BH}} > 0$, there is a negative covariance between M_{BH} and M/L_{F814W} , creating the characteristic “banana shape” in the confidence contours. This degeneracy arises because a larger BH mass can be partially compensated by a smaller stellar M/L , and vice versa, while still fitting the mock kinematics.

The high spatial resolution of the simulations allows us to break this degeneracy effectively. For the simulations without a BH ($M_{\text{BH}} = 0$), the fits yield upper limits of $M_{\text{BH}} \approx 10^2 M_{\odot}$ for NGC 300 and $M_{\text{BH}} \approx 10^3 M_{\odot}$ for NGC 3115 dw01. This indicates HARMONI's ability to distinguish between the presence and absence of IMBHs above these mass thresholds at the respective distances (though see subsection 7.2 for caveats regarding mass segregation).

The anisotropy parameter β_z is well-constrained around the input value of $\beta_z = 0$ (isotropy), with best fits slightly favoring tangential orbits ($\beta_z \lesssim 0$) for NGC 300 and radial orbits ($\beta_z \gtrsim 0$) for NGC 3115 dw01, consistent with isotropy within errors. The inclination i , however, is less well-constrained. For NGC 300, it spans a wide range (40° to 90°), while for NGC 3115 dw01, it is mostly constrained to low values ($\gtrsim 5^\circ$), except for the J -band fit. This poor constraint on inclination is expected because the models are nearly spherical and show little rotation; spherical systems look identical regardless of viewing angle.

Figure 11 summarizes the comparison between the input M_{BH} values and the recovered values from the JAM_{cyl} modeling across all six gratings. The plot shows the median recovered mass for each input mass, with error bars indicating the 3σ confidence range. The results demonstrate excellent recovery, consistent with the input values within the uncertainties.

7.2. Caveat: Distinguishing IMBHs from Mass Segregation

A potential complication in dynamically detecting IMBHs is the effect of mass segregation. Stellar-mass black holes (sBHs), being more massive than typical stars, can sink towards the center of a dense stellar system like an NSC over time. This process increases the central mass density and, consequently, the central velocity dispersion, potentially mimicking the kinematic signature of a single, more massive

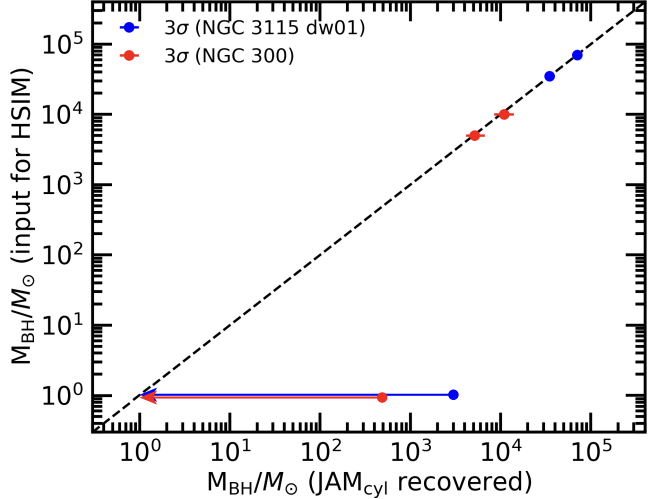


Figure 11. Comparison between the input IMBH masses used for the HARMONI simulations and the recovered masses from the JAM_{cyl} fits. The points show the median recovered M_{BH} across all six gratings for each input mass. Error bars represent the 3σ confidence interval (0.14th to 99.86th percentiles from the MCMC chains, see Table 8 and Table 9). The dashed line indicates perfect recovery ($M_{\text{BH, recovered}} = M_{\text{BH, input}}$). **In this log-log scale plot, the (0, 0) coordinates are replaced by (10⁰, 10⁰).**

IMBH (J. N. Bahcall & R. A. Wolf 1977; P. Bianchini et al. 2017).

Theoretical studies suggest that IMBHs down to $M_{\text{BH}} \approx 3 \times 10^3 M_{\odot}$ might be dynamically detectable in dense stellar systems like Galactic globular clusters, even considering mass segregation (J. E. Greene et al. 2020, section 3.2). Our simulations explore IMBHs with masses of 0.5% of their host NSC's mass. For NGC 300 ($M_{\text{NSC}} \approx 10^6 M_{\odot}$) and NGC 3115 dw01 ($M_{\text{NSC}} \approx 7 \times 10^6 M_{\odot}$), this corresponds to $M_{\text{BH}} \approx 5 \times 10^3 M_{\odot}$ and $M_{\text{BH}} \approx 3.5 \times 10^4 M_{\odot}$, respectively. Since these masses exceed the $\approx 3 \times 10^3 M_{\odot}$ threshold, detecting them with HARMONI appears feasible based solely on mass.

However, the central concentration of sBHs due to mass segregation can elevate the central M/L , potentially leading to a false IMBH detection (e.g., M. den Brok et al. 2014). To assess the importance of this effect, we can estimate the system's relaxation timescale, $t_{\text{relax}}(r)$, which characterizes the time needed for stellar orbits to change significantly due to two-body interactions. Following J. N. Bahcall & R. A. Wolf (1977) and M. Valluri et al. (2005), we use:

$$t_{\text{relax}}(r) \approx (1.4 \times 10^8 \text{ yr}) \sigma_{20}^3(r) \rho_5^{-1}(r) (\ln \Lambda_{10})^{-1}. \quad (3)$$

Here, $\sigma_{20} = \sigma_{\star}/(20 \text{ km s}^{-1})$ is the stellar velocity dispersion normalized to 20 km s⁻¹, $\rho_5 = \rho/(10^5 M_{\odot} \text{ pc}^{-3})$ is the intrinsic stellar mass density normalized to $10^5 M_{\odot} \text{ pc}^{-3}$, and $\ln \Lambda_{10} = \ln(\Lambda)/10$ is the Coulomb logarithm, typically assumed to be ≈ 10 . If t_{relax} at a given radius is comparable to

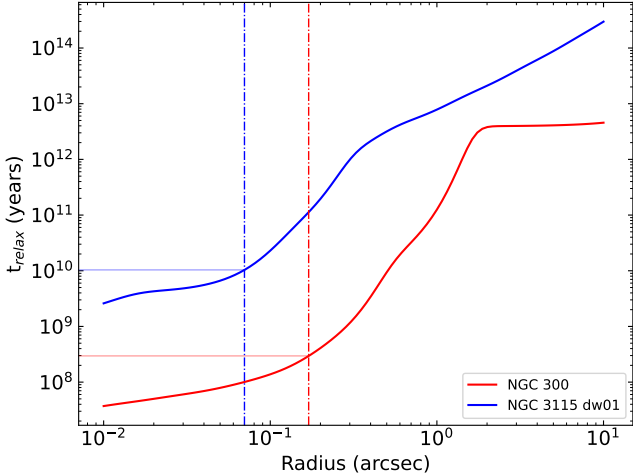


Figure 12. Relaxation time $t_{\text{relax}}(r)$ as a function of radius for the NSC models of NGC 300 (red solid line) and NGC 3115 dw01 (blue solid line), assuming no central IMBH. The vertical dash-dotted lines indicate the effective radii (R_e) of the respective NSCs.

or longer than the age of the Universe (~ 13.8 Gyr), significant mass segregation of sBHs towards the center is unlikely to have occurred. In such cases, an observed central rise in velocity dispersion is more likely a genuine signature of an IMBH.

We calculated $t_{\text{relax}}(r)$ for the NSCs of NGC 300 and NGC 3115 dw01 using their observed central velocity dispersions ($\sigma_\star = 13.3 \text{ km s}^{-1}$ for NGC 300 (N. Kacharov et al. 2018); $\sigma_\star = 32 \text{ km s}^{-1}$ for NGC 3115 dw01 (R. C. Peterson & N. Caldwell 1993)) and intrinsic mass densities derived from the deprojected MGE models of the NSC components (Table 7, bold entries) assuming spherical symmetry and the literature M/L values (subsection 5.2). The results are shown in Figure 12. At the effective radius of the NSC (R_e), we find $t_{\text{relax}}(R_e \approx 1.9 \text{ pc}) \approx 3 \text{ Myr}$ for NGC 300, but $t_{\text{relax}}(R_e \approx 3.2 \text{ pc}) \approx 10 \text{ Gyr}$ for NGC 3115 dw01.

The very short relaxation time for NGC 300’s NSC suggests that mass segregation could be significant, potentially complicating the interpretation of its central kinematics. Conversely, the long relaxation time for NGC 3115 dw01’s NSC implies that mass segregation is likely unimportant, making it a cleaner target for IMBH detection. However, significant uncertainties remain regarding the efficiency of sBH segregation and retention in NSCs, requiring more detailed simulations (D. D. Nguyen et al. 2018).

While alternative methods like gravitational microlensing have been proposed to detect populations of sBHs (D. P. Bennett et al. 2002), they are observationally challenging for extragalactic systems and beyond the scope of this paper. It is worth noting that while IMBH formation in globular clusters faces theoretical challenges and lacks strong observational support (R. P. van der Marel & J. Anderson 2010; A. Zocchi

et al. 2017, 2019; H. Baumgardt et al. 2019), NSCs often possess higher velocity dispersions and longer relaxation times, making them more plausible environments for hosting IMBHs (see review by N. Neumayer et al. 2020, section 10.1).

7.3. Sensitivity Limits

To determine the minimum exposure time required for reliable kinematic measurements, we performed additional simulations for both NGC 300 and NGC 3115 dw01. In these tests, we progressively reduced the simulated exposure time, which correspondingly lowered the S/N in the mock data cubes. We continued this process until the stellar kinematics could only marginally be extracted after applying Voronoi binning (Vorbin) to achieve a target S/N of ≈ 20 per bin.

The minimum required exposure times determined through this process are listed in Column 4 of Table 5. These times are relatively short (less than three hours per grating), suggesting that such observations are feasible with the ELT.

However, it is important to note that these sensitivity limits are based on simulations using photometric models derived from current *HST* data. Future, higher-resolution imaging (e.g., from *JWST*/NIRCam or ELT/MICADO) might resolve the NSCs more finely, potentially revealing lower central surface brightness than assumed in our current models. If the actual surface brightness is lower, the S/N achieved in a given exposure time will be reduced, and longer exposure times than estimated here might be necessary for real observations. Despite this caveat, our simulations demonstrate the fundamental feasibility of detecting IMBH kinematic signatures with HARMONI within reasonable exposure times.

8. CONCLUSIONS

We investigated the capability of the ELT/HARMONI instrument to detect and measure the masses of IMBHs residing in the NSCs of nearby dwarf galaxies ($D \lesssim 10 \text{ Mpc}$). This mass range represents a critical link between sBHs and SMBHs. We defined the “HARMONI IMBH survey,” a sample of 44 galaxies selected based on criteria ensuring observability and suitability for IMBH searches, notably the presence of luminous NSCs and low central velocity dispersions ($\sigma_{\star,c} < 70 \text{ km s}^{-1}$).

To assess HARMONI’s performance, we conducted realistic simulations for two representative galaxies (NGC 300 and NGC 3115 dw01). We combined photometric models derived from *HST* data with JAM to predict intrinsic stellar kinematics for scenarios including IMBHs with masses ranging from 0% to 1% of the NSC mass. These predictions served as input for the HSIM simulator to generate mock HARMONI IFS data cubes across six different gratings. We subsequently analyzed these mock observations using standard techniques: extracting kinematics with pPXF and recovering the IMBH mass and other dynamical parameters using JAM within a Bayesian MCMC framework.

Our key findings are:

- HARMONI's high angular resolution (simulated at 10 mas) can resolve the kinematic SOI of IMBHs with masses down to $\approx 0.5\%$ of their host NSC mass, clearly distinguishing them from models without a central BH.
- The recovered M_{BH} and stellar M/L_{F814W} accurately matched the input simulation values within $\lesssim 5\%$ uncertainty, demonstrating the robustness of the measurement technique with HARMONI data.
- Consistent kinematic results and successful parameter recovery were achieved across different HARMONI gratings, including both medium ($\lambda/\Delta\lambda \approx 7100$) and high ($\lambda/\Delta\lambda \approx 17400$) spectral resolutions.
- The simulations indicate that high-quality IFS data, sufficient for these demanding measurements, can be obtained within feasible exposure times (typically less than four hours per target under median conditions).

These results confirm that HARMONI will be a powerful instrument for constraining the elusive IMBH population in nearby galaxies. Such observations will provide crucial tests for BH seeding models, refine our understanding of galaxy–BH scaling relations at the lowest mass scales, and inform predictions for future gravitational wave observatories.

ACKNOWLEDGEMENTS

The authors would like to thank the anonymous referee for their careful reading and useful comments, that helped to improve the paper greatly. Research conducted by HNN is funded by University of Science, VNU-HCM under grant number T2013-105. TQL's and TNL's works are partially supported by a grant from the Simons Foundation to IFIRSE, ICISE (916424, N.H.). NT would like to acknowledge partial support from UKRI grant ST/X002322/1 for UK ELT Instrument Development at Oxford. MPS acknowledges support under grants RYC2021-033094-I, CNS2023-145506 and PID2023-146667NB-I00 funded by MCIN/AEI/10.13039/501100011033 and the European Union NextGenerationEU/PRTR.

Facilities: *HST*, 2MASS, SDSS DR12, Gaia, DSS.

Software: python 3.12, Matplotlib 3.6.0, numpy 1.22, scipy 1.3.1, photutils 0.7, MPFIT, plotbin 3.1.3, astropy 5.1 (Astropy Collaboration et al. 2022), adamet 2.0.9 (M. Cappellari et al. 2013b), jampy 7.2.0 (M. Cappellari 2020), pPXF 8.2.1 (M. Cappellari 2023), vorbin 3.1.5 (M. Cappellari & Y. Copin 2003), MgeFit 5.0.14 (M. Cappellari 2002) and HSIM 3.11 (S. Zielezniewski et al. 2015).

REFERENCES

- An, J. H., & Evans, N. W. 2006, ApJ, 642, 752, doi: [10.1086/501040](https://doi.org/10.1086/501040)
- Ashok, A., Seth, A., Erwin, P., et al. 2023, ApJ, 958, 100, doi: [10.3847/1538-4357/ace341](https://doi.org/10.3847/1538-4357/ace341)
- Astropy Collaboration, Price-Whelan, A. M., Lim, P. L., et al. 2022, ApJ, 935, 167, doi: [10.3847/1538-4357/ac7c74](https://doi.org/10.3847/1538-4357/ac7c74)
- Avila, R. J., Hack, W. J., & STScI AstroDrizzle Team. 2012, in American Astronomical Society Meeting Abstracts, Vol. 220, American Astronomical Society Meeting Abstracts #220, 135.13
- Bahcall, J. N., & Wolf, R. A. 1977, ApJ, 216, 883, doi: [10.1086/155534](https://doi.org/10.1086/155534)
- Bailes, M., Berger, B. K., Brady, P. R., et al. 2021, Nature Reviews Physics, 3, 344, doi: [10.1038/s42254-021-00303-8](https://doi.org/10.1038/s42254-021-00303-8)
- Baldassare, V. F., Stone, N. C., Foord, A., Gallo, E., & Ostriker, J. P. 2022, ApJ, 929, 84, doi: [10.3847/1538-4357/ac5f51](https://doi.org/10.3847/1538-4357/ac5f51)
- Barth, A. J., Ho, L. C., & Sargent, W. L. W. 2002, AJ, 124, 2607, doi: [10.1086/343840](https://doi.org/10.1086/343840)
- Barth, A. J., Sarzi, M., Rix, H.-W., et al. 2001, ApJ, 555, 685, doi: [10.1086/321523](https://doi.org/10.1086/321523)
- Barth, A. J., Strigari, L. E., Bentz, M. C., Greene, J. E., & Ho, L. C. 2009, ApJ, 690, 1031, doi: [10.1088/0004-637X/690/1/1031](https://doi.org/10.1088/0004-637X/690/1/1031)
- Baumgardt, H., He, C., Sweet, S. M., et al. 2019, MNRAS, 488, 5340, doi: [10.1093/mnras/stz2060](https://doi.org/10.1093/mnras/stz2060)
- Bennett, D. P., Becker, A. C., Quinn, J. L., et al. 2002, ApJ, 579, 639, doi: [10.1086/342225](https://doi.org/10.1086/342225)
- Bianchini, P., Sills, A., van de Ven, G., & Sippel, A. C. 2017, MNRAS, 469, 4359, doi: [10.1093/mnras/stx1114](https://doi.org/10.1093/mnras/stx1114)
- Binney, J. 1980, MNRAS, 190, 873, doi: [10.1093/mnras/190.4.873](https://doi.org/10.1093/mnras/190.4.873)
- Böker, T., Laine, S., van der Marel, R. P., et al. 2002, AJ, 123, 1389, doi: [10.1086/339025](https://doi.org/10.1086/339025)
- Bono, G., Caputo, F., Marconi, M., & Musella, I. 2010, ApJ, 715, 277, doi: [10.1088/0004-637X/715/1/277](https://doi.org/10.1088/0004-637X/715/1/277)
- Bonoli, S., Mayer, L., & Callegari, S. 2014, MNRAS, 437, 1576, doi: [10.1093/mnras/stt1990](https://doi.org/10.1093/mnras/stt1990)
- Busso, G., Cacciari, C., Bellazzini, M., et al. 2022, Gaia DR3 documentation, European Space Agency; Gaia Data Processing and Analysis Consortium. id. 5 doi: <https://doi.org/10.5281/zenodo.5900000>
- Cappellari, M. 2002, MNRAS, 333, 400, doi: [10.1046/j.1365-8711.2002.05412.x](https://doi.org/10.1046/j.1365-8711.2002.05412.x)
- Cappellari, M. 2008, MNRAS, 390, 71, doi: [10.1111/j.1365-2966.2008.13754.x](https://doi.org/10.1111/j.1365-2966.2008.13754.x)

- Cappellari, M. 2016, *ARA&A*, 54, 597, doi: [10.1146/annurev-astro-082214-122432](https://doi.org/10.1146/annurev-astro-082214-122432)
- Cappellari, M. 2020, *MNRAS*, 494, 4819, doi: [10.1093/mnras/staa959](https://doi.org/10.1093/mnras/staa959)
- Cappellari, M. 2023, *MNRAS*, 526, 3273, doi: [10.1093/mnras/stad2597](https://doi.org/10.1093/mnras/stad2597)
- Cappellari, M. 2025, arXiv e-prints, arXiv:2503.02746, doi: [10.48550/arXiv.2503.02746](https://doi.org/10.48550/arXiv.2503.02746)
- Cappellari, M., & Copin, Y. 2003, *MNRAS*, 342, 345, doi: [10.1046/j.1365-8711.2003.06541.x](https://doi.org/10.1046/j.1365-8711.2003.06541.x)
- Cappellari, M., Bacon, R., Bureau, M., et al. 2006, *MNRAS*, 366, 1126, doi: [10.1111/j.1365-2966.2005.09981.x](https://doi.org/10.1111/j.1365-2966.2005.09981.x)
- Cappellari, M., Emsellem, E., Krajnović, D., et al. 2011, *MNRAS*, 413, 813, doi: [10.1111/j.1365-2966.2010.18174.x](https://doi.org/10.1111/j.1365-2966.2010.18174.x)
- Cappellari, M., McDermid, R. M., Alatalo, K., et al. 2013a, *MNRAS*, 432, 1862, doi: [10.1093/mnras/stt644](https://doi.org/10.1093/mnras/stt644)
- Cappellari, M., Scott, N., Alatalo, K., et al. 2013b, *MNRAS*, 432, 1709, doi: [10.1093/mnras/stt562](https://doi.org/10.1093/mnras/stt562)
- Cardelli, J. A., Clayton, G. C., & Mathis, J. S. 1989, *ApJ*, 345, 245, doi: [10.1086/167900](https://doi.org/10.1086/167900)
- Carlsten, S. G., Greene, J. E., Beaton, R. L., & Greco, J. P. 2022, *ApJ*, 927, 44, doi: [10.3847/1538-4357/ac457e](https://doi.org/10.3847/1538-4357/ac457e)
- Carson, D. J., Barth, A. J., Seth, A. C., et al. 2015, *AJ*, 149, 170, doi: [10.1088/0004-6256/149/5/170](https://doi.org/10.1088/0004-6256/149/5/170)
- Conroy, C., Villaume, A., van Dokkum, P. G., & Lind, K. 2018, *ApJ*, 854, 139, doi: [10.3847/1538-4357/aaab49](https://doi.org/10.3847/1538-4357/aaab49)
- Côté, P., Piatek, S., Ferrarese, L., et al. 2006, *ApJS*, 165, 57, doi: [10.1086/504042](https://doi.org/10.1086/504042)
- Crespo Gómez, A., Piqueras López, J., Arribas, S., et al. 2021, *A&A*, 650, A149, doi: [10.1051/0004-6361/202039472](https://doi.org/10.1051/0004-6361/202039472)
- Davis, T. A., Bureau, M., Cappellari, M., Sarzi, M., & Blitz, L. 2013, *Nature*, 494, 328, doi: [10.1038/nature11819](https://doi.org/10.1038/nature11819)
- de Swardt, B., Kraan-Korteweg, R. C., & Jerjen, H. 2010, *MNRAS*, 407, 955, doi: [10.1111/j.1365-2966.2010.16986.x](https://doi.org/10.1111/j.1365-2966.2010.16986.x)
- de Zeeuw, T. 2001, in *Black Holes in Binaries and Galactic Nuclei*, ed. L. Kaper, E. P. J. V. D. Heuvel, & P. A. Woudt, 78, doi: [10.1007/10720995_12](https://doi.org/10.1007/10720995_12)
- Dehnen, W. 1993, *MNRAS*, 265, 250, doi: [10.1093/mnras/265.1.250](https://doi.org/10.1093/mnras/265.1.250)
- den Brok, M., van de Ven, G., van den Bosch, R., & Watkins, L. 2014, *MNRAS*, 438, 487, doi: [10.1093/mnras/stt2221](https://doi.org/10.1093/mnras/stt2221)
- Di Matteo, T., Colberg, J., Springel, V., Hernquist, L., & Sijacki, D. 2008, *ApJ*, 676, 33, doi: [10.1086/524921](https://doi.org/10.1086/524921)
- Emsellem, E., Monnet, G., & Bacon, R. 1994, *A&A*, 285, 723
- Erwin, P., & Gadotti, D. A. 2012, *Advances in Astronomy*, 2012, 946368, doi: [10.1155/2012/946368](https://doi.org/10.1155/2012/946368)
- Evans, C. J., Davies, B., Kudritzki, R. P., et al. 2011, *A&A*, 527, A50, doi: [10.1051/0004-6361/201015986](https://doi.org/10.1051/0004-6361/201015986)
- Fabian, A. C. 2012, *ARA&A*, 50, 455, doi: [10.1146/annurev-astro-081811-125521](https://doi.org/10.1146/annurev-astro-081811-125521)
- Fahrion, K., Lyubenova, M., Hilker, M., et al. 2020, *A&A*, 637, A27, doi: [10.1051/0004-6361/202037686](https://doi.org/10.1051/0004-6361/202037686)
- Fahrion, K., Bulichi, T.-E., Hilker, M., et al. 2022, *A&A*, 667, A101, doi: [10.1051/0004-6361/202244932](https://doi.org/10.1051/0004-6361/202244932)
- Ferrarese, L., & Merritt, D. 2000, *ApJL*, 539, L9, doi: [10.1086/312838](https://doi.org/10.1086/312838)
- Gallo, E., Treu, T., Jacob, J., et al. 2008, *ApJ*, 680, 154, doi: [10.1086/588012](https://doi.org/10.1086/588012)
- Gebhardt, K., Rich, R. M., & Ho, L. C. 2005, *ApJ*, 634, 1093, doi: [10.1086/497023](https://doi.org/10.1086/497023)
- Gebhardt, K., Bender, R., Bower, G., et al. 2000, *ApJL*, 539, L13, doi: [10.1086/312840](https://doi.org/10.1086/312840)
- Gebhardt, K., Lauer, T. R., Kormendy, J., et al. 2001, *AJ*, 122, 2469, doi: [10.1086/323481](https://doi.org/10.1086/323481)
- Gebhardt, K., Richstone, D., Tremaine, S., et al. 2003, *ApJ*, 583, 92, doi: [10.1086/345081](https://doi.org/10.1086/345081)
- Georgiev, I. Y., & Böker, T. 2014, *MNRAS*, 441, 3570, doi: [10.1093/mnras/stu797](https://doi.org/10.1093/mnras/stu797)
- Georgiev, I. Y., Böker, T., Leigh, N., Lützgendorf, N., & Neumayer, N. 2016, *MNRAS*, 457, 2122, doi: [10.1093/mnras/stw093](https://doi.org/10.1093/mnras/stw093)
- González-Alfonso, E., García-Bernete, I., Pereira-Santaella, M., et al. 2023, arXiv e-prints, arXiv:2312.04914, doi: [10.48550/arXiv.2312.04914](https://doi.org/10.48550/arXiv.2312.04914)
- Graham, A. W., Erwin, P., Trujillo, I., & Asensio Ramos, A. 2003, *AJ*, 125, 2951, doi: [10.1086/375320](https://doi.org/10.1086/375320)
- Graham, M. J., Ford, K. E. S., McKernan, B., et al. 2020, *PhRvL*, 124, 251102, doi: [10.1103/PhysRevLett.124.251102](https://doi.org/10.1103/PhysRevLett.124.251102)
- Greene, J. E. 2012, *Nature Communications*, 3, 1304, doi: [10.1038/ncomms2314](https://doi.org/10.1038/ncomms2314)
- Greene, J. E., Strader, J., & Ho, L. C. 2020, *ARA&A*, 58, 257, doi: [10.1146/annurev-astro-032620-021835](https://doi.org/10.1146/annurev-astro-032620-021835)
- Gültekin, K., Richstone, D. O., Gebhardt, K., et al. 2009, *ApJ*, 698, 198, doi: [10.1088/0004-637X/698/1/198](https://doi.org/10.1088/0004-637X/698/1/198)
- Gustafsson, B., Edvardsson, B., Eriksson, K., et al. 2008, *A&A*, 486, 951, doi: [10.1051/0004-6361:200809724](https://doi.org/10.1051/0004-6361:200809724)
- Haario, H., Saksman, E., & Tamminen, J. 2001, *Bernoulli*, 7, 223
- Häggele, G. F., Díaz, Á. I., Cardaci, M. V., Terlevich, E., & Terlevich, R. 2007, *MNRAS*, 378, 163, doi: [10.1111/j.1365-2966.2007.11751.x](https://doi.org/10.1111/j.1365-2966.2007.11751.x)
- Hartmann, M., Debattista, V. P., Seth, A., Cappellari, M., & Quinn, T. R. 2011, *MNRAS*, 418, 2697, doi: [10.1111/j.1365-2966.2011.19659.x](https://doi.org/10.1111/j.1365-2966.2011.19659.x)
- Ho, L. C., Greene, J. E., Filippenko, A. V., & Sargent, W. L. W. 2009, *ApJS*, 183, 1, doi: [10.1088/0067-0049/183/1/1](https://doi.org/10.1088/0067-0049/183/1/1)
- Hoyer, N., Neumayer, N., Seth, A. C., Georgiev, I. Y., & Greene, J. E. 2023, *MNRAS*, 520, 4664, doi: [10.1093/mnras/stad220](https://doi.org/10.1093/mnras/stad220)
- Huchra, J. P., Macri, L. M., Masters, K. L., et al. 2012, *ApJS*, 199, 26, doi: [10.1088/0067-0049/199/2/26](https://doi.org/10.1088/0067-0049/199/2/26)
- Inayoshi, K., Visbal, E., & Haiman, Z. 2020, *ARA&A*, 58, 27, doi: [10.1146/annurev-astro-120419-014455](https://doi.org/10.1146/annurev-astro-120419-014455)

- Jarrett, T. H., Chester, T., Cutri, R., Schneider, S. E., & Huchra, J. P. 2003, AJ, 125, 525, doi: [10.1086/345794](https://doi.org/10.1086/345794)
- Jedrzejewski, R. I. 1987, MNRAS, 226, 747, doi: [10.1093/mnras/226.4.747](https://doi.org/10.1093/mnras/226.4.747)
- Jerjen, H., Binggeli, B., & Freeman, K. C. 2000a, AJ, 119, 593, doi: [10.1086/301216](https://doi.org/10.1086/301216)
- Jerjen, H., Freeman, K. C., & Binggeli, B. 2000b, AJ, 119, 166, doi: [10.1086/301188](https://doi.org/10.1086/301188)
- Kacharov, N., Neumayer, N., Seth, A. C., et al. 2018, MNRAS, 480, 1973, doi: [10.1093/mnras/sty1985](https://doi.org/10.1093/mnras/sty1985)
- Karachentsev, I. D., Karachentseva, V. E., Huchtmeier, W. K., & Makarov, D. I. 2004, AJ, 127, 2031, doi: [10.1086/382905](https://doi.org/10.1086/382905)
- Karachentsev, I. D., Makarov, D. I., & Kaisina, E. I. 2013, AJ, 145, 101, doi: [10.1088/0004-6256/145/4/101](https://doi.org/10.1088/0004-6256/145/4/101)
- Kim, S. C., Sung, H., Park, H. S., & Sung, E.-C. 2004, ChJAA, 4, 299, doi: [10.1088/1009-9271/4/4/299](https://doi.org/10.1088/1009-9271/4/4/299)
- Kochanek, C. S. 2016, MNRAS, 461, 371, doi: [10.1093/mnras/stw1290](https://doi.org/10.1093/mnras/stw1290)
- Kormendy, J., & Ho, L. C. 2013, ARA&A, 51, 511, doi: [10.1146/annurev-astro-082708-101811](https://doi.org/10.1146/annurev-astro-082708-101811)
- Kormendy, J., & Richstone, D. 1995, ARA&A, 33, 581, doi: [10.1146/annurev.aa.33.090195.003053](https://doi.org/10.1146/annurev.aa.33.090195.003053)
- Krajnović, D., Cappellari, M., & McDermid, R. M. 2018, MNRAS, 473, 5237, doi: [10.1093/mnras/stx2704](https://doi.org/10.1093/mnras/stx2704)
- Krist, J. 1995, in Astronomical Society of the Pacific Conference Series, Vol. 77, Astronomical Data Analysis Software and Systems IV, ed. R. A. Shaw, H. E. Payne, & J. J. E. Hayes, 349
- Krist, J. E., Hook, R. N., & Stoehr, F. 2011, in Society of Photo-Optical Instrumentation Engineers (SPIE) Conference Series, Vol. 8127, Optical Modeling and Performance Predictions V, ed. M. A. Kahan, 81270J, doi: [10.1117/12.892762](https://doi.org/10.1117/12.892762)
- Lyubenova, M., Kuntschner, H., Rejkuba, M., et al. 2012, A&A, 543, A75, doi: [10.1051/0004-6361/201218847](https://doi.org/10.1051/0004-6361/201218847)
- Ma, C.-P., Greene, J. E., McConnell, N., et al. 2014, ApJ, 795, 158, doi: [10.1088/0004-637X/795/2/158](https://doi.org/10.1088/0004-637X/795/2/158)
- Magorrian, J., Tremaine, S., Richstone, D., et al. 1998, AJ, 115, 2285, doi: [10.1086/300353](https://doi.org/10.1086/300353)
- Maraston, C., & Strömbäck, G. 2011, MNRAS, 418, 2785, doi: [10.1111/j.1365-2966.2011.19738.x](https://doi.org/10.1111/j.1365-2966.2011.19738.x)
- Markwardt, C. B. 2009, in Astronomical Society of the Pacific Conference Series, Vol. 411, Astronomical Data Analysis Software and Systems XVIII, ed. D. A. Bohlender, D. Durand, & P. Dowler, 251, doi: [10.48550/arXiv.0902.2850](https://doi.org/10.48550/arXiv.0902.2850)
- McConnell, N. J., & Ma, C.-P. 2013, ApJ, 764, 184, doi: [10.1088/0004-637X/764/2/184](https://doi.org/10.1088/0004-637X/764/2/184)
- McConnell, N. J., Ma, C.-P., Gebhardt, K., et al. 2011, Nature, 480, 215, doi: [10.1038/nature10636](https://doi.org/10.1038/nature10636)
- Merritt, D., Ferrarese, L., & Joseph, C. L. 2001, Science, 293, 1116, doi: [10.1126/science.1063896](https://doi.org/10.1126/science.1063896)
- Mezcua, M. 2017, International Journal of Modern Physics D, 26, 1730021, doi: [10.1142/S021827181730021X](https://doi.org/10.1142/S021827181730021X)
- Mitzkus, M., Cappellari, M., & Walcher, C. J. 2017, MNRAS, 464, 4789, doi: [10.1093/mnras/stw2677](https://doi.org/10.1093/mnras/stw2677)
- Miyoshi, M., Moran, J., Herrnstein, J., et al. 1995, Nature, 373, 127, doi: [10.1038/373127a0](https://doi.org/10.1038/373127a0)
- Müller, O., Durrell, P. R., Marleau, F. R., et al. 2021, ApJ, 923, 9, doi: [10.3847/1538-4357/ac2831](https://doi.org/10.3847/1538-4357/ac2831)
- Navarro, J. F., Frenk, C. S., & White, S. D. M. 1996, ApJ, 462, 563, doi: [10.1086/177173](https://doi.org/10.1086/177173)
- Netzer, H. 2015, ARA&A, 53, 365, doi: [10.1146/annurev-astro-082214-122302](https://doi.org/10.1146/annurev-astro-082214-122302)
- Neumayer, N., Seth, A., & Böker, T. 2020, A&A Rv, 28, 4, doi: [10.1007/s00159-020-00125-0](https://doi.org/10.1007/s00159-020-00125-0)
- Neumayer, N., & Walcher, C. J. 2012, Advances in Astronomy, 2012, 709038, doi: [10.1155/2012/709038](https://doi.org/10.1155/2012/709038)
- Nguyen, D. D. 2017, arXiv e-prints, arXiv:1712.02470, doi: [10.48550/arXiv.1712.02470](https://doi.org/10.48550/arXiv.1712.02470)
- Nguyen, D. D. 2019, in ALMA2019: Science Results and Cross-Facility Synergies, 106, doi: [10.5281/zenodo.3585410](https://doi.org/10.5281/zenodo.3585410)
- Nguyen, D. D., Cappellari, M., & Pereira-Santalla, M. 2023, MNRAS, 526, 3548, doi: [10.1093/mnras/stad2860](https://doi.org/10.1093/mnras/stad2860)
- Nguyen, D. D., Seth, A. C., Reines, A. E., et al. 2014, ApJ, 794, 34, doi: [10.1088/0004-637X/794/1/34](https://doi.org/10.1088/0004-637X/794/1/34)
- Nguyen, D. D., Seth, A. C., den Brok, M., et al. 2017, ApJ, 836, 237, doi: [10.3847/1538-4357/aa5cb4](https://doi.org/10.3847/1538-4357/aa5cb4)
- Nguyen, D. D., Seth, A. C., Neumayer, N., et al. 2018, ApJ, 858, 118, doi: [10.3847/1538-4357/aabe28](https://doi.org/10.3847/1538-4357/aabe28)
- Nguyen, D. D., Seth, A. C., Neumayer, N., et al. 2019, ApJ, 872, 104, doi: [10.3847/1538-4357/aafe7a](https://doi.org/10.3847/1538-4357/aafe7a)
- Nguyen, D. D., den Brok, M., Seth, A. C., et al. 2020, ApJ, 892, 68, doi: [10.3847/1538-4357/ab77aa](https://doi.org/10.3847/1538-4357/ab77aa)
- Nguyen, D. D., Izumi, T., Thater, S., et al. 2021, MNRAS, 504, 4123, doi: [10.1093/mnras/stab1002](https://doi.org/10.1093/mnras/stab1002)
- Nguyen, D. D., Bureau, M., Thater, S., et al. 2022, MNRAS, 509, 2920, doi: [10.1093/mnras/stab3016](https://doi.org/10.1093/mnras/stab3016)
- Nguyen, D. D., Ngo, H. N., Le, T. Q. T., et al. 2025, A&A, 698, L9, doi: [10.1051/0004-6361/202554672](https://doi.org/10.1051/0004-6361/202554672)
- Nightingale, J. W., Smith, R. J., He, Q., et al. 2023, MNRAS, 521, 3298, doi: [10.1093/mnras/stad587](https://doi.org/10.1093/mnras/stad587)
- Norris, M. A., Kannappan, S. J., Forbes, D. A., et al. 2014, MNRAS, 443, 1151, doi: [10.1093/mnras/stu1186](https://doi.org/10.1093/mnras/stu1186)
- Noyola, E., Gebhardt, K., Kissler-Patig, M., et al. 2010, ApJL, 719, L60, doi: [10.1088/2041-8205/719/1/L60](https://doi.org/10.1088/2041-8205/719/1/L60)
- Oke, J. B. 1974, ApJS, 27, 21, doi: [10.1086/190287](https://doi.org/10.1086/190287)
- Ordenes-Briceño, Y., Puzia, T. H., Eigenthaler, P., et al. 2018, ApJ, 860, 4, doi: [10.3847/1538-4357/aac1b8](https://doi.org/10.3847/1538-4357/aac1b8)
- Parodi, B. R., Barazza, F. D., & Binggeli, B. 2002, A&A, 388, 29, doi: [10.1051/0004-6361:20020432](https://doi.org/10.1051/0004-6361:20020432)

- Pechetti, R., Seth, A., Neumayer, N., et al. 2020, *ApJ*, 900, 32, doi: [10.3847/1538-4357/abaaa7](https://doi.org/10.3847/1538-4357/abaaa7)
- Pechetti, R., Seth, A., Kamann, S., et al. 2022, *ApJ*, 924, 48, doi: [10.3847/1538-4357/ac339f](https://doi.org/10.3847/1538-4357/ac339f)
- Peterson, R. C., & Caldwell, N. 1993, *AJ*, 105, 1411, doi: [10.1086/116520](https://doi.org/10.1086/116520)
- Pinna, F., Neumayer, N., Seth, A., et al. 2021, *ApJ*, 921, 8, doi: [10.3847/1538-4357/ac158f](https://doi.org/10.3847/1538-4357/ac158f)
- Rayner, J. T., Cushing, M. C., & Vacca, W. D. 2009, *ApJS*, 185, 289, doi: [10.1088/0067-0049/185/2/289](https://doi.org/10.1088/0067-0049/185/2/289)
- Rossa, J., van der Marel, R. P., Böker, T., et al. 2006, *AJ*, 132, 1074, doi: [10.1086/505968](https://doi.org/10.1086/505968)
- Saglia, R. P., Opitsch, M., Erwin, P., et al. 2016, *ApJ*, 818, 47, doi: [10.3847/0004-637X/818/1/47](https://doi.org/10.3847/0004-637X/818/1/47)
- Sahu, N., Graham, A. W., & Davis, B. L. 2019, *ApJ*, 876, 155, doi: [10.3847/1538-4357/ab0f32](https://doi.org/10.3847/1538-4357/ab0f32)
- Sánchez-Janssen, R., Côté, P., Ferrarese, L., et al. 2019, *ApJ*, 878, 18, doi: [10.3847/1538-4357/aaf4fd](https://doi.org/10.3847/1538-4357/aaf4fd)
- Schiavon, R. P. 2007, *ApJS*, 171, 146, doi: [10.1086/511753](https://doi.org/10.1086/511753)
- Schlafly, E. F., & Finkbeiner, D. P. 2011, *ApJ*, 737, 103, doi: [10.1088/0004-637X/737/2/103](https://doi.org/10.1088/0004-637X/737/2/103)
- Schombert, J., & Smith, A. K. 2012, *PASA*, 29, 174, doi: [10.1071/AS11059](https://doi.org/10.1071/AS11059)
- Sersic, J. L. 1968, *Atlas de galaxias australes* (Córdoba: Obs. Astron. Univ. Nacional de Córdoba)
- Seth, A., Agüeros, M., Lee, D., & Basu-Zych, A. 2008, *ApJ*, 678, 116, doi: [10.1086/528955](https://doi.org/10.1086/528955)
- Seth, A. C., Cappellari, M., Neumayer, N., et al. 2010, *ApJ*, 714, 713, doi: [10.1088/0004-637X/714/1/713](https://doi.org/10.1088/0004-637X/714/1/713)
- Seth, A. C., van den Bosch, R., Mieske, S., et al. 2014, *Nature*, 513, 398, doi: [10.1038/nature13762](https://doi.org/10.1038/nature13762)
- Shields, J. C., Walcher, C. J., Böker, T., et al. 2008, *ApJ*, 682, 104, doi: [10.1086/589680](https://doi.org/10.1086/589680)
- Silk, J., & Rees, M. J. 1998, *A&A*, 331, L1, doi: [10.48550/arXiv.astro-ph/9801013](https://doi.org/10.48550/arXiv.astro-ph/9801013)
- Skrutskie, M. F., Cutri, R. M., Stiening, R., et al. 2006, *AJ*, 131, 1163, doi: [10.1086/498708](https://doi.org/10.1086/498708)
- Spengler, C., Côté, P., Roediger, J., et al. 2017, *ApJ*, 849, 55, doi: [10.3847/1538-4357/aa8a78](https://doi.org/10.3847/1538-4357/aa8a78)
- Straub, O., Godet, O., Webb, N., Servillat, M., & Barret, D. 2014, *A&A*, 569, A116, doi: [10.1051/0004-6361/201423874](https://doi.org/10.1051/0004-6361/201423874)
- STScI. 2020, IPAC, doi: [10.26131/IRSA441](https://doi.org/10.26131/IRSA441)
- Thater, S., Lyubenova, M., Fahrion, K., et al. 2023, *A&A*, 675, A18, doi: [10.1051/0004-6361/202245362](https://doi.org/10.1051/0004-6361/202245362)
- Thatte, N. A., Clarke, F., Bryson, I., et al. 2016, in *Society of Photo-Optical Instrumentation Engineers (SPIE) Conference Series*, Vol. 9908, *Ground-based and Airborne Instrumentation for Astronomy VI*, ed. C. J. Evans, L. Simard, & H. Takami, 99081X, doi: [10.1117/12.2230629](https://doi.org/10.1117/12.2230629)
- Thatte, N. A., Bryson, I., Clarke, F., et al. 2020, in *Society of Photo-Optical Instrumentation Engineers (SPIE) Conference Series*, Vol. 11447, *Ground-based and Airborne Instrumentation for Astronomy VIII*, ed. C. J. Evans, J. J. Bryant, & K. Motohara, 114471W, doi: [10.1117/12.2562144](https://doi.org/10.1117/12.2562144)
- Thatte, N. A., Melotte, D., Neichel, B., et al. 2024, in *Society of Photo-Optical Instrumentation Engineers (SPIE) Conference Series*, Vol. 13096, *Ground-based and Airborne Instrumentation for Astronomy X*, ed. J. J. Bryant, K. Motohara, & J. R. D. Vernet, 1309614, doi: [10.1117/12.3018520](https://doi.org/10.1117/12.3018520)
- Tremaine, S., Richstone, D. O., Byun, Y.-I., et al. 1994, *AJ*, 107, 634, doi: [10.1086/116883](https://doi.org/10.1086/116883)
- Trujillo, I., Erwin, P., Asensio Ramos, A., & Graham, A. W. 2004, *AJ*, 127, 1917, doi: [10.1086/382712](https://doi.org/10.1086/382712)
- Valluri, M., Ferrarese, L., Merritt, D., & Joseph, C. L. 2005, *ApJ*, 628, 137, doi: [10.1086/430752](https://doi.org/10.1086/430752)
- van der Marel, R. P. 1999, *AJ*, 117, 744, doi: [10.1086/300730](https://doi.org/10.1086/300730)
- van der Marel, R. P., & Anderson, J. 2010, *ApJ*, 710, 1063, doi: [10.1088/0004-637X/710/2/1063](https://doi.org/10.1088/0004-637X/710/2/1063)
- van Wassenhove, S., Volonteri, M., Walker, M. G., & Gair, J. R. 2010, *MNRAS*, 408, 1139, doi: [10.1111/j.1365-2966.2010.17189.x](https://doi.org/10.1111/j.1365-2966.2010.17189.x)
- Verolme, E. K., Cappellari, M., Copin, Y., et al. 2002, *MNRAS*, 335, 517, doi: [10.1046/j.1365-8711.2002.05664.x](https://doi.org/10.1046/j.1365-8711.2002.05664.x)
- Volonteri, M. 2012, *Science*, 337, 544, doi: [10.1126/science.1220843](https://doi.org/10.1126/science.1220843)
- Volonteri, M., Habouzit, M., & Colpi, M. 2021, *Nature Reviews Physics*, 3, 732, doi: [10.1038/s42254-021-00364-9](https://doi.org/10.1038/s42254-021-00364-9)
- Walcher, C. J., Böker, T., Charlot, S., et al. 2006, *ApJ*, 649, 692, doi: [10.1086/505166](https://doi.org/10.1086/505166)
- Walcher, C. J., van der Marel, R. P., McLaughlin, D., et al. 2005, *ApJ*, 618, 237, doi: [10.1086/425977](https://doi.org/10.1086/425977)
- Wallace, L., & Hinkle, K. 1996, *ApJS*, 107, 312, doi: [10.1086/192367](https://doi.org/10.1086/192367)
- Wallace, L., & Hinkle, K. 1997, *ApJS*, 111, 445, doi: [10.1086/313020](https://doi.org/10.1086/313020)
- Walsh, J. L., Barth, A. J., Ho, L. C., & Sarzi, M. 2013, *ApJ*, 770, 86, doi: [10.1088/0004-637X/770/2/86](https://doi.org/10.1088/0004-637X/770/2/86)
- Williams, B. F., Dalcanton, J. J., Stilp, A., et al. 2013, *ApJ*, 765, 120, doi: [10.1088/0004-637X/765/2/120](https://doi.org/10.1088/0004-637X/765/2/120)
- Zhu, K., Cappellari, M., Mao, S., et al. 2025, arXiv e-prints, arXiv:2503.06968, doi: [10.48550/arXiv.2503.06968](https://doi.org/10.48550/arXiv.2503.06968)
- Zieleniewski, S., Thatte, N., Kendrew, S., et al. 2015, *MNRAS*, 453, 3754, doi: [10.1093/mnras/stv1860](https://doi.org/10.1093/mnras/stv1860)
- Zocchi, A., Gieles, M., & Hénault-Brunet, V. 2017, *MNRAS*, 468, 4429, doi: [10.1093/mnras/stx316](https://doi.org/10.1093/mnras/stx316)
- Zocchi, A., Gieles, M., & Hénault-Brunet, V. 2019, *MNRAS*, 482, 4713, doi: [10.1093/mnras/sty1508](https://doi.org/10.1093/mnras/sty1508)

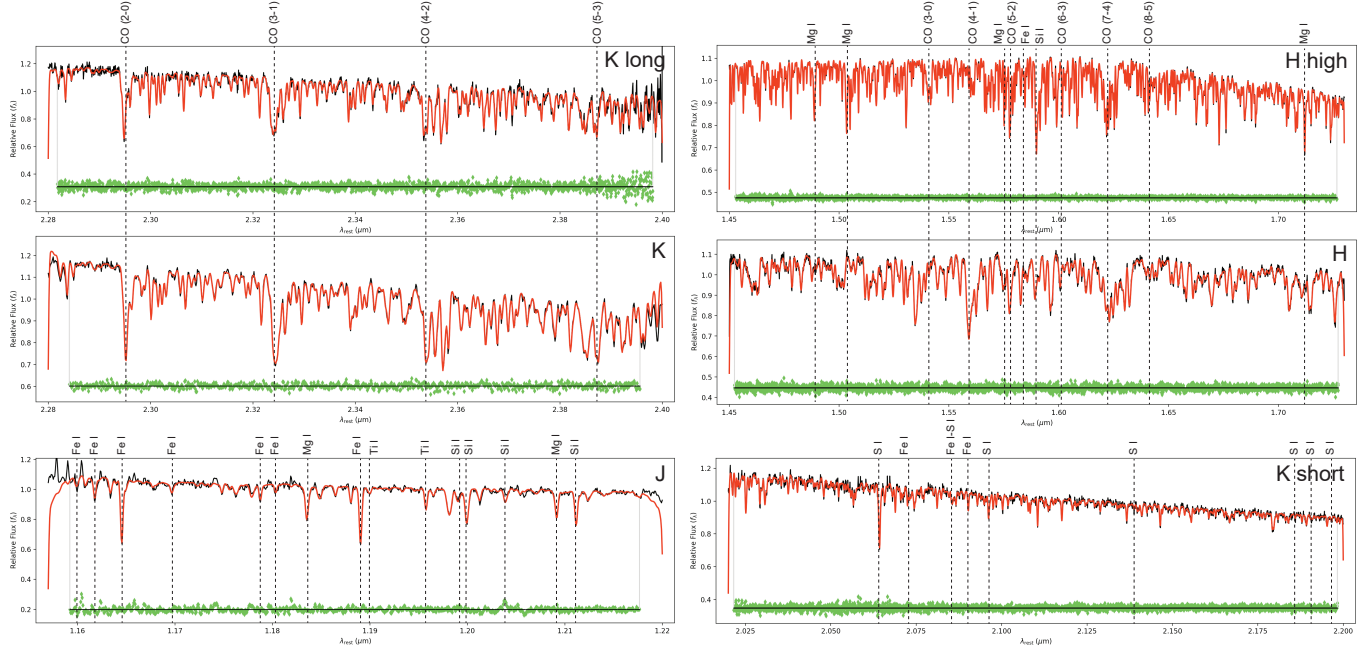


Figure 13. Parts of the simulated spectra over six HSIM data cubes, which are fixed as the best spectral wavelength ranges for measuring the stellar kinematics for NGC 300 and NGC 3115 dw01, including $\lambda 2.28$ – $2.40 \mu\text{m}$ for both the K - and K -long, $\lambda 1.45$ – $1.74 \mu\text{m}$ for both the H - and H -high, and $\lambda 1.16$ – $1.218 \mu\text{m}$ for the J - and $\lambda 2.05$ – $2.20 \mu\text{m}$ for K -long, specifically. For the fixed spectra parts of the K - and K -long bands, we used the CO absorption bandheads (e.g. $^{12}\text{CO}(2-0) \lambda 2.293 \mu\text{m}$, $^{12}\text{CO}(3-1) \lambda 2.312 \mu\text{m}$, $^{12}\text{CO}(4-2) \lambda 2.351 \mu\text{m}$, and $^{12}\text{CO}(5-3) \lambda 2.386 \mu\text{m}$; L. Wallace & K. Hinkle 1997). For the fixed spectra parts of the H - and H -bands, we used the atomic-absorption species of Mg I $\lambda 1.487$, 1.503 , 1.575 , $1.711 \mu\text{m}$; Fe I $\lambda 1.583 \mu\text{m}$; Si I $\lambda 1.589 \mu\text{m}$ and the CO-absorptions lines of $^{12}\text{CO}(3-0) \lambda 1.540 \mu\text{m}$; $^{12}\text{CO}(4-1) \lambda 1.561 \mu\text{m}$; $^{12}\text{CO}(5-2) \lambda 1.577 \mu\text{m}$; $^{12}\text{CO}(6-3) \lambda 1.602 \mu\text{m}$; $^{12}\text{CO}(7-4) \lambda 1.622 \mu\text{m}$; $^{12}\text{CO}(8-5) \lambda 1.641 \mu\text{m}$. For the fixed spectrum part of the J -band, we used the atomic-absorption species of Ti I $\lambda 1.1896$, $1.1953 \mu\text{m}$; Si I $\lambda 1.1988$, 1.1995 , 1.2035 , $1.2107 \mu\text{m}$; Mg I $\lambda 1.1831$, $1.2087 \mu\text{m}$; Fe I $\lambda 1.1597$, 1.1611 , 1.1641 , 1.1693 , 1.1783 , 1.1801 , 1.1887 , $1.1976 \mu\text{m}$. For the fixed spectrum part of the K -short band, we used the atomic-absorption lines of Fe I $\lambda 2.088$, $2.070 \mu\text{m}$; Si I $\lambda 2.188$, 2.183 , 2.179 , 2.137 , 2.092 , $2.062 \mu\text{m}$, and the blended-absorption features of Fe I – Si I at $\lambda 2.070$, $\lambda 2.083 \mu\text{m}$. In each panel plot, the black vertically thin-dashed lines indicate the positions of atomic/molecule absorptions features of the stellar component extracted from one bin (black line) and its best-fit model produced by pPXF (red line). The two gray-vertical lines limit the wavelength range where the spectrum was fit, and blue dots show the residual between the galaxy spectrum and the best-fitting model (data-model). The kinematic results of these pPXF fits are shown in Figure 7 and Figure 14 for NGC 300 and Figure 8 and Figure 15 for NGC 3115 dw01 in terms of the 2D maps.

APPENDIX

A. SUPPLEMENTARY FIGURES AND TABLES

Table 6. Full list of our HARMONI IMBH survey: host galaxies' and their nuclear star clusters' properties

No.	Galaxy Name	R.A. (J2000) (h:m:s)	Decl. (J2000) (d:m:s)	D (Mpc)	Hubble Type	L_K (L_\odot)	$M_{\star, \text{gal.}}$ (M_\odot)	$\sigma_{\star, \text{NSC}}$ (km s $^{-1}$)	$R_{e, \text{gal}}$ (kpc)	M_{NSC} (M_\odot)	$R_{e, \text{NSC}}$ (pc)	ref.
(1)	(2)	(3)	(4)	(5)	(6)	(7)	(8)	(9)	(10)	(11)	(12)	(13)
1	PGC046680	13:22:02.048	-42:32:07.34	3.77	-3.0	1.32×10^8	4.0×10^7	13.2	0.73	4.30×10^6	3.0	(1)
2	NGC 5206	13:33:43.961	-48:09:03.95	3.50	-3.0	1.05×10^9	2.5×10^9	46.0	0.99	1.54×10^7	3.4	(2)
3	ESO269-066	13:13:09.156	-44:53:23.63	3.66	-2.1	2.75×10^8	1.0×10^8	-	0.70	1.55×10^6	-	-
4	ESO269-068	13:13:11.917	-43:15:54.69	3.77	-2.1	8.91×10^7	1.7×10^7	-	0.41	6.10×10^5	15.2	(11)
5	NGC 4600	12:40:22.957	03:07:03.91	8.15	0.0	1.32×10^9	1.2×10^9	73.6	0.94	1.03×10^7	8.3	(2)
6	NGC 5102	13:21:57.610	-36:37:48.37	3.20	0.0	4.27×10^9	6.9×10^9	61.1	1.20	7.30×10^7	26.3	(3)
7	NGC 300	00:54:53.444	-37:41:03.22	2.01	6.9	5.00×10^8	1.0×10^9	47.0	2.94	1.05×10^6	8.0	(4, 5)
8	NGC 7793	23:57:49.753	-32:35:27.74	3.40	7.4	7.94×10^7	2.8×10^9	24.6	2.19	7.76×10^6	7.9	(4, 5)
9	NGC 3621	11:18:16.511	-32:48:50.55	6.60	7.0	2.24×10^{10}	7.9×10^9	43.0	2.60	1.01×10^7	4.2	(6)
10	NGC 247	00:47:08.470	-20:45:36.71	3.38	6.9	3.16×10^9	3.0×10^9	15.1	2.46	2.51×10^6	3.4	(7)
11	IC3077	12:24:22.180	21:09:35.95	9.12	5.8	1.45×10^8	1.3×10^9	25.0	1.40	-	-	-
12	NGC 5237	13:37:39.050	-42:50:49.099	3.33	-3.5	2.82×10^8	1.6×10^8	48.5	0.34	-	-	-
13	PGC029300	10:05:41.599	-07:58:53.40	9.70	-1.9	1.86×10^9	2.8×10^9	32.0	1.20	7.01×10^6	6.6	(3)
14	ESO384-016	13:57:01.370	-35 19 58.699	4.49	-4.9	6.76×10^7	6.0×10^7	-	0.69	-	-	-
15	ESO174-001	13:33:19.680	-53:21:16.88	3.60	-1.7	7.94×10^7	7.9×10^7	-	0.42	-	-	-
16	MESSIER083	13:37:00.950	-29:51:55.50	4.85	5.0	7.24×10^{10}	4.5×10^{10}	40.0	5.29	1.67×10^6	4.9	-
17	NGC 3593	11:14:37.001	12:49:03.61	9.20	-4.8	2.69×10^{10}	1.5×10^{10}	60.0	1.90	1.58×10^8	6	(3, 8)
18	ESO274-G001	15:14:14.554	-46:48:19.32	3.15	6.7	8.32×10^8	5.0×10^8	17.2	1.45	2.54×10^6	2.0	(3)
19	NGC 4713	12:49:57.874	05:18:41.04	10.7	6.8	-	3.0×10^{10}	23.2	2.12	-	-	-
20	NGC 3351	10:43:57.701	11:42:13.72	9.46	3.1	2.00×10^{10}	2.0×10^{10}	67.0	3.95	1.45×10^6	4.4	(9)
21	IC 5332	23:34:27.490	-36:06:03.89	4.63	6.8	5.50×10^9	4.7×10^9	58.3	1.18	6.95×10^6	23.2	(3)
22	NGC 1493	03:57:27.430	-46:12:38.52	11.3	6.0	-	4.0×10^9	25.0	-	1.51×10^6	4.2	-
23	NGC 1042	02:40:23.966	-08:26:00.74	4.21	6.0	-	2.1×10^9	32.0	1.09	2.12×10^6	1.3	(4)
24	NGC 628	01:36:41.747	15:47:01.18	4.21	5.2	3.98×10^{10}	1.4×10^{10}	72.2	6.60	1.13×10^7	5.4	(10)
25	ESO059-01	07:31:18.00	-68:11:14	4.57	9.8	1.48×10^8	5.1×10^7	-	-	1.45×10^6	-	-
26	UGC 3755	07:13:51.57	10:31:16.53	4.99	9.9	2.69×10^8	9.3×10^7	-	-	6.03×10^4	0.5	(10)
27	IC 1959	03:33:12.53	-50:24:52.19	6.05	8.4	3.09×10^8	1.4×10^8	-	-	1.35×10^6	-	-
28	UGC 5889	10:47:22.4	14:04:16.58	6.89	8.9	3.55×10^8	1.6×10^8	-	-	1.23×10^6	1.0	(10)
29	NGC 4592	12:39:18.76	-00:31:55.61	10.6	7.9	1.45×10^9	1.0×10^9	38.9	-	6.31×10^5	1.1	(10)
30	NGC 1796	05:02:41.27	-61 08 18.79	10.6	5.3	-	1.2×10^9	-	-	6.61×10^6	2.6	-
31	ESO359-G029	04:12:50.52	-33:00:10.34	10.1	9.9	-	2.3×10^8	29.5	-	1.48×10^5	0.5	(10)
32	IC 4710	18:28:40.9	-66:59:10.0	8.91	8.9	1.74×10^9	1.3×10^9	67.2	-	2.49×10^6	1.0	(10)
33	NGC 1566	04:20:0.4	-54:56:16.5	9.95	4.0	-	1.5×10^{10}	116	-	1.49×10^8	2.3	(12)
34	NGC 2835	09:17:52.85	-22:21:16.79	10.8	5.0	2.19×10^{10}	5.1×10^9	70.7	-	4.07×10^6	3.4	(10)
35	NGC 4204	12:15:14.44	20:39:30.14	7.8	7.8	1.32×10^9	4.9×10^8	20.1	-	1.44×10^5	0.9	(10)
36	NGC 4517	12:32:45.51	00:06:54.9	10.6	6.0	1.86×10^{10}	1.2×10^{10}	28.3	-	7.01×10^5	2.3	(10)
37	NGC 5068	13:18:54.77	-21:02:19.66	6.03	6.0	5.37×10^9	4.83×10^9	15.6	-	5.31×10^5	5.1	(10)
38	NGC 5264	-	-	4.51	9.7	7.59×10^8	3.40×10^8	51.0	-	5.83×10^5	0.5	(10)
39	NGC 7090	21:36:28.19	-54 33 19.86	8.71	5.0	1.10×10^{10}	4.36×10^9	56.3	-	3.03×10^6	2.4	(10)
40	[KK2000] 03	02 24 44.4	-73 30 51	2.12	-4.9	7.70×10^7	2.30×10^7	-	-	1.35×10^5	3.8	(11)
41	LV J0956-0929	09 56 37.57	-09 29 10.8	9.37	-5	-	1.95×10^8	-	-	9.12×10^5	3.0	(11)
42	UGC 01104	01 32 42.53	+18 19 01.6	7.55	9.5	3.28×10^8	1.00×10^8	-	8.17	-	3.7	(11)
43	PGC 154449	09 57 08.88	-09 15 48.7	9.68	-1	1.60×10^8	5.01×10^7	-	5.25	-	-	(11)
44	ESO 553-046	05 27 05.72	-20 40 41.1	6.7	4	1.56×10^8	4.79×10^7	-	1.47	1.10×10^6	4.3	(11)

Notes: Columns 2–5: Galaxy name, R.A., and Decl., and distance to the galaxy. Column 6: Galaxy Hubble type. Columns 7 and 8: Total galaxy's K -band luminosity and total galaxy stellar mass. Columns 9–12: the nucleus stellar velocity dispersion, the galaxy effective radius that enclosed half of the galaxy mass or light, the nuclear star cluster mass, and the effective radius, respectively. Column 13: references - (1): [K. Fahrion et al. \(2020\)](#), (2): [D. D. Nguyen et al. \(2018\)](#), (3): [R. Pechetti et al. \(2020\)](#), (4): [C. J. Walcher et al. \(2005\)](#), (5): [N. Neumayer & C. J. Walcher \(2012\)](#), (6): [A. J. Barth et al. \(2009\)](#), (7): [S. G. Carlsten et al. \(2022\)](#), (8): [D. D. Nguyen et al. \(2021\)](#), (9): [A. Ashok et al. \(2023\)](#), (10): [I. Y. Georgiev & T. Böker \(2014\)](#), (11): [N. Hoyer et al. \(2023\)](#). Target numbers from 41–45 are galaxies those are not present in [Figure 3](#) (main text).

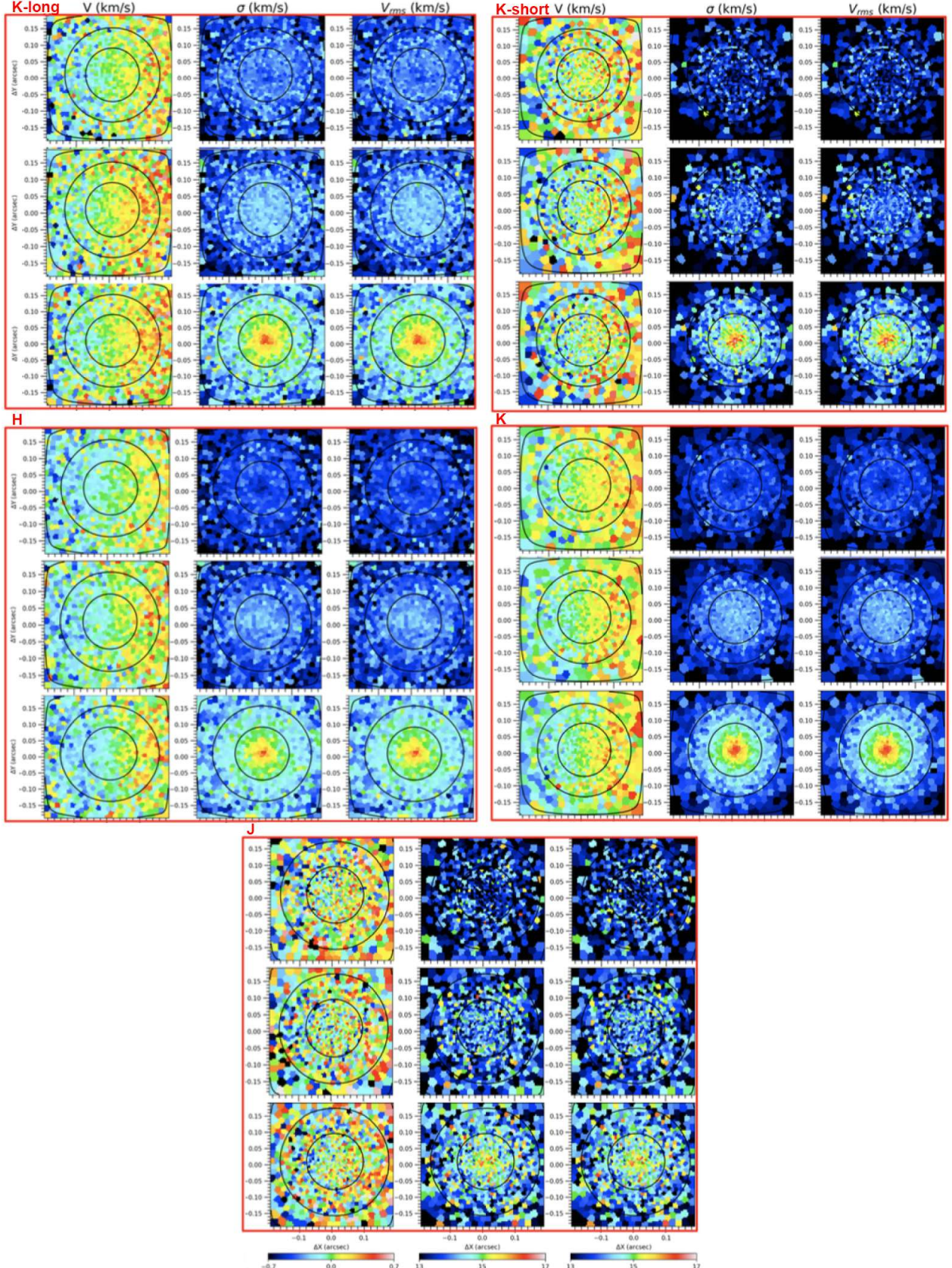


Figure 14. The stellar kinematic maps of NGC 300 extracted from the spectral part of $\lambda 2.28\text{--}2.40 \mu\text{m}$ (K and K -long band), $\lambda 2.05\text{--}2.20 \mu\text{m}$ (K -short band), $\lambda 1.15\text{--}1.22 \mu\text{m}$ (H band), $\lambda 1.15\text{--}1.22 \mu\text{m}$ (J band) HSIM IFS produced from JAM_{cyl} (M. Cappellari 2020) using pPXF (M. Cappellari 2023). In each red rectangular, these maps are present with three M_{BH} : $= 0 M_{\odot}$ (first row), $= 5 \times 10^3 M_{\odot}$ (second row), and $= 10^4 M_{\odot}$ (third row). On each row, the kinematic maps are listed orderly with V , σ_{\star} , and V_{rms} . The contours indicate the isophotes from the collapsed HSIM IFS cubes spaced by $1 \text{ mag arcsec}^{-2}$. The color bars are fixed at the same scale for all three M_{BH} to illustrate the kinematic effects of the central BHs and also indicate the robustness of our proposed kinematic measurements at the centers of these dwarf galaxies hosting bright NSCs as the kinematic signatures for IMBHs.

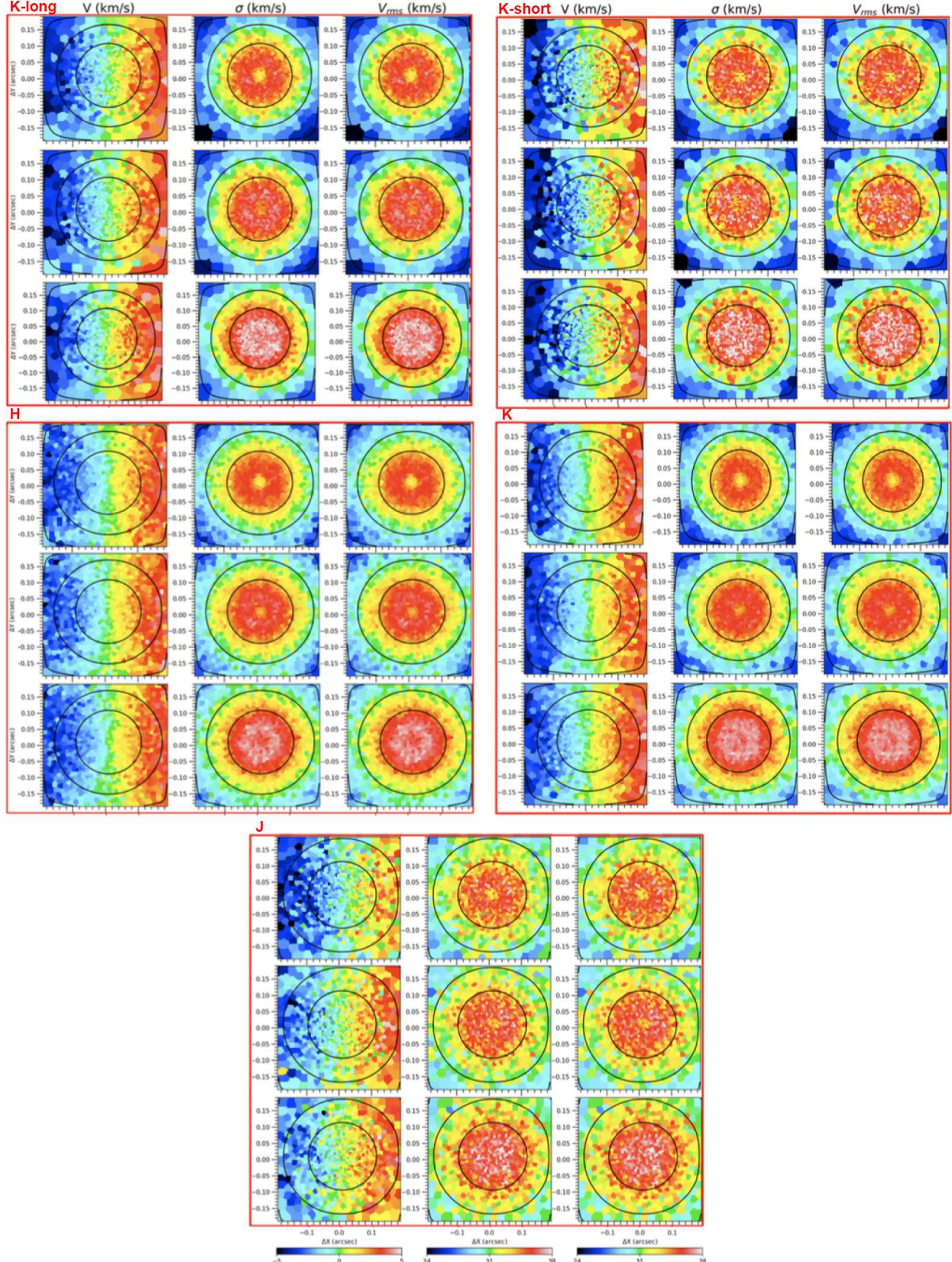


Figure 15. The stellar kinematic maps of NGC 3115 dw01 extracted from the spectral part of $\lambda 2.28\text{--}2.40\ \mu\text{m}$ (K and K -long band), $\lambda 2.05\text{--}2.20\ \mu\text{m}$ (K -short band), $\lambda 1.15\text{--}1.22\ \mu\text{m}$ (H band), $\lambda 1.15\text{--}1.22\ \mu\text{m}$ (J band) HSIM IFS produced from JAM_{cyl} ([M. Cappellari 2020](#)) using pPXF ([M. Cappellari 2023](#)). In each red rectangular, these maps are present with three M_{BH} : $= 0\ M_{\odot}$ (first row), $= 3.5 \times 10^4\ M_{\odot}$ (second row), and $= 7 \times 10^4\ M_{\odot}$ (third row). On each row, the kinematic maps are listed orderly with V , σ_{\star} , and V_{rms} . The contours indicate the isophotes from the collapsed HSIM IFS cubes spaced by 1 mag arcsec $^{-2}$. The color bars are fixed at the same scale for all three M_{BH} to illustrate the kinematic effects of the central BHs and also indicate the robustness of our proposed kinematic measurements at the centers of these dwarf galaxies hosting bright NSCs as the kinematic signatures for IMBHs.

Table 7. The stellar-light MGE models of NGC 300 and NGC 3115 dw01

$\log_{10} \Sigma_{\star,j} (L_{\odot} \text{pc}^{-2})$	$\sigma_j (\text{''})$	$q'_j = b_j/a_i$	$\log_{10} \Sigma_{\star,j} (L_{\odot} \text{pc}^{-2})$	$\sigma_j (\text{''})$	$q'_j = b_j/a_i$	
(1)	(2)	(3)	(4)	(5)	(6)	(7)
j	NGC 300	NGC 300	NGC 300	NGC 3115 dw01	NGC 3115 dw01	NGC 3115 dw01
1	3.954	0.0007	0.90	4.298	0.0069	0.90
2	3.745	0.0012	0.90	4.791	0.0512	0.90
3	3.714	0.0020	0.90	4.339	0.1044	0.90
4	3.377	0.0028	0.90	3.201	0.2293	0.90
5	3.195	0.0039	0.90	2.886	0.6191	0.90
6	3.774	0.0052	0.90	2.739	1.3815	0.90
7	3.971	0.0119	0.90	2.570	2.8272	0.90
8	3.159	0.0174	0.90	2.376	5.4128	0.90
9	3.456	0.0267	0.90	2.154	9.8186	0.90
10	4.334	0.0358	0.90	1.905	17.040	0.90
11	4.778	0.0877	0.90	1.632	28.594	0.90
12	3.620	0.1103	0.90	1.332	47.157	0.90
13	4.814	0.1774	0.90	0.994	78.302	0.90
14	4.518	0.5033	0.75	0.587	136.755	0.90
15	3.312	57.735	0.75	-0.019	288.675	0.90

Notes: The MGE models used in JAM_{cyl} model to create the input cubes for HSIM (subsection 6.2) and recover the IMBH mass (subsection 7.1). Each MGE model has 15 Gaussian components as shown in Column 1. Columns 2, 3 and 4: The MGE models that represented the mass models of the galaxies when scaled with a constant M/L_{F814W} , the dispersion of Gaussians, and the ratio between the semimajor and semiminor axes for NGC 300, respectively. Columns 5, 6 and 7: Similarities of Columns 2, 3 and 4 but for NGC 3115 dw01. Bold-face numbers are representative parameters for the Gaussians decomposed from the Core-Sérsic profile, which describes the NSC.

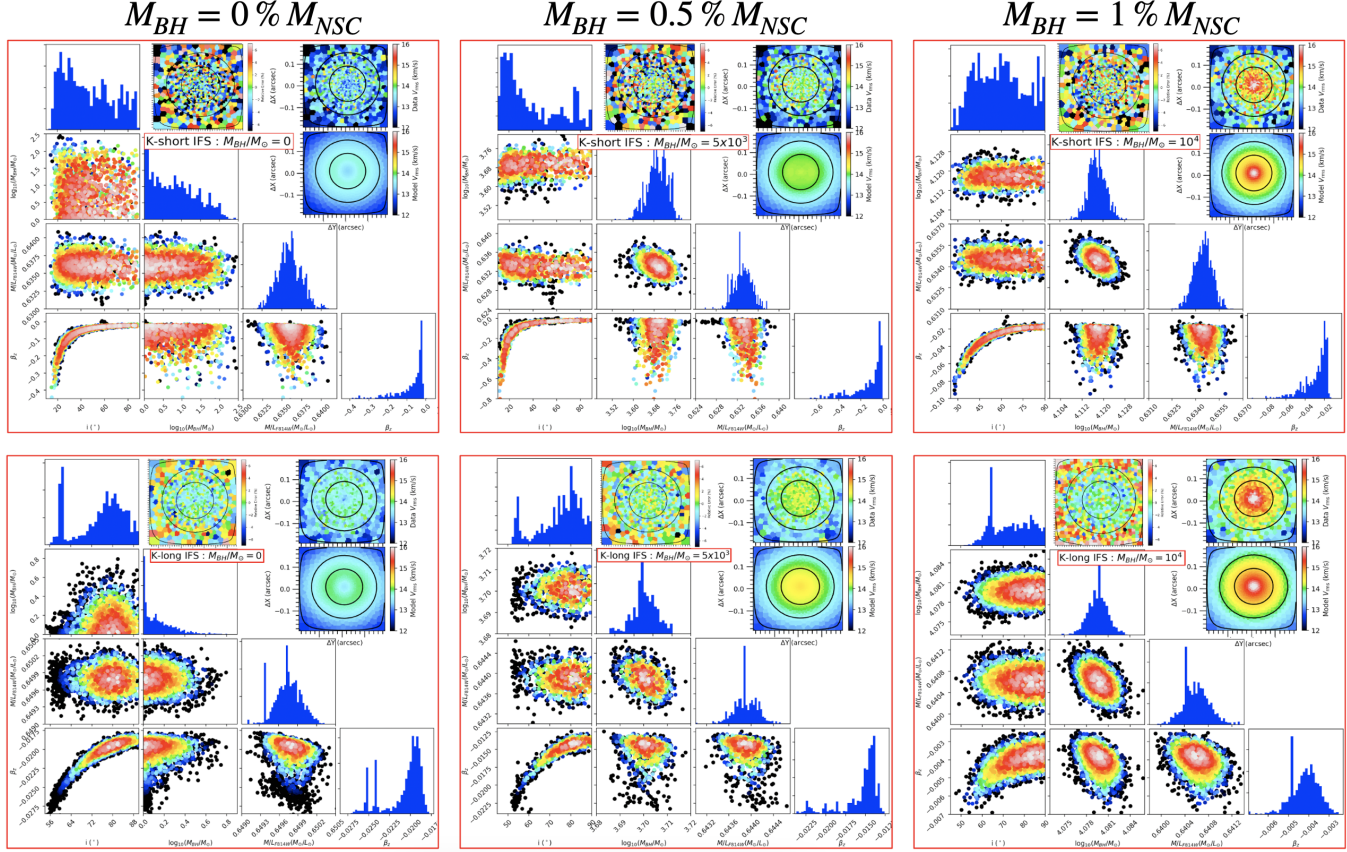


Figure 16. The posterior distributions obtained after the burn-in phase of the admet MCMC optimization process for the JAM_{cyl} models applied to the K -short and K -long HSIM kinematics of NGC 300. These simulations were generated using the JAM_{cyl} models and feature three $M_{BH} = 0 M_{\odot}$ (left), $= 5 \times 10^3 M_{\odot}$ (middle), and $= 10^4 M_{\odot}$ (right). Each red-square panel presents a set of four parameters (i , M_{BH} , M/L_{F814W} , and β_z), depicted as scatter plots illustrating their projected 2D distributions and histograms displaying their projected 1D distributions. In the top right corner, there are inset maps that depict the V_{rms} values. The top maps represent the simulated kinematic maps extracted from the simulated datacubes, while the bottom maps represent the kinematic maps recovered from the best-fit JAM_{cyl} model. These maps visually illustrate the level of agreement or disagreement at each spaxel between the simulated data and our best-fit model. The determination of the best-fit JAM_{cyl} model is based on the PDF with the highest likelihood.

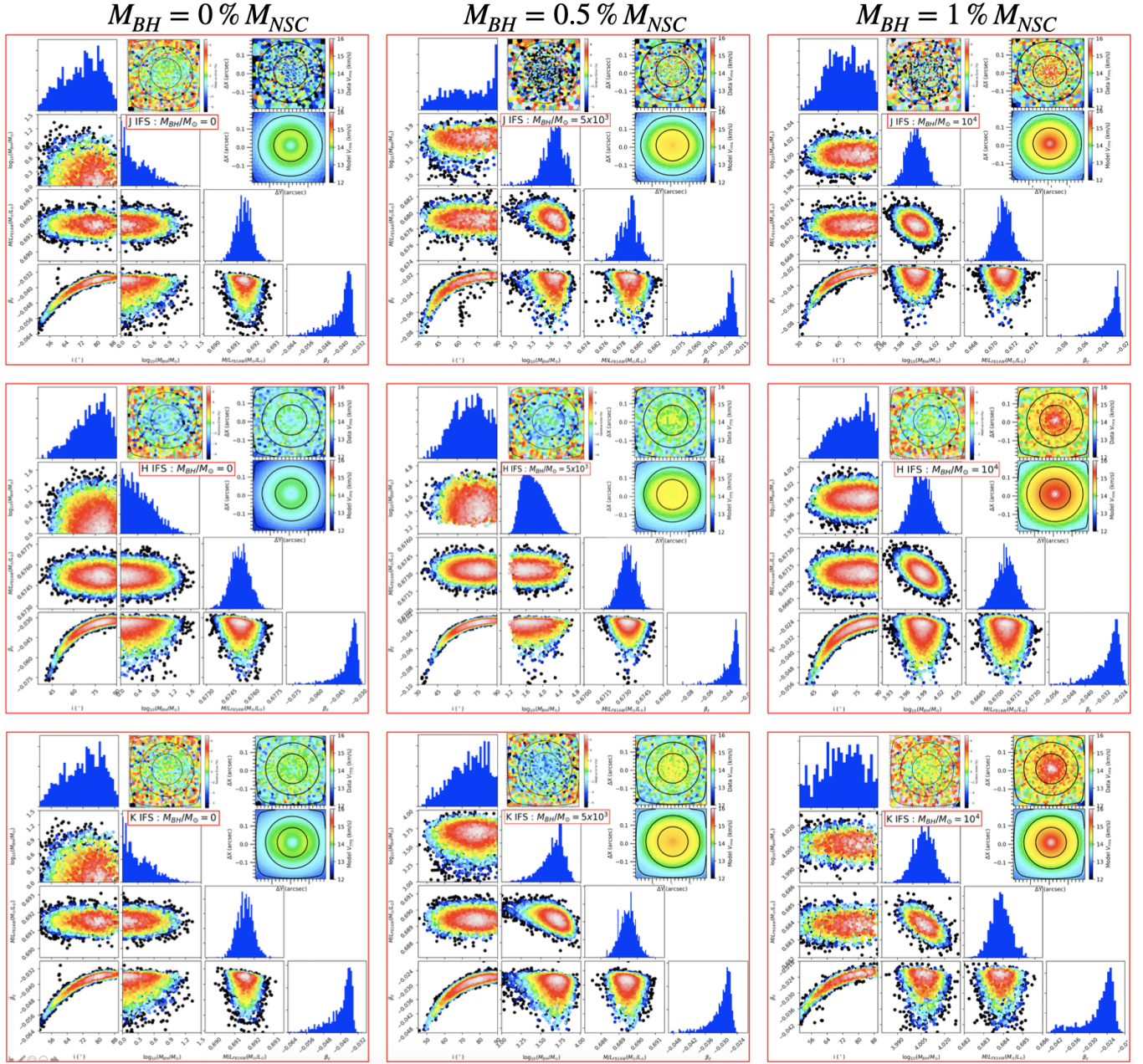


Figure 17. The posterior distributions obtained after the burn-in phase of the admet MCMC optimization process for the JAM_{cyl} models applied to the J , H , and K HSIM kinematics of NGC 300. These simulations were generated using the JAM_{cyl} models and feature three M_{BH} : $= 0 M_{\odot}$ (left), $= 5 \times 10^3 M_{\odot}$ (middle), and $= 10^4 M_{\odot}$ (right). Each red-square panel presents a set of four parameters (i , M_{BH} , M/L_{F814W} , and β_z), depicted as scatter plots illustrating their projected 2D distributions and histograms displaying their projected 1D distributions. In the top right corner, there are inset maps that depict the V_{rms} values. The top maps represent the simulated kinematic maps extracted from the simulated datacubes, while the bottom maps represent the kinematic maps recovered from the best-fit JAM_{cyl} model. These maps visually illustrate the level of agreement or disagreement at each spaxel between the simulated data and our best-fit model. The determination of the best-fit JAM_{cyl} model is based on the PDF with the highest likelihood.

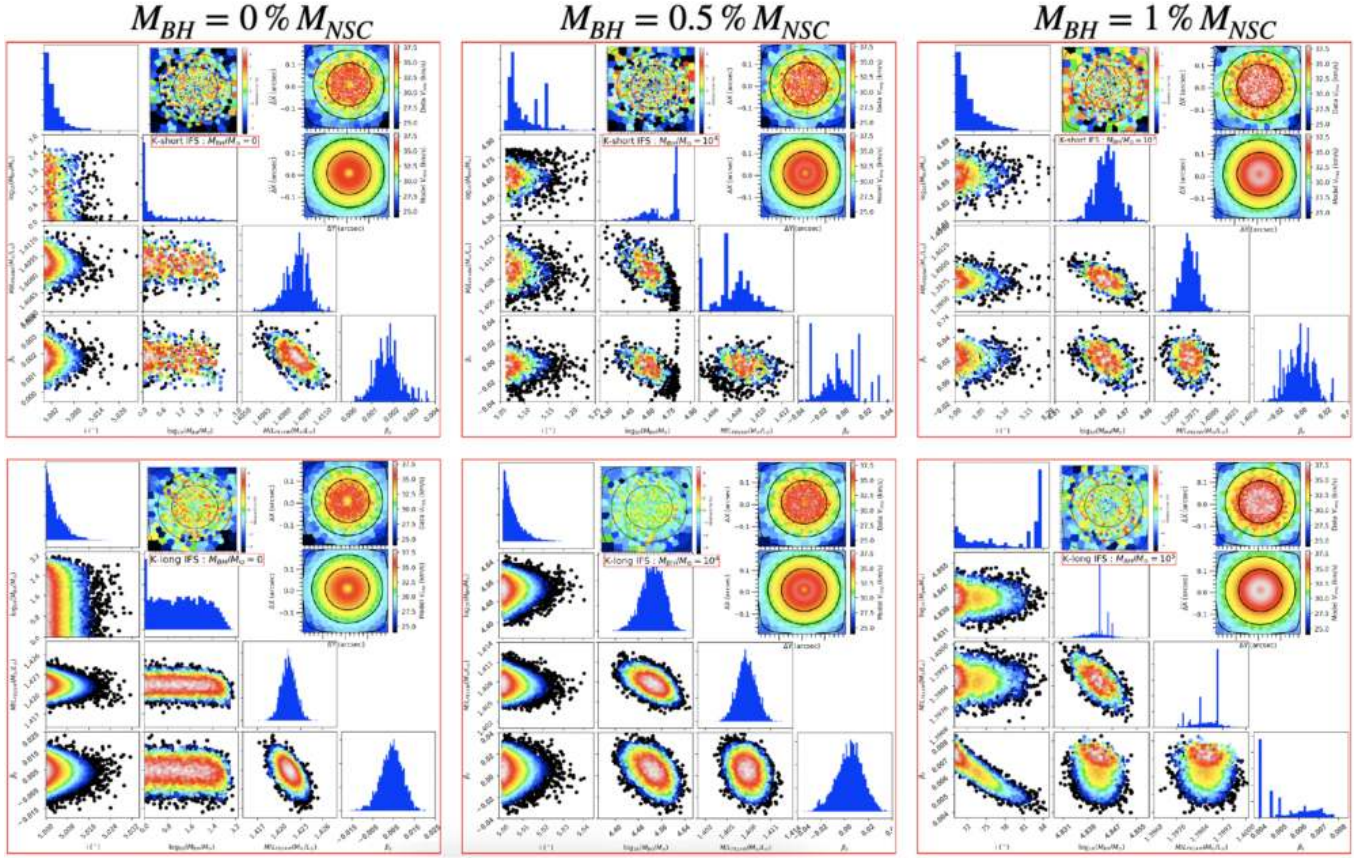


Figure 18. The posterior distributions obtained after the burn-in phase of the adamet MCMC optimization process for the JAM_{cyl} models applied to the K -short and K -long HSIM kinematics of NGC 3115 dw01. These simulations were generated using the JAM_{cyl} models and feature three M_{BH} : $= 0 M_{\odot}$ (left), $= 3.5 \times 10^4 M_{\odot}$ (middle), and $= 7 \times 10^4 M_{\odot}$ (right). Each red-square panel presents a set of four parameters (i , M_{BH} , M/L_{F814W} , and β_z), depicted as scatter plots illustrating their projected 2D distributions and histograms displaying their projected 1D distributions. In the top right corner, there are inset maps that depict the V_{rms} values. The top maps represent the simulated kinematic maps extracted from the simulated datacubes, while the bottom maps represent the kinematic maps recovered from the best-fit JAM_{cyl} model. These maps visually illustrate the level of agreement or disagreement at each spaxel between the simulated data and our best-fit model. The determination of the best-fit JAM_{cyl} model is based on the PDF with the highest likelihood.

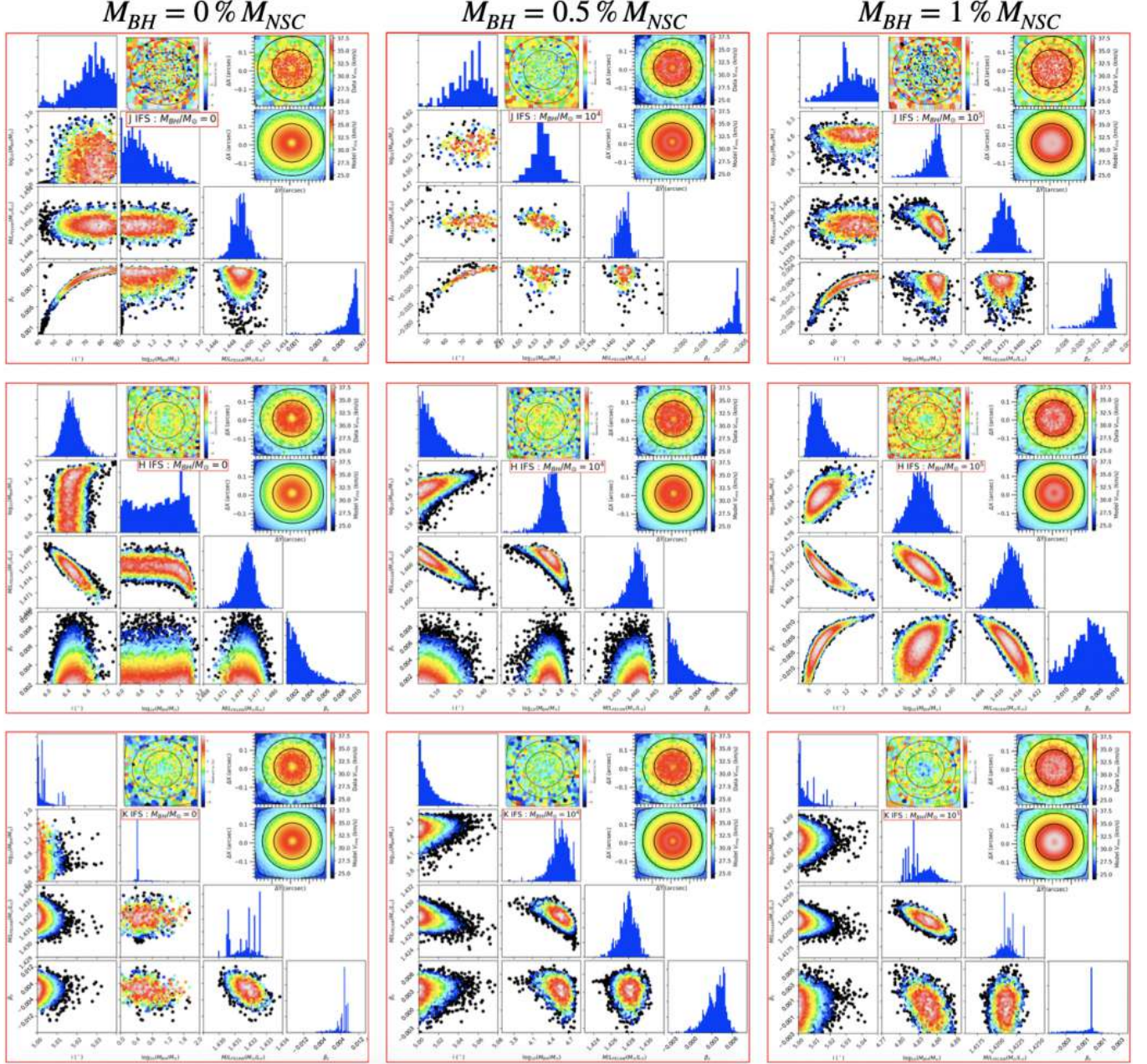


Figure 19. The posterior distributions obtained after the burn-in phase of the admet MCMC optimization process for the JAM_{cyl} models applied to the J , H , and K HSTM kinematics of NGC 3115 dw01. These simulations were generated using the JAM_{cyl} models and feature three M_{BH} : $= 0 M_{\odot}$ (left), $= 3.5 \times 10^4 M_{\odot}$ (middle), and $= 7 \times 10^4 M_{\odot}$ (right). Each red-square panel presents a set of four parameters (i , M_{BH} , M/L_{F814W} , and β_z), depicted as scatter plots illustrating their projected 2D distributions and histograms displaying their projected 1D distributions. In the top right corner, there are inset maps that depict the V_{rms} values. The top maps represent the simulated kinematic maps extracted from the simulated datacubes, while the bottom maps represent the kinematic maps recovered from the best-fit JAM_{cyl} model. These maps visually illustrate the level of agreement or disagreement at each spaxel between the simulated data and our best-fit model. The determination of the best-fit JAM_{cyl} model is based on the PDF with the highest likelihood.

Table 8. Best-fit JAM_{cyl} parameters and their statistical uncertainties for six mock IFS of NGC 300

Grating (1)	Parameters (2)	input $M_{\text{BH}} = 0 \text{ M}_{\odot}$			input $\log_{10}(M_{\text{BH}}/\text{M}_{\odot}) = 3.7$			input $\log_{10}(M_{\text{BH}}/\text{M}_{\odot}) = 4$		
		(3) best-fit	(4) 1σ	(5) 3σ	(6) best-fit	(7) 1σ	(8) 3σ	(9) best-fit	(10) 1σ	(11) 3σ
		(16-84%) (0.14-99.86%)			(0.14-99.86%) (16-84%)			(16-84%) (0.14-99.86%)		
<i>H</i> -high	$\log_{10}(M_{\text{BH}}/\text{M}_{\odot})$	0.1	<0.5	<0.8	3.710	± 0.012	± 0.025	4.04	± 0.01	± 0.03
	$M/L_{\text{F814W}} (M_{\odot}/L_{\odot})$	0.676	± 0.001	± 0.003	0.67	± 0.001	± 0.003	0.665	± 0.001	± 0.002
	$i(^{\circ})$	77.2	± 7.7	± 19.0	80.0	± 9.1	± 17.6	80.0	± 8.2	± 17.2
	β_z	-0.027	± 0.002	± 0.006	-0.019	± 0.002	± 0.005	-0.017	± 0.002	± 0.006
<i>K</i> -short	$\log_{10}(M_{\text{BH}}/\text{M}_{\odot})$	0.5	<1.9	<2.4	3.70	± 0.04	± 0.17	4.117	± 0.004	± 0.013
	$M/L_{\text{F814W}} (M_{\odot}/L_{\odot})$	0.636	± 0.002	± 0.004	0.635	± 0.002	± 0.006	0.634	± 0.001	± 0.003
	$i(^{\circ})$	84	± 26	± 37	56	± 30	± 40	89	± 20	± 32
	β_z	-0.024	± 0.069	± 0.190	-0.028	± 0.120	± 0.400	-0.017	± 0.01	± 0.035
<i>K</i> -long	$\log_{10}(M_{\text{BH}}/\text{M}_{\odot})$	0.1	<0.4	<0.7	3.703	± 0.005	± 0.015	4.080	± 0.001	± 0.004
	$M/L_{\text{F814W}} (M_{\odot}/L_{\odot})$	0.650	± 0.001	± 0.002	0.644	± 0.001	± 0.002	0.640	± 0.001	± 0.002
	$i(^{\circ})$	82	± 6	± 16	81	± 11	± 18	83.0	± 11	± 19
	β_z	-0.019	± 0.001	± 0.003	-0.014	± 0.002	± 0.009	-0.004	± 0.001	± 0.003
<i>J</i>	$\log_{10}(M_{\text{BH}}/\text{M}_{\odot})$	0.3	<0.6	<1.2	3.69	± 0.19	± 0.45	4.00	± 0.01	± 0.03
	$M/L_{\text{F814W}} (M_{\odot}/L_{\odot})$	0.692	± 0.003	± 0.008	0.679	± 0.001	± 0.003	0.671	± 0.001	± 0.003
	$i(^{\circ})$	80	± 7	± 16	82	± 14	± 30	75	± 16	± 29
	β_z	-0.038	± 0.140	± 0.460	-0.023	± 0.011	± 0.032	-0.025	± 0.009	± 0.033
<i>H</i>	$\log_{10}(M_{\text{BH}}/\text{M}_{\odot})$	0.1	<0.8	<1.6	3.66	± 0.32	± 0.91	4.00	± 0.03	± 0.06
	$M/L_{\text{F814W}} (M_{\odot}/L_{\odot})$	0.675	± 0.001	± 0.002	0.673	± 0.001	± 0.002	0.671	± 0.001	± 0.003
	$i(^{\circ})$	81	± 11	± 23	82	± 14	± 24	82	± 14	± 24
	β_z	-0.033	± 0.007	± 0.031	-0.025	± 0.006	± 0.017	-0.028	± 0.003	± 0.009
<i>K</i>	$\log_{10}(M_{\text{BH}}/\text{M}_{\odot})$	0.1	<0.7	<1.2	3.710	± 0.11	± 0.30	4.005	± 0.007	± 0.015
	$M/L_{\text{F814W}} (M_{\odot}/L_{\odot})$	0.691	± 0.001	± 0.002	0.689	± 0.001	± 0.002	0.684	± 0.001	± 0.002
	$i(^{\circ})$	80	± 11	± 22	79	± 15	± 31	80	± 15	± 25
	β_z	-0.038	± 0.006	± 0.016	-0.028	± 0.006	± 0.012	-0.025	± 0.003	± 0.012

Notes: We fixed the search ranges for all four model parameters (M_{BH} , M/L_{F814W} , β_z , and i) to ensure consistency in the fitting process. These ranges were set as follows:

- M_{BH} : from 0 to 10^6 M_{\odot} (or $\log_{10}(M_{\text{BH}}/\text{M}_{\odot})$: from 0 to 6)
- M/L_{F814W} : from 0.1 to 3 (M_{\odot}/L_{\odot})
- β_z : from -1.0 to 0.99
- i : from 5° to 90°

Column 1: The ELT/HARMONI grating. Column 2: The JAM_{cyl} model's parameters. Columns 3, 4, and 5: The best-fit parameters, 1σ (or 16-84%), and 3σ (or 0.14-99.86%) uncertainties provided by the JAM_{cyl} models, respectively, when constrained from the HARMONI mock kinematics. These model constraints are associated with the case of no input black hole ($M_{\text{BH}} = 0 \text{ M}_{\odot}$). Columns 6, 7, and 8: Similarities of Columns 3, 4, and 5 but for the case of input black hole mass of $M_{\text{BH}} = 5 \times 10^3 \text{ M}_{\odot}$. Columns 9, 10, and 11: Similarities of Columns 3, 4, and 5 but for the case of input black hole mass of $M_{\text{BH}} = 10^4 \text{ M}_{\odot}$.

Table 9. Best-fit JAM_{cyl} parameters and their statistical uncertainties for six mock IFS of NGC 3115 dw01

Grating (1)	Parameters (2)	input $M_{\text{BH}} = 0 \text{ M}_{\odot}$			input $\log_{10}(M_{\text{BH}}/\text{M}_{\odot}) = 4.544$			input $\log_{10}(M_{\text{BH}}/\text{M}_{\odot}) = 4.845$		
		(3)	(4)	(5)	(6)	(7)	(8)	(9)	(10)	(11)
		best-fit	1σ	3σ	best-fit	1σ	3σ	best-fit	1σ	3σ
		(16-84%) (0.14-99.86%)			(0.14-99.86%) (16-84%)			(16-84%) (0.14-99.86%)		
<i>H</i> -high	$\log_{10}(M_{\text{BH}}/\text{M}_{\odot})$	2.4	<2.5	<2.6	4.543	± 0.031	± 0.091	4.850	± 0.020	± 0.050
	$M/L_{\text{F814W}} (M_{\odot}/L_{\odot})$	1.487	± 0.001	± 0.004	1.446	± 0.002	± 0.005	1.441	± 0.002	± 0.005
	$i(^{\circ})$	5.00	± 0.010	± 0.034	5.001	± 0.006	± 0.022	5.000	± 0.01	± 0.03
	β_z	0.003	± 0.002	± 0.006	0.005	± 0.005	± 0.018	0.003	± 0.001	± 0.003
<i>K</i> -short	$\log_{10}(M_{\text{BH}}/\text{M}_{\odot})$	0.5	<1.8	<2.4	4.550	± 0.13	± 0.27	4.850	± 0.01	± 0.08
	$M/L_{\text{F814W}} (M_{\odot}/L_{\odot})$	1.410	± 0.002	± 0.010	1.408	± 0.003	± 0.007	1.398	± 0.001	± 0.003
	$i(^{\circ})$	5.000	± 0.020	± 0.099	5.07	± 0.04	± 0.14	5.00	± 0.03	± 0.10
	β_z	0.002	± 0.001	± 0.002	-0.002	± 0.005	± 0.018	-0.002	± 0.007	± 0.022
<i>K</i> -long	$\log_{10}(M_{\text{BH}}/\text{M}_{\odot})$	1.2	<2.8	<3.2	4.540	± 0.04	± 0.12	4.843	± 0.003	± 0.010
	$M/L_{\text{F814W}} (M_{\odot}/L_{\odot})$	1.422	± 0.001	± 0.003	1.408	± 0.001	± 0.003	1.398	± 0.001	± 0.002
	$i(^{\circ})$	5.000	± 0.004	± 0.012	5.000	± 0.005	± 0.014	70.1	± 2.1	± 6.6
	β_z	0.004	± 0.006	± 0.015	0.000	± 0.012	± 0.031	0.007	± 0.001	± 0.002
<i>J</i>	$\log_{10}(M_{\text{BH}}/\text{M}_{\odot})$	1.0	<2.0	<2.5	4.540	± 0.015	± 0.043	4.830	± 0.240	± 0.750
	$M/L_{\text{F814W}} (M_{\odot}/L_{\odot})$	1.449	± 0.002	± 0.006	1.443	± 0.001	± 0.009	1.438	± 0.002	± 0.004
	$i(^{\circ})$	80	± 12	± 24	79	± 11	± 29	80	± 12	± 24
	β_z	0.006	± 0.001	± 0.003	-0.007	± 0.006	± 0.020	-0.005	± 0.005	± 0.016
<i>H</i>	$\log_{10}(M_{\text{BH}}/\text{M}_{\odot})$	2.4	<2.0	<2.5	4.580	± 0.15	± 0.59	4.846	± 0.022	± 0.053
	$M/L_{\text{F814W}} (M_{\odot}/L_{\odot})$	1.475	± 0.002	± 0.007	1.463	± 0.003	± 0.007	1.414	± 0.004	± 0.009
	$i(^{\circ})$	6.49	± 0.18	± 0.69	5.006	± 0.075	± 0.210	9.0	± 1.2	± 3.5
	β_z	0.002	± 0.002	± 0.006	0.001	± 0.003	± 0.008	-0.001	± 0.008	± 0.019
<i>K</i>	$\log_{10}(M_{\text{BH}}/\text{M}_{\odot})$	0.5	<1.2	<1.6	4.550	± 0.16	± 0.54	4.845	± 0.023	± 0.045
	$M/L_{\text{F814W}} (M_{\odot}/L_{\odot})$	1.432	± 0.001	± 0.002	1.428	± 0.001	± 0.004	1.421	± 0.001	± 0.003
	$i(^{\circ})$	5.000	± 0.004	± 0.010	5.000	± 0.01	± 0.04	5.000	± 0.007	± 0.018
	β_z	0.001	± 0.004	± 0.012	0.003	± 0.002	± 0.005	-0.002	± 0.001	± 0.004

Notes: We fixed the search ranges for all four model parameters (M_{BH} , M/L_{F814W} , β_z , and i) to ensure consistency in the fitting process. These ranges were set as follows:

- M_{BH} : from 0 to 10^6 M_{\odot} (or $\log_{10}(M_{\text{BH}}/\text{M}_{\odot})$: from 0 to 6)
- M/L_{F814W} : from 0.1 to 3 (M_{\odot}/L_{\odot})
- β_z : from -1.0 to 0.99
- i : from 5° to 90°

Column 1: The ELT/HARMONI grating. Column 2: The JAM_{cyl} model's parameters. Columns 3, 4, and 5: The best-fit parameters, 1σ (or 16-84%), and 3σ (or 0.14-99.86%) uncertainties provided by the JAM_{cyl} models, respectively, when constrained from the HARMONI mock kinematics. These model constraints are associated with the case of no input black hole ($M_{\text{BH}} = 0 \text{ M}_{\odot}$). Columns 6, 7, and 8: Similarities of Columns 3, 4, and 5 but for the case of input black hole mass of $M_{\text{BH}} = 3.5 \times 10^4 \text{ M}_{\odot}$. Columns 9, 10, and 11: Similarities of Columns 3, 4, and 5 but for the case of input black hole mass of $M_{\text{BH}} = 7 \times 10^4 \text{ M}_{\odot}$.